

MODELING OF MICROPIPETTE ASPIRATION OF FLACCID HUMAN RED  
BLOOD CELL USING FINITE ELEMENTS

by

Ali Çağdaş Akyıldız

B.S., M.E., Bogaziçi University, 2006

Submitted to the Institute for Graduate Studies in  
Science and Engineering in partial fulfillment of  
the requirements for the degree of  
Master of Science

Graduate Program in in Mechanical Engineering  
Boğaziçi University

2008

MODELING OF MICROPIPETTE ASPIRATION OF FLACCID HUMAN RED  
BLOOD CELL USING FINITE ELEMENTS

APPROVED BY:

Prof. Günay Anlaş .....  
(Thesis Supervisor)

Assoc. Prof. Fazıl Önder Sönmez .....

Assist. Prof. Can Yücesoy .....

DATE OF APPROVAL: 06.10.2008

## ACKNOWLEDGEMENTS

I would like to express my sincere gratitude to my advisor Prof. Dr. Günay Anlaş for his cooperation and endless goodwill. I would like to thank Assoc. Prof. Fazıl Önder Sönmez and Assist. Prof. Can Yücesoy for their interest.

Special thanks and appreciation go to my family and my friends for their endless support.

Finally, I would like to thank TÜBİTAK for the financial support during my study.

## ABSTRACT

# MODELING OF MICROPIPETTE ASPIRATION OF FLACCID HUMAN RED BLOOD CELL USING FINITE ELEMENTS

This thesis aims to analyze the steady state deformation of flaccid red blood cell (RBC) in micropipette aspiration (MA) experiment using finite elements (FE). Three different geometries, namely infinite plane, disk and modified biconcave model are used for undeformed flaccid RBC to see the geometry effects.

ABAQUS is used to solve the micropipette aspiration problem. A nearly incompressible, isotropic, hyperelastic, 2D material model is used for the cell membrane with the aid of the user subroutine, UGENS. Comparing the experimental results found in literature and the computational results, material characteristics of RBC membrane is investigated where the appropriate in-plane shear modulus value is estimated as 3-4  $\mu\text{N}/\text{m}$ .

It is observed that the cytosol, the fluid inside the red blood cell, modeled as a hydraulic fluid does not affect the deformation of the aspirated membrane portion. Additionally, principal stretches and stress resultants and the fractional area change at maximum applied suction pressure are also computed.

## ÖZET

# YUMUŞAK İNSAN ALYUVARININ MİKROPİPETE EMİLİMİNİN SONLU ELEMANLAR İLE MODELLENMESİ

Bu tezin amacı yumuşak insan alyuvarının mikropipete emiliminin sonlu elemanlar ile analizini yapmaktır. Deforme olmamış yumuşak alyuvarı modellemek amacıyla üç farklı geometrik model oluşturulmuştur: sonsuz düzlem, disk ve değiştirilmiş bikonkav modelleri.

Mikropipet emilimi problemini çözmek için ABAQUS kullanılmıştır. Hücre membranı için kullanılan iki boyutlu, izotropik, hiperelastik malzeme modeli ABAQUS'e UGENS adlı altprogram yardımı ile tanımlanmıştır. Elde edilen sayısal sonuçlar ile literatürdeki deneysel sonuçların karşılaştırılması sonucunda alyuvar membranının malzeme özellikleri incelenmiş ve düzlem kayma modülünün değeri 3-4  $\mu\text{N}/\text{m}$  olarak bulunmuştur.

Çalışmada hidrolik bir sıvı olarak modellenen alyuvarın iç sıvısının aspire edilen membran bölgesindeki deformasyona etkisinin olmadığı gözlemlenmiştir. Ayrıca deformasyon sonucu membranda oluşan gerilim ve gerinim değerleri ile oransal alan değişimi de hesaplanmıştır.

## TABLE OF CONTENTS

ACKNOWLEDGEMENTS . . . . .	iii
ABSTRACT . . . . .	iv
ÖZET . . . . .	v
LIST OF FIGURES . . . . .	viii
LIST OF SYMBOLS/ABBREVIATIONS . . . . .	xv
1. INTRODUCTION . . . . .	1
1.1. Biological Structure of Human Red Blood Cell . . . . .	2
1.1.1. Components of Human Red Blood Cell and Their Material Behavior . . . . .	2
1.2. Micropipette Aspiration Experiment with Flaccid Human RBC . . . . .	4
1.3. Previous Studies on the Deformation of Red Blood Cell . . . . .	5
1.3.1. Previous Micropipette Aspiration Studies with Flaccid RBC . . . . .	7
1.3.2. Conclusions of Previous Micropipette Aspiration Studies with Flaccid RBC . . . . .	9
1.4. Thesis Objective . . . . .	10
2. FINITE DEFORMATION MECHANICS . . . . .	12
2.1. Strain and Deformation Measures for Finite Deformations . . . . .	16
2.2. Stress Measures for Finite Deformations . . . . .	25
2.3. Constitutive Relations for Nonlinear Elastic Materials under Finite Deformations: Hyperelasticity . . . . .	30
3. ELASTIC MATERIAL MODELS FOR RBC MEMBRANE . . . . .	39
3.1. 2D, Incompressible, Isotropic, Hyperelastic Material Model of Evans . . . . .	39
3.2. 2D, Compressible, Isotropic, Hyperelastic Material Model of Skalak et al. . . . .	43
3.3. 2D, Compressible, Isotropic, Hyperelastic Material Model of Evans et al. . . . .	44
3.4. 3D, Incompressible, Isotropic, Hyperelastic Material Model of Neo-Hookean Strain Energy Density Function . . . . .	47
3.5. Comparison of 2D and 3D Isotropic Hyperelastic Material Models . . . . .	48
4. MODELS FOR THE DEFORMATION OF FLACCID RBC BY MICROPIPETTE ASPIRATION . . . . .	52

4.1. Analytical Models . . . . .	52
4.1.1. Infinite Plane Membrane Model of Evans . . . . .	52
4.1.2. Infinite Plane Membrane Model of Chien et al. (Spherical Cap Model) . . . . .	58
4.2. FE Analysis . . . . .	60
5. PRESENT FE ANALYSIS . . . . .	62
5.1. Infinite Plane Membrane Model . . . . .	63
5.2. Disk Model . . . . .	65
5.3. Modified Biconcave Model . . . . .	66
6. RESULTS . . . . .	69
6.1. Infinite Plane Membrane Model . . . . .	69
6.2. Disk Model . . . . .	76
6.3. Modified Biconcave Model . . . . .	83
7. CONCLUSION . . . . .	93
REFERENCES . . . . .	95
REFERENCES NOT CITED . . . . .	98

## LIST OF FIGURES

Figure 1.1.	Human RBC [3] . . . . .	2
Figure 1.2.	Human RBC structure [3] . . . . .	3
Figure 1.3.	Human RBC membrane structure [5] . . . . .	3
Figure 1.4.	Deformations at constant area . . . . .	4
Figure 1.5.	Area expansion and bending deformations . . . . .	5
Figure 1.6.	Micropipette aspiration of flaccid human RBC . . . . .	5
Figure 1.7.	Infinite plane model [24] . . . . .	8
Figure 1.8.	Comparison of the analytical results obtained by Evans and by the spherical cap model of Chien et al. [24] . . . . .	9
Figure 2.1.	Reference and final configurations of a deformable body . . . . .	13
Figure 2.2.	2D illustration of the polar decompositions . . . . .	18
Figure 2.3.	Physical interpretations of different stress definitions . . . . .	29
Figure 3.1.	First principal stress resultant and fractional area change by biaxial tension for 2D, nearly incompressible, isotropic, hyperelastic material	50
Figure 3.2.	First principal stress resultant and fractional area change by uniaxial tension for 2D, nearly incompressible, isotropic, hyperelastic material . . . . .	50

Figure 3.3.	First principal stress and fractional area change by biaxial tension for neo-Hookean hyperelastic material . . . . .	51
Figure 3.4.	First principal stress and fractional area change by uniaxial tension for neo-Hookean hyperelastic material . . . . .	51
Figure 4.1.	Cross section of RBC biconcave shape estimated by Evans and Fung [15] . . . . .	61
Figure 5.1.	Cross section of the infinite plane membrane model at the initial state . . . . .	63
Figure 5.2.	Cross section of the infinite plane membrane model at the deformed state . . . . .	64
Figure 5.3.	Axisymmetric FE model for infinite plane geometry . . . . .	64
Figure 5.4.	Cross section of the disk model at the initial state . . . . .	65
Figure 5.5.	Cross section of the disk model at the deformed state . . . . .	65
Figure 5.6.	Axisymmetric FE model for the disk geometry . . . . .	66
Figure 5.7.	Modified biconcave model and the RBC geometry proposed by Evans and Fung . . . . .	67
Figure 5.8.	Cross section of the modified biconcave model at the initial state . . . . .	67
Figure 5.9.	Cross section of the modified biconcave model at the deformed state . . . . .	68
Figure 5.10.	Axisymmetric FE model for the modified biconcave geometry . . . . .	68

Figure 6.1.	Comparison of the experimental and analytical results given by Evans and La Celle [32] and FE simulation for infinite plane membrane model with $K = 500 \text{ mN/m}$ and $\mu = 3 \cdot 10^{-3} \text{ mN/m}$ . . . . .	70
Figure 6.2.	Results of infinite plane membrane models with different element numbers for $K = 500 \text{ mN/m}$ and $\mu = 3 \cdot 10^{-3} \text{ mN/m}$ . . . . .	71
Figure 6.3.	Comparison of FE simulation results for infinite plane membrane model with fixed value of $\mu$ and different $K$ values . . . . .	71
Figure 6.4.	Comparison of FE simulation results for infinite plane membrane model with fixed value of $K$ and different $\mu$ values . . . . .	72
Figure 6.5.	Fractional area change, $\alpha$ as a function of curvilinear distance, $s$ in the infinite plane membrane model for $K = 500 \text{ mN/m}$ and $\mu = 3 \cdot 10^{-3} \text{ mN/m}$ at $\Delta P = 0.07 \text{ kPa}$ . . . . .	73
Figure 6.6.	Fractional area change, $\alpha$ as a function of curvilinear distance, $s$ in the infinite plane membrane model for $K = 100 \text{ mN/m}$ and $\mu = 3 \cdot 10^{-3} \text{ mN/m}$ at $\Delta P = 0.07 \text{ kPa}$ . . . . .	73
Figure 6.7.	Fractional area change, $\alpha$ as a function of curvilinear distance, $s$ in the infinite plane membrane model for $K = 10 \text{ mN/m}$ and $\mu = 3 \cdot 10^{-3} \text{ mN/m}$ at $\Delta P = 0.07 \text{ kPa}$ . . . . .	74
Figure 6.8.	Fractional area change, $\alpha$ as a function of curvilinear distance, $s$ in the infinite plane membrane model for $K = 1 \text{ mN/m}$ and $\mu = 3 \cdot 10^{-3} \text{ mN/m}$ at $\Delta P = 0.07 \text{ kPa}$ . . . . .	74
Figure 6.9.	First principal stretch, $\lambda_1$ as a function of curvilinear distance, $s$ in the infinite plane membrane model for $K = 500 \text{ mN/m}$ and $\mu = 3 \cdot 10^{-3} \text{ mN/m}$ at $\Delta P = 0.07 \text{ kPa}$ . . . . .	75

Figure 6.10.	Second principal stretch, $\lambda_2$ as a function of curvilinear distance, $s$ in the infinite plane membrane model for $K = 500 \text{ mN/m}$ and $\mu = 3 \cdot 10^{-3} \text{ mN/m}$ at $\Delta P = 0.07 \text{ kPa}$ . . . . .	75
Figure 6.11.	First principal stress resultant, $\Sigma_1$ as a function of curvilinear distance, $s$ in the infinite plane membrane model for $K = 500 \text{ mN/m}$ and $\mu = 3 \cdot 10^{-3} \text{ mN/m}$ at $\Delta P = 0.07 \text{ kPa}$ . . . . .	76
Figure 6.12.	Second principal stress resultant, $\Sigma_2$ as a function of curvilinear distance, $s$ in the infinite plane membrane model for $K = 500 \text{ mN/m}$ and $\mu = 3 \cdot 10^{-3} \text{ mN/m}$ at $\Delta P = 0.07 \text{ kPa}$ . . . . .	77
Figure 6.13.	Comparison of the experimental and analytical results given by Evans and La Celle [32] and FE simulation with $K = 500 \text{ mN/m}$ and $\mu = 3 \cdot 10^{-3} \text{ mN/m}$ for disk model . . . . .	77
Figure 6.14.	Results of disk models with different element numbers for $K = 500 \text{ mN/m}$ and $\mu = 3 \cdot 10^{-3} \text{ mN/m}$ . . . . .	78
Figure 6.15.	Comparison of FE simulation results of disk model with fixed value of $\mu$ and different $K$ values . . . . .	79
Figure 6.16.	Comparison of FE simulation results of disk model with fixed value of $K$ and different $\mu$ values . . . . .	79
Figure 6.17.	Comparison of FE simulations results of infinite plane membrane and disk models with fixed value of $K =$ and different $\mu$ values . . . . .	80
Figure 6.18.	First principal stretch, $\lambda_1$ as a function of curvilinear distance, $s$ in the disk model for $K = 500 \text{ mN/m}$ and $\mu = 3 \cdot 10^{-3} \text{ mN/m}$ at $\Delta P = 0.07 \text{ kPa}$ . . . . .	80

Figure 6.19.	Second principal stretch, $\lambda_2$ as a function of curvilinear distance, $s$ in the disk model for $K = 500 \text{ mN/m}$ and $\mu = 3 \cdot 10^{-3} \text{ mN/m}$ at $\Delta P = 0.07 \text{ kPa}$ . . . . .	81
Figure 6.20.	Fractional area change, $\alpha$ as a function of curvilinear distance, $s$ in the disk model for $K = 500 \text{ mN/m}$ and $\mu = 3 \cdot 10^{-3} \text{ mN/m}$ at $\Delta P = 0.07 \text{ kPa}$ . . . . .	81
Figure 6.21.	First principal stress resultant, $\Sigma_1$ as a function of curvilinear distance, $s$ in the disk membrane model for $K = 500 \text{ mN/m}$ and $\mu = 3 \cdot 10^{-3} \text{ mN/m}$ at $\Delta P = 0.07 \text{ kPa}$ . . . . .	82
Figure 6.22.	Second principal stress resultant, $\Sigma_2$ as a function of curvilinear distance, $s$ in the disk model for $K = 500 \text{ mN/m}$ and $\mu = 3 \cdot 10^{-3} \text{ mN/m}$ at $\Delta P = 0.07 \text{ kPa}$ . . . . .	82
Figure 6.23.	Comparison of FE simulations results of modified biconcave shape model without cytosol for fixed value of $K$ and different $\mu$ values .	84
Figure 6.24.	Comparison of FE simulations results of modified biconcave shape model without cytosol for fixed value of $\mu$ and different $K$ values .	84
Figure 6.25.	Comparison of the experimental and analytical results given by Evans and La Celle [32] and FE simulation with $K = 500 \text{ mN/m}$ and $\mu = 3 \cdot 10^{-3} \text{ mN/m}$ and $\mu = 4 \cdot 10^{-3} \text{ mN/m}$ for modified biconcave model without cytosol . . . . .	85
Figure 6.26.	Results of modified biconcave models with different element numbers for $K = 500 \text{ mN/m}$ and $\mu = 3 \cdot 10^{-3} \text{ mN/m}$ . . . . .	85

Figure 6.27. Comparison of FE simulations results of infinite plane membrane and modified biconcave model without cytosol with fixed value of $K$ and different $\mu$ values . . . . .	86
Figure 6.28. Comparison of FE simulations results of infinite plane membrane and modified biconcave model without cytosol with fixed value of $K$ and different $\mu$ values . . . . .	86
Figure 6.29. Deformed shapes of modified biconcave model with and without cytosol . . . . .	87
Figure 6.30. First principal stretch, $\lambda_1$ as a function of curvilinear distance, $s$ in the modified biconcave model without cytosol for $K = 500 \text{ mN/m}$ and $\mu = 3 \cdot 10^{-3} \text{ mN/m}$ at $\Delta P = 0.07 \text{ kPa}$ . . . . .	87
Figure 6.31. Second principal stretch, $\lambda_2$ as a function of curvilinear distance, $s$ in the modified biconcave model without cytosol for $K = 500 \text{ mN/m}$ and $\mu = 3 \cdot 10^{-3} \text{ mN/m}$ at $\Delta P = 0.07 \text{ kPa}$ . . . . .	88
Figure 6.32. Fractional area change, $\alpha$ as a function of curvilinear distance, $s$ in the modified biconcave model without cytosol for $K = 500 \text{ mN/m}$ and $\mu = 3 \cdot 10^{-3} \text{ mN/m}$ at $\Delta P = 0.07 \text{ kPa}$ . . . . .	88
Figure 6.33. First principal stress resultant, $\Sigma_1$ as a function of curvilinear distance, $s$ in the modified biconcave model without cytosol for $K = 500 \text{ mN/m}$ and $\mu = 3 \cdot 10^{-3} \text{ mN/m}$ at $\Delta P = 0.07 \text{ kPa}$ . . . . .	89
Figure 6.34. Second principal stress resultant, $\Sigma_2$ as a function of curvilinear distance, $s$ in the modified biconcave model without cytosol for $K = 500 \text{ mN/m}$ and $\mu = 3 \cdot 10^{-3} \text{ mN/m}$ at $\Delta P = 0.07 \text{ kPa}$ . . . . .	89

- Figure 6.35. First principal stretch,  $\lambda_1$  as a function of curvilinear distance,  $s$  in the modified biconcave model with cytosol for  $K = 500 \text{ mN/m}$  and  $\mu = 3 \cdot 10^{-3} \text{ mN/m}$  at  $\Delta P = 0.07 \text{ kPa}$  . . . . . 90
- Figure 6.36. Second principal stretch,  $\lambda_2$  as a function of curvilinear distance,  $s$  in the modified biconcave model with cytosol for  $K = 500 \text{ mN/m}$  and  $\mu = 3 \cdot 10^{-3} \text{ mN/m}$  at  $\Delta P = 0.07 \text{ kPa}$  . . . . . 90
- Figure 6.37. Fractional area change,  $\alpha$  as a function of curvilinear distance,  $s$  in the modified biconcave model with cytosol for  $K = 500 \text{ mN/m}$  and  $\mu = 3 \cdot 10^{-3} \text{ mN/m}$  at  $\Delta P = 0.07 \text{ kPa}$  . . . . . 91
- Figure 6.38. First principal stress resultant,  $\Sigma_1$  as a function of curvilinear distance,  $s$  in the modified biconcave model with cytosol for  $K = 500 \text{ mN/m}$  and  $\mu = 3 \cdot 10^{-3} \text{ mN/m}$  at  $\Delta P = 0.07 \text{ kPa}$  . . . . . 91
- Figure 6.39. Second principal stress resultant,  $\Sigma_2$  as a function of curvilinear distance,  $s$  in the modified biconcave model with cytosol for  $K = 500 \text{ mN/m}$  and  $\mu = 3 \cdot 10^{-3} \text{ mN/m}$  at  $\Delta P = 0.07 \text{ kPa}$  . . . . . 92

## LIST OF SYMBOLS/ABBREVIATIONS

$A$	Area
$B$	Material constant
$B$	Bending stiffness
$\mathbf{B}$	Left Cauchy deformation or Finger tensor
$C$	Material constant
$\mathbf{C}$	Right Cauchy deformation tensor
$D$	Distance leading edge of RBC undergoes in the pipette
$\mathbf{e}$	Almansi-Eulerian strain tensor
$E_n$	Material constant
$\mathbf{F}$	Deformation gradient tensor
$G$	Material constant
$\vec{G}_1, \vec{G}_2$	Base vectors in the undeformed configuration
$\vec{g}_1, \vec{g}_2$	Base vectors in the deformed configuration
$I_1, I_2, I_3$	Invariants
$\mathbf{I}$	Identity matrix
$J$	Determinant of the deformation gradient tensor
$K$	In-plane bulk modulus
$p$	Lagrange multiplier
$r$	Radial coordinate
$\mathbf{R}$	Rotation tensor
$R_p$	Pipette radius
$s$	Curvilinear coordinate along the meridian
$\mathbf{S}$	2nd Piola-Kirchhoff stress tensor
$t$	Time
$\mathbf{T}$	1st Piola-Kirchhoff stress tensor
$\vec{x}$	Position vector in the deformed configuration
$\vec{X}$	Position vector in the undeformed configuration
$\mathbf{U}$	Right stretch tensor
$\vec{u}$	Displacement vector

$V$	Volume
$\mathbf{V}$	Left stretch tensor
$\alpha$	Fractional change in area
$\delta_{ij}$	Kronecker delta
$\Delta P$	Suction pressure
$\epsilon$	Green-Lagrange strain tensor
$\gamma_s$	In-plane shear strain
$\lambda_i$	Principal stretch in the $i$ 'th principal direction
$\mu$	In-plane shear modulus
$\phi$	Azimuthal coordinate
$\Psi$	Helmholtz free energy function, strain energy density function
$\sigma$	Cauchy (true) stress tensor
$\Sigma$	Cauchy stress resultant tensor
$\Sigma_s$	In-plane shear stress resultant
$\epsilon$	Small deformation strain tensor
FE	Finite elements
MA	Micropipette aspiration
RBC	Red blood cell
2D	2 dimensional
3D	3 dimensional

## 1. INTRODUCTION

Red blood cells (RBC) also known as erythrocytes or red cells are important components of the human circulatory system. They carry oxygen from lungs to body tissues. To reach all body tissues they have to squeeze and pass through all capillaries in the body. Some of human capillaries are much more smaller than RBC's and RBC's deform extremely during the passage through these small sized capillaries; they recover their original shape afterwards. The deformation characteristics of RBC and material properties of its membrane have been subjects of study for researchers.

Blood flow in the body is highly affected by the deformability of RBC's. Material and geometric properties of RBC influence the blood flow. Any change in these properties can disturb the blood flow and cause a disease in the body. For instance, RBC is used as the maturation lodge by intracellular parasites such as *Plasmodium Falciparum* that causes malaria. During the maturation process of the parasite in RBC, cell's mechanical properties are altered. RBC stiffens progressively losing the ability to undergo large deformations and becomes adhesive complicating the passage through the blood vessels and capillaries which can lead to cerebral malaria, hypoglycemia, respiratory distress and even death [1].

Moreover, RBC provides a convenient possibility for cell membrane studies. RBC just consists of a membrane complex and a fluid enclosed by the membrane called cytosol. Thus, the deformation behavior of the whole cell can be used to investigate the material behavior of the membrane.

Additionally, this simple biological structure made it the start point for the development of mechanical models for more complex structured cells.

Studies to understand the deformation of RBC and the material behavior of its membrane have been done where appropriate mechanical models for the cell and material models for its components are used to explain the results and observations

of whole cell experiments like micropipette aspiration, cell swelling, fluid shear flow deformation and optical tweezers stretching.

### 1.1. Biological Structure of Human Red Blood Cell

As shown in figure 1.1 a RBC has an axisymmetric biconcave shape with an average diameter of about 7-8  $\mu m$  and is remarkably simple structured compared to other types of cells. The nucleus and other organelles which are present during the development of the cell are expelled immediately after the release of the cell into the circulatory system. So, the only components of a mature human RBC are the membrane-associated cytoskeleton complex and the fluid inside called cytosol [2].

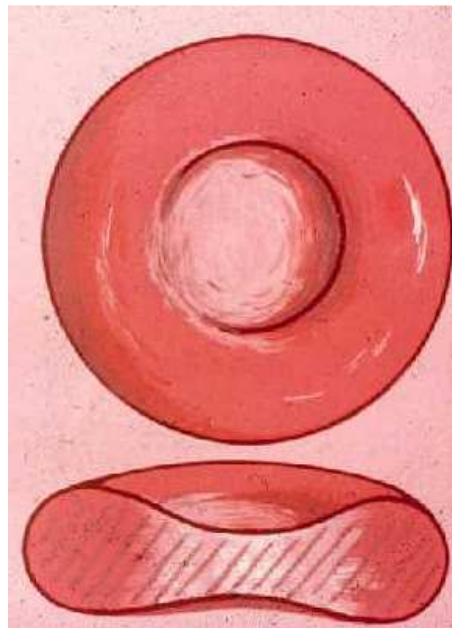


Figure 1.1. A human RBC [3]. The top view shows RBC to be circular whereas the side view shows RBC to be a biconcave disc

#### 1.1.1. Components of Human Red Blood Cell and Their Material Behavior

The cytosol inside the cell is assumed to behave as a Newtonian fluid. Therefore, elastic material and geometric properties of RBC can be fully attributed to the cell membrane [4].

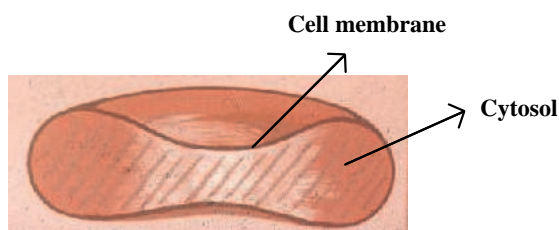


Figure 1.2. Components of human RBC [3]

As depicted in figure 1.3 RBC membrane consists of a lipid bilayer, transmembrane proteins and the spectrin network, namely the cytoskeleton [5]. In literature there are some analyses [5, 6, 7] where the whole membrane structure is considered as an effective continuum material since the interest lies in the characteristics of the whole membrane not the individual components of it.

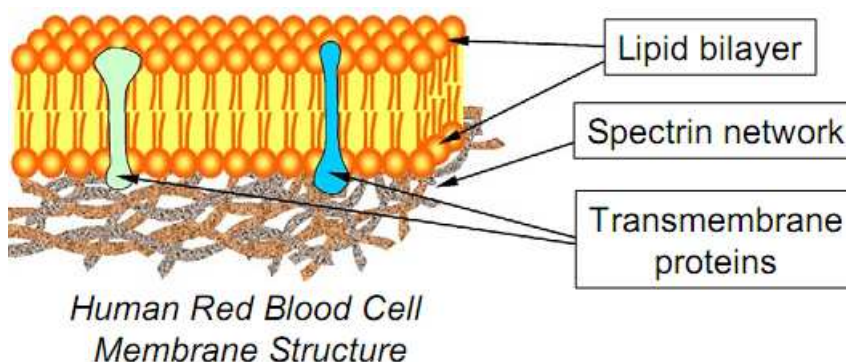


Figure 1.3. Human RBC membrane structure [5]

Because of the extremely small size of RBC well-known engineering material tests such as uniaxial tension, biaxial tension and compression tests with a specimen cut out of cell membrane cannot be performed. Only whole cell experiments like micropipette aspiration, cell swelling, fluid shear flow deformation and optical tweezers stretching techniques are used. Although not only the cell membrane but the whole cell deforms during these experiments the material properties of the membrane can be deduced from results using appropriate mechanical models. The Newtonian behavior of the cytosol causes that the deformation characteristics of the whole RBC come from the membrane. Therefore, whole cell experiments can be used to obtain the membrane material characteristics.

Previous studies characterized the material behavior of the RBC membrane with three elastic material properties: in-plane shear modulus,  $\mu$ ; in-plane bulk modulus,  $K$  and bending stiffness,  $B$  [8, 9]. Each of these material properties is related to two independent, fundamental elastic deformation type of membrane (figure 1.4 and 1.5): (1) *shear deformation* in the plane at constant surface area without bending the membrane, where this deformation can also be considered as an elongation in one principal direction and contraction in the second one and is characterized by in-plane shear modulus,  $\mu$ , with units of mN/m and (2) *isotropic* or *uniform dilation* in the plane without shearing or bending the membrane where the surface area is altered. This type of deformation is characterized by in-plane bulk modulus,  $K$ , with units of mN/m. In addition to the first two deformation types the membrane may also bend without shearing or expansion which is characterized by bending stiffness,  $B$ , with units of N·m [8].

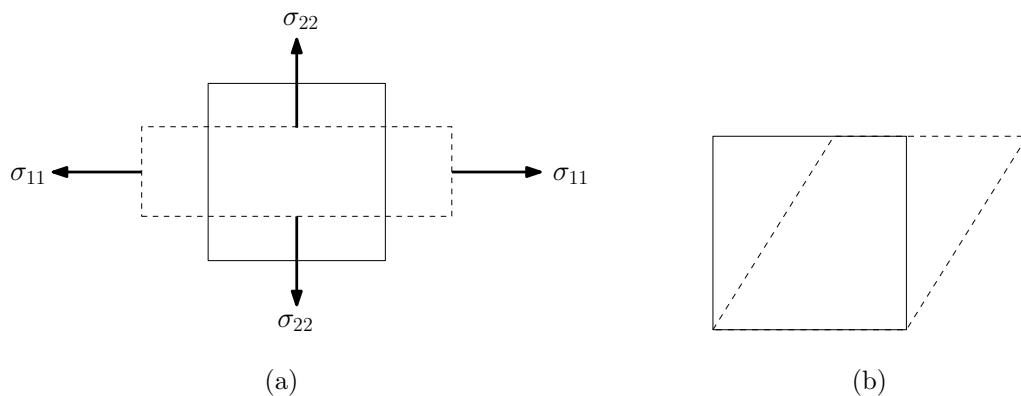


Figure 1.4. Deformations at constant area. (a) To keep the surface area constant elongation in one principal direction results in contraction in the other principal direction. (b) Simple shear deformation also occurs at constant area.

## 1.2. Micropipette Aspiration Experiment with Flaccid Human RBC

Micropipette aspiration is one of the whole cell experiments where the surface of the cell is sucked into a small glass tube and the leading edge of its surface is tracked. Figure 1.6 shows micropipette aspiration of a flaccid RBC. In the experiment, RBC is aspirated partially into the pipette. To aspirate the cell a suction pressure,  $\Delta P$  is applied, and the distance,  $D$ , the leading edge of RBC undergoes in the pipette, is recorded.

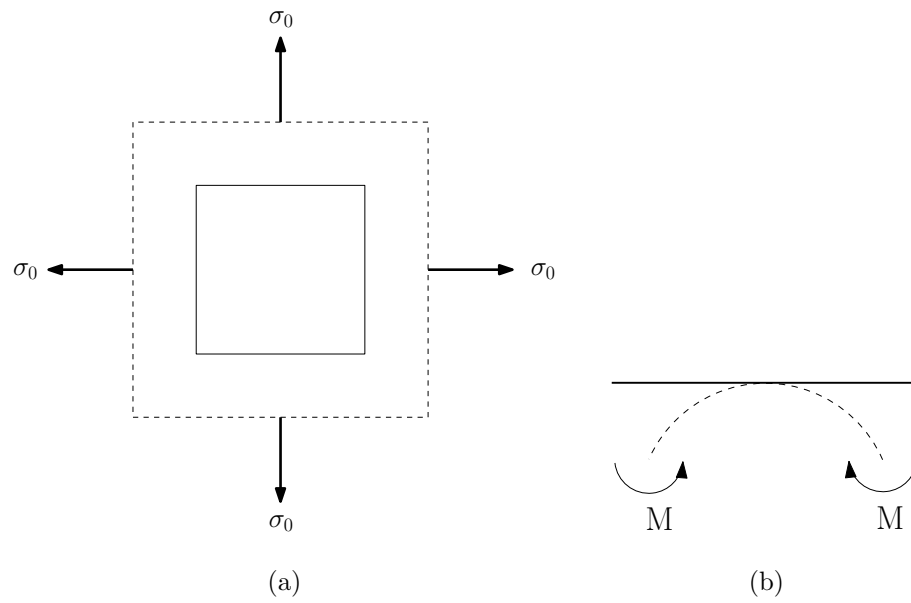


Figure 1.5. Area expansion and bending deformations a.) Area expansion for biaxial tension. b.) Bending deformation

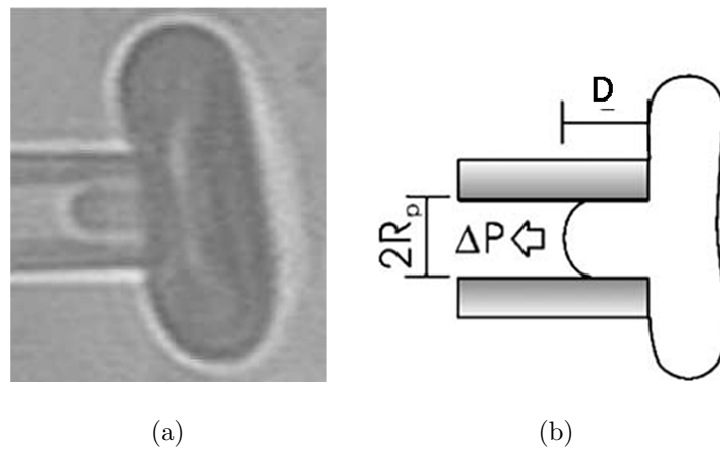


Figure 1.6. Micropipette aspiration of flaccid human RBC: a.) Image of the aspiration of a flaccid red blood cell into a pipette [10] b.) Schematic of a micropipette aspiration [11]

### 1.3. Previous Studies on the Deformation of Red Blood Cell

Rand and Burton [12] were the first to apply the micropipette aspiration technique to RBC (preswollen ones). They concluded that the membrane is isotropic in 2D. Rand

[13] found that RBC membrane has great resistance to isotropic surface tension which means high resistance to lysis. Hochmuth and Mohandas [14] observed that the RBC membrane can deform greatly subjected to uniaxial tension where they used the fluid shear flow technique. They realized that membrane surface area remained almost constant although the deformation in one direction was high. In addition, Evans and Fung [15] showed after swelling experiments that the transformation of RBC from biconcave shape to spherocyte did not cause an increase in the membrane surface area.

In the light of the previous studies Evans [16] proposed a material model for RBC membrane. He modeled the membrane as a 2D, incompressible, isotropic material and constructed an elastic strain energy density function with a single elastic constant. The constitutive law derived related Green-Lagrange strains to Cauchy stress resultants. He employed this material model to analyze cell swelling [16], fluid shear flow and micropipette aspiration experiments [17] using analytical models.

Skalak et al. [18] also proposed a material model for the RBC membrane similar to the one of Evans [16]; however by making use of a strain energy density function with two elastic constants. One of these constants is related to the shear deformation characteristics of the membrane which is analogous to the elastic constant in the Evans' work [16]. The second constant reflects the dilation characteristics of RBC membrane the value of which is much greater than the first one implying high resistance of the membrane to an area increase meaning a nearly incompressible material in 2D.

Note that the studies mentioned above made use of membrane material models which have no resistance to bending. Therefore the elastic constants have been derived to give the deformation response of RBC to in-plane force boundary conditions. However, some works were done also to identify the bending stiffness of RBC membrane [19, 20]. Zarda et al. [21] and Pai and Weymann [22] included both the bending and in-plane material characteristics in their analysis for osmotic swelling of RBC.

Recently, some studies to analyze the RBC deformation by optical tweezers experiment were conducted where continuum mechanics approach utilized finite element

method [5, 6, 23]. These researches used 3D, incompressible, isotropic, hyperelastic material models. In their work Dao et al. [5] modeled the RBC membrane complex as an effective continuum material and the cytosol inside the cell as a Newtonian fluid preserving the cell volume and maintaining the fluid pressure distribution inside the cell. They investigated the viscoelastic characteristics of the effective membrane by employing neo-Hookean hyperelastic strain energy density function for the elastic response of the RBC membrane.

### 1.3.1. Previous Micropipette Aspiration Studies with Flaccid RBC

Prior analytical studies of the micropipette aspiration of flaccid human red blood cell are the ones done by Evans [17] and Chien et al. [24]. Both analyzed this experiment where the suction of an infinite plane into a cylindrical micropipette was used as the model [17] (figure 1.7). This model is valid for small pipettes and for thin discocytes aspirated in the central region which is assumed to be relatively flat compared to the peripheral portion of the cell. Additionally, the model is just suitable for the experiments where the portion of the cell outside the pipette remains flat throughout the experiment and the sucked portion leans tightly to the pipette's wall. So, the model is valid for cells with nonspherical outside portion and if no buckling occurs inside the pipette. Another assumption is that there exists no frictional force between the pipette wall and the aspirated cell membrane.

Both studies benefited from the membrane theory where the structure is considered as incapable of conveying moments to analyze the experiment. Thus, the material behavior of the RBC membrane used by both analyses is the 2D, incompressible, isotropic, hyperelastic material model proposed by Evans [16].

The geometry of pipette, shapes RBC undergo in the experiment and the loading are axisymmetric. By solving the equilibrium equations for this axisymmetric condition both Evans and Chien et al. ended up with an equation relating the applied suction pressure,  $\Delta P$  to the distance,  $D$  the leading edge of RBC goes inside the pipette where the material constant is another parameter in the equation. By setting different values

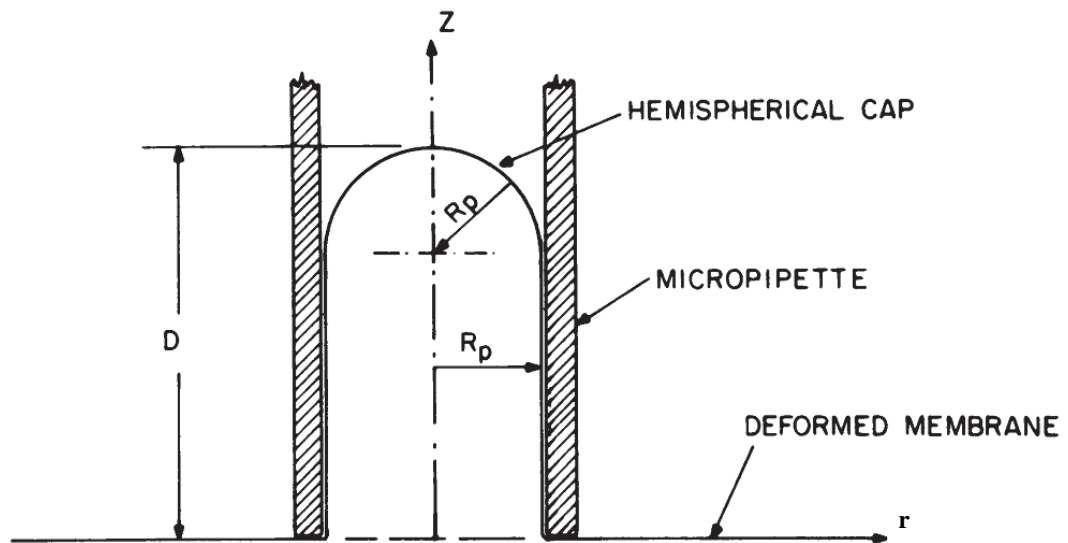


Figure 1.7. Schematic drawing of the deformed shape for analyzing the micropipette aspiration of the infinite plane membrane model used by Evans and Chien et al. [24]

for this material constant different  $\Delta P$  vs.  $D$  curves are obtained which are compared with the experimental curve.

The two analytical studies and their results are very similar. The important point where they diverge is the assumed final shape of the cap portion of RBC membrane inside the pipette. Evans assumed an elliptical cap where Chien et al. a hemispherical one.

Higuchi and Kanno analyzed the micropipette aspiration of flaccid human red blood cell by finite element method [25]. They modeled the membrane complex as an effective continuum material with the 3D, incompressible, hyperelastic material model of Arruda-Boyce form of strain energy potential. The initial RBC geometry used in the work is the biconcave shape proposed by Evans and Fung [15]. They conducted only small (nano-order) deformation simulations of micropipette aspiration of flaccid RBC in their work [25].

### 1.3.2. Conclusions of Previous Micropipette Aspiration Studies with Flaccid RBC

In works of Evans [17] and Chien et al. [24] the undeformed flaccid RBC is modeled as an infinite plane which is a very simplified model. Both analyses make assumptions on the deformed shape of the portion inside the pipette (spherical cap and elliptical cap) and solve the problem based on this assumption. The results of the two analyses [17, 24] have only slight differences. Chien et al. plotted this function to compare it with the one obtained by Evans (see graph 1.8). Moreover, due to the surface area constancy (2D incompressibility) assumption of the cell membrane they only estimated the value of in-plane shear modulus,  $\mu$  in their analyses which is the only material constant of the material model they used. The value of in-plane bulk modulus,  $K$  cannot be concluded from their analyses.

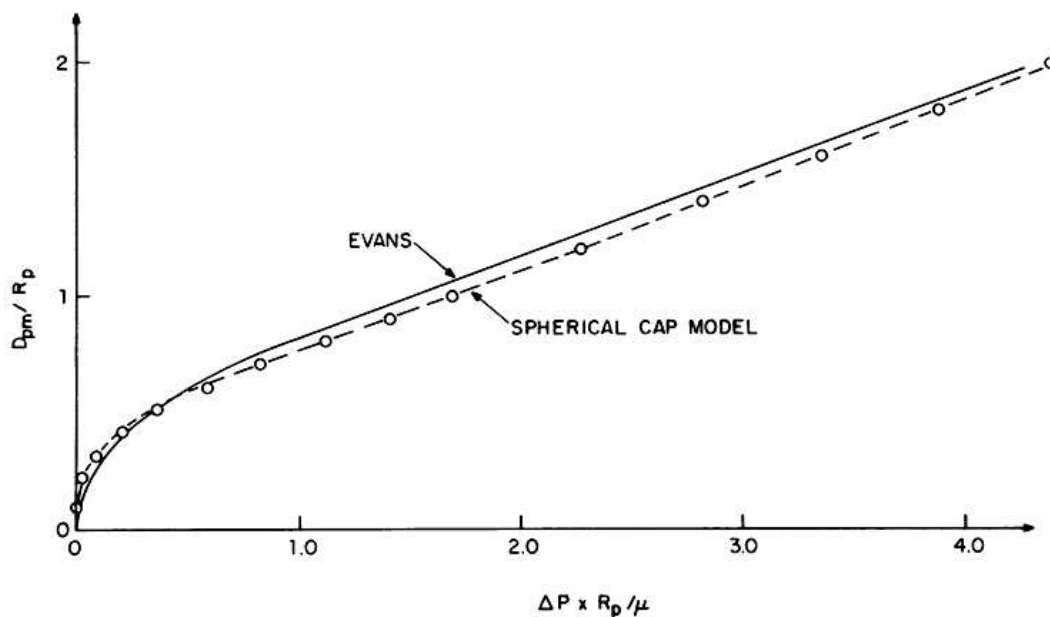


Figure 1.8. Comparison of the analytical results obtained by Evans and by the spherical cap model of Chien et al. [24]

Higuchi and Kanno conducted only small (nano-order) deformation simulations of micropipette aspiration of flaccid RBC in their work [25]. They used a 3D, incompressible, isotropic, hyperelastic material model for RBC membrane which does not

represent the material characteristics of the membrane very well. 3D, isotropic, hyperelastic material models preserve volume which are widely used in rubber elasticity. These material models may give reasonable results for small deformations but they are not suitable for large deformations. The incompressibility constraint in these material models results in increase in surface area where the membrane thickness is decreased to preserve the volume under large deformations which contradicts the RBC membrane material property that the surface area remains almost constant.

#### 1.4. Thesis Objective

Analytical works in literature [17, 24] that study the deformation of a flaccid RBC using micropipette aspiration experiments assume that the membrane is incompressible in 2D and use the material model of Evans [16] with a single material constant, namely the in-plane shear modulus,  $\mu$ . Thus, they only make estimations for this material constant. They miss the in-plane bulk modulus,  $K$ . Additionally, these works use an assumption for the final deformed state of the membrane (spheroidal cap, spherical cap) and solve for using this particular final state.

Recently, Higuchi and Kanno [25] studied the micropipette aspiration of a flaccid RBC using finite element method. They used a 3D, incompressible, isotropic, hyperelastic material model which is not suitable to analyze large RBC membrane deformations.

In the present work, large deformation of flaccid RBC in micropipette aspiration experiments is investigated using finite element modeling. A 2D, nearly incompressible, hyperelastic, isotropic material model is implemented to the finite element program, ABAQUS with the aid of a user subroutine, UGENS.

Three different geometrical models, namely the infinite plane, disk and modified biconcave model are used to represent the undeformed flaccid RBC. The effects of the cytosol, the fluid inside the red blood cell, on the deformation is also investigated by modeling it.

By comparing the results of the finite element simulations with the analytical and experimental results of previous studies the values of the material constants in the material model are estimated. Moreover, the principal stretches and stress resultants and the fractional area change after the deformation are also computed.

## 2. FINITE DEFORMATION MECHANICS

Biological materials like tissues and membranes frequently undergo finite deformations in physiological activities. Any deformation with a strain greater than 3-5% is classified as finite deformation.

Small deformation theory of elasticity assumes that material points in a deformable body undergo infinitesimal displacements and hence the difference between the deformed and undeformed states is negligible. In this theory strains and displacements are linearly related. But in finite deformation analysis, 1.) displacements are not infinitesimal and 2.) strains are not infinitesimal. The above mentioned assumptions are not valid for finite deformation analysis. If the deformation is small, linear strain tensor and Cauchy stress tensor are appropriate for use. On the other hand, for finite deformation proper strain and stress tensors have to be employed.

Assume that there is a deformable body in the reference or undeformed configuration in 3D space before the loads have been applied and that the same body gets a deformed configuration after loading (Figure 2.1). Note that a body might undergo rigid body motion in addition to deformation when loaded. The relation between the two position vectors,  $\vec{X}$  and  $\vec{x}$  of a point within this body defined in the undeformed and deformed configurations, respectively, are given by

$$\vec{x} = \vec{X} + \vec{u} \quad (2.1)$$

or

$$x_i = X_i + u_i \quad (2.2)$$

where  $\vec{u}$  is the displacement vector.

Consider two neighboring points  $P(X_1, X_2, X_3)$  and  $P'(X_1 + dX_1, X_2 + dX_2, X_3 +$

$dX_3$ ) in the undeformed configuration which are transformed into  $Q(x_1, x_2, x_3)$  and  $Q'(x_1 + dx_1, x_2 + dx_2, x_3 + dx_3)$  in the deformed state given in Figure 2.1. The vectors between these points in the reference and deformed configurations are defined as

$$\overrightarrow{PP'} = d\vec{X} \tag{2.3}$$

and

$$\overrightarrow{QQ'} = d\vec{x} . \tag{2.4}$$

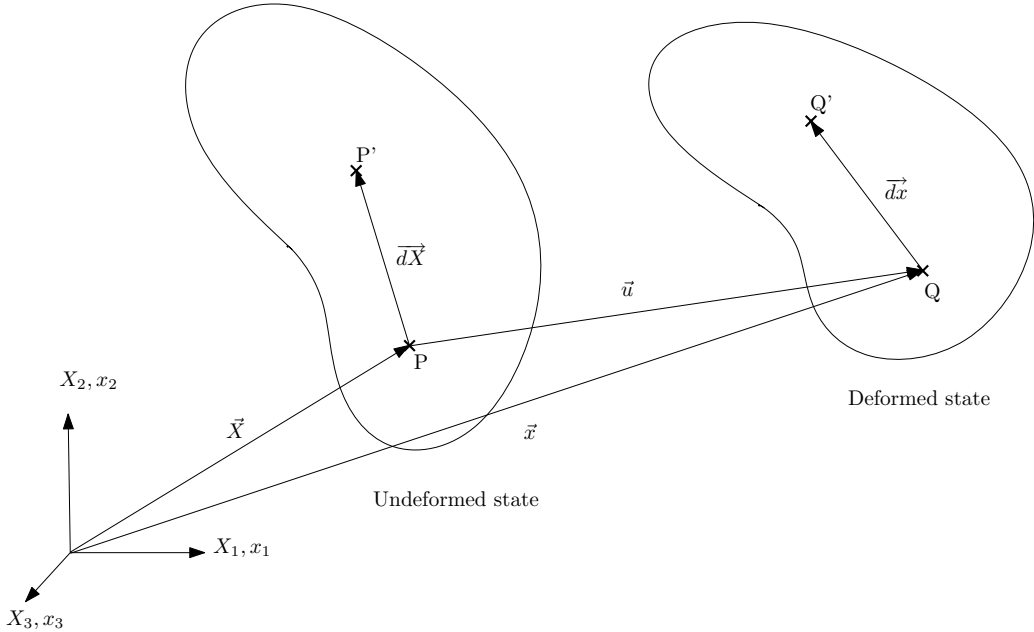


Figure 2.1. Reference and final configurations of a deformable body

The two vectors describe the orientation of an infinitesimal piece of material in the body in each configuration. Using the chain rule a mapping between these vectors are obtained:

$$dx_i = \frac{\partial x_i}{\partial X_j} dX_j . \tag{2.5}$$

This mapping called the deformation gradient tensor,  $\mathbf{F}$  is defined as

$$F_{ij} = \frac{\partial x_i}{\partial X_j} . \quad (2.6)$$

The second order tensor  $\mathbf{F}$  linearly maps a vector to a vector.

The deformation gradient tensor,  $\mathbf{F}$  in Cartesian coordinates is

$$\mathbf{F} = \begin{bmatrix} \frac{\partial x_1}{\partial X_1} & \frac{\partial x_1}{\partial X_2} & \frac{\partial x_1}{\partial X_3} \\ \frac{\partial x_2}{\partial X_1} & \frac{\partial x_2}{\partial X_2} & \frac{\partial x_2}{\partial X_3} \\ \frac{\partial x_3}{\partial X_1} & \frac{\partial x_3}{\partial X_2} & \frac{\partial x_3}{\partial X_3} \end{bmatrix} . \quad (2.7)$$

When equation 2.2 is used in equation 2.6 and the derivative is taken the deformation gradient tensor in terms of displacements is obtained as

$$F_{ij} = \frac{\partial(X_i + u_i)}{\partial X_j} = \delta_{ij} + \frac{\partial u_i}{\partial X_j} , \quad (2.8)$$

where  $\delta_{ij}$  is the Kronecker delta.

For a volume element described by  $\overrightarrow{dX_1}$ ,  $\overrightarrow{dX_2}$  and  $\overrightarrow{dX_3}$  in the undeformed state and by  $\overrightarrow{dx_1}$ ,  $\overrightarrow{dx_2}$  and  $\overrightarrow{dx_3}$  in the deformed state, the initial volume of the element,  $dV_0$  can be related to its volume in the deformed state,  $dV_f$ . The scalar triple products of these vectors give the volumes in the reference and the deformed states:

$$dV_0 = \overrightarrow{dX_1} \cdot (\overrightarrow{dX_2} \times \overrightarrow{dX_3}) \quad (2.9)$$

$$dV_f = \overrightarrow{dx_1} \cdot (\overrightarrow{dx_2} \times \overrightarrow{dx_3}) . \quad (2.10)$$

Using the deformation gradient tensor,  $\mathbf{F}$  vectors  $\overrightarrow{dx_1}$ ,  $\overrightarrow{dx_2}$  and  $\overrightarrow{dx_3}$  can be written in

the following form:

$$\begin{aligned}
 \overrightarrow{dx_1} &= \mathbf{F} \overrightarrow{dX_1}, \\
 \overrightarrow{dx_2} &= \mathbf{F} \overrightarrow{dX_2}, \\
 \overrightarrow{dx_3} &= \mathbf{F} \overrightarrow{dX_3}.
 \end{aligned} \tag{2.11}$$

The relation between the initial and final volumes is obtained via the following derivation:

$$\begin{aligned}
 dV_f &= (\mathbf{F} \overrightarrow{dX_1}) \cdot [(\mathbf{F} \overrightarrow{dX_2}) \times (\mathbf{F} \overrightarrow{dX_3})] \\
 &= (\mathbf{F} \overrightarrow{dX_1}) \cdot [\mathbf{F}^{-T} (\overrightarrow{dX_2} \times \overrightarrow{dX_3}) \det(\mathbf{F})] \\
 &= \overrightarrow{dX_1} \mathbf{F}^T \mathbf{F}^{-T} (\overrightarrow{dX_2} \times \overrightarrow{dX_3}) \det(\mathbf{F}) \\
 &= \underbrace{\det(\mathbf{F})}_J \underbrace{\overrightarrow{dX_1} \cdot (\overrightarrow{dX_2} \times \overrightarrow{dX_3})}_{dV_0} \\
 dV_f &= J dV_0,
 \end{aligned} \tag{2.12}$$

where  $J$  is the Jacobian or the determinant of the deformation gradient tensor.

The relation in 2.12 has two important interpretations. The first one is that the volume of an element in the deformed state is related to its volume in the undeformed state linearly by the factor  $J$ . Secondly, if the volume of the element needs to be constant after deformation, i.e.  $dV_0 = dV_f$  then the determinant of the deformation gradient matrix has to be equal to one.

Similarly, a relation between the initial and final areas of an infinitesimal area element defined by a parallelogram formed by two infinitesimal vectors  $\overrightarrow{dX_1}$  and  $\overrightarrow{dX_2}$  in the reference state and  $\overrightarrow{dx_1}$  and  $\overrightarrow{dx_2}$  in the undeformed state can be achieved. The initial and final areas are the absolute values of the cross products of the vectors:

$$dA_0 = \left\| \overrightarrow{dX_1} \times \overrightarrow{dX_2} \right\| \tag{2.13}$$

$$dA_f = \left\| \overrightarrow{dx_1} \times \overrightarrow{dx_2} \right\| . \quad (2.14)$$

Additionally, the vector  $\overrightarrow{dN}$  which is the cross product of the vectors  $\overrightarrow{dX_1}$  and  $\overrightarrow{dX_2}$  and the vector  $\overrightarrow{dn}$  which is the cross product of the vectors  $\overrightarrow{dx_1}$  and  $\overrightarrow{dx_2}$  can be written as follows:

$$\overrightarrow{dN} = \overrightarrow{dX_1} \times \overrightarrow{dX_2} = dA_0 \overrightarrow{N} \quad (2.15)$$

and

$$\overrightarrow{dn} = \overrightarrow{dx_1} \times \overrightarrow{dx_2} = dA_f \overrightarrow{n} \quad (2.16)$$

where  $\overrightarrow{N}$  and  $\overrightarrow{n}$  are the unit vectors in the direction of  $\overrightarrow{dN}$  and  $\overrightarrow{dn}$ , respectively. Making use of the deformation gradient tensor, the initial and final areas of the infinitesimal area element can be related to each other,

$$\begin{aligned} dA_f \overrightarrow{n} &= \overrightarrow{dx_1} \times \overrightarrow{dx_2} \\ &= (\mathbf{F} \overrightarrow{dX_1}) \times (\mathbf{F} \overrightarrow{dX_2}) \\ &= \det(\mathbf{F}) \mathbf{F}^{-T} \underbrace{(\overrightarrow{dX_1} \times \overrightarrow{dX_2})}_{dA_0 \overrightarrow{N}} \\ &= J \mathbf{F}^{-T} dA_0 \overrightarrow{N} . \end{aligned} \quad (2.17)$$

## 2.1. Strain and Deformation Measures for Finite Deformations

Although the deformation gradient tensor,  $\mathbf{F}$  measures how a body changes after the loads are applied on it, this tensor cannot be used directly for strain characterization since it also includes rigid body motions. To investigate the strain or deformation characterization, a measure without rigid body motion is needed.

Since the deformation gradient tensor  $\mathbf{F}$  is non-singular, according to the polar

decomposition theorem, there exist two positive definite symmetric tensors  $\mathbf{U}$  and  $\mathbf{V}$ , and an orthogonal tensor  $\mathbf{R}$ , uniquely determined by  $\mathbf{F}$ , such that

$$\mathbf{F} = \mathbf{R}\mathbf{U} = \mathbf{V}\mathbf{R} \quad (2.18)$$

holds [26].

$\mathbf{R}$  is called the rotation tensor, and  $\mathbf{U}$  and  $\mathbf{V}$  are the right and left stretch tensors, respectively. The geometrical interpretation of the polar decomposition of a 2D deformation gradient tensor,  $\mathbf{F}$  is summarized in Figure 2.2. In this figure there are four sets of base vectors:

1.  $\vec{G}_1 \& \vec{G}_2$
2.  $\vec{g}_1 \& \vec{g}_2$
3.  $\vec{G}'_1 \& \vec{G}'_2$
4.  $\vec{g}'_1 \& \vec{g}'_2$  .

The first and second sets display the base vectors in the initial and deformed configurations, respectively. The third one is the set of the base vectors after the rotation tensor,  $\mathbf{R}$  is applied to the initial configuration and the last set is obtained after the application of the right stretch tensor,  $\mathbf{U}$  to the initial configuration, such that

$$\mathbf{F}\vec{G}_i = \mathbf{R}\mathbf{U}\vec{G}_i = \mathbf{R}\vec{g}'_i = \vec{g}_i \quad (2.19)$$

and

$$\mathbf{F}\vec{G}_i = \mathbf{V}\mathbf{R}\vec{G}_i = \mathbf{V}\vec{G}'_i = \vec{g}_i \quad (2.20)$$

hold.

From 2.19 it follows that the deformation of an infinitesimal volume element having the position vector  $\vec{X}$  and  $\vec{x}$  in the reference and deformed configurations,

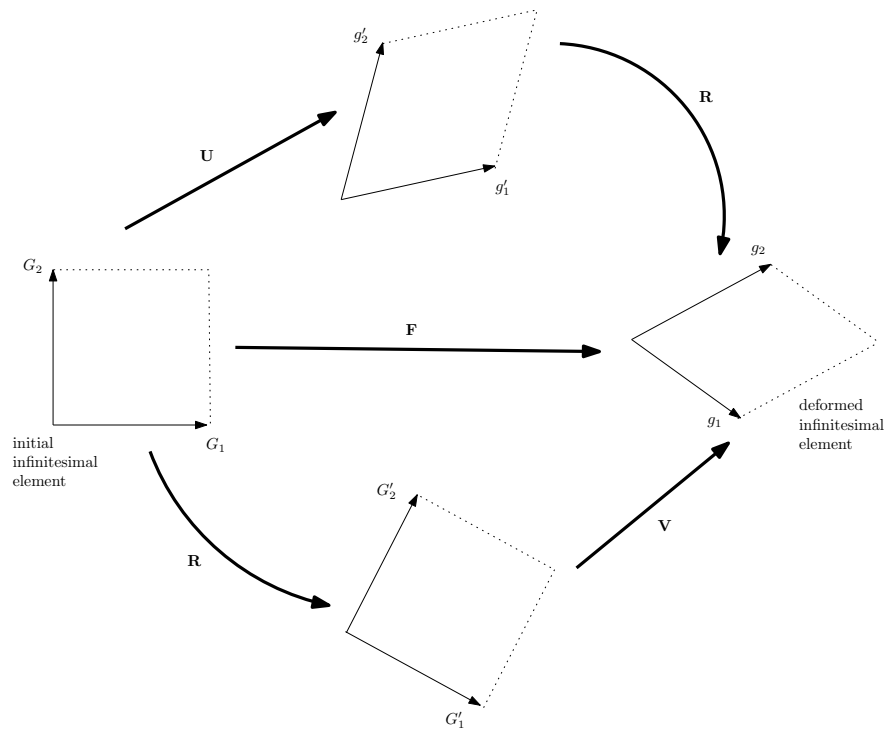


Figure 2.2. 2D illustration of the polar decompositions

respectively, can be considered as the successive application of:

- a stretch by the tensor  $\mathbf{U}$ ,
- a rigid body rotation by the tensor  $\mathbf{R}$ ,
- a translation by the vector  $\vec{v}$ ,

where the vector  $\vec{v}$  is the displacement vector of the origin. The above first two steps determine the base vectors  $\vec{g}_i$  of the deformed configuration and the third one determines the origin of the base vectors  $\vec{g}_i$ .

In an alternative way, equation 2.20 indicates that the same deformation can be considered as the result of the successive application of:

- a rigid body rotation by the tensor  $\mathbf{R}$ ,
- a stretch by the tensor  $\mathbf{V}$ ,
- a translation by the vector  $\vec{v}$  .

The above clarified mappings are illustrated in Figure 2.2.

$\mathbf{U}$  and  $\mathbf{V}$  have the same eigenvalues which are real and positive. The eigenvalues are the principal stretches, namely  $\lambda_i$ 's. Thus, a deformation can be defined with a rotation and stretches along the three mutually orthogonal axes in the principal directions [27]. Stretches in the principal directions which do not include rigid body motion can be used as deformation measure.

In order to obtain a strain measure, a relation describing the length change of a material vector from the undeformed configuration to the deformed one has to be found. A typical strain measure is the Green-Lagrange strain tensor,  $\epsilon$ . For a 1D case the Green-Lagrange strain,  $\epsilon$  is defined as the half of the ratio of the difference between the the initial length ( $L_0$ ) squared and final length ( $L_f$ ) squared of a line to the initial length squared:

$$\epsilon = \frac{L_f^2 - L_0^2}{2L_0^2}. \quad (2.21)$$

Thus, one can obtain the difference  $L_f^2 - L_0^2$  as:

$$2\epsilon L_0^2 = L_f^2 - L_0^2. \quad (2.22)$$

The stretch in 1D is defined as

$$\lambda = \frac{L_f}{L_0} = \frac{L_0 + \Delta L}{L_0} = 1 + \frac{\Delta L}{L_0} \quad (2.23)$$

where  $\Delta L$  is the change in length of the line whereas in 3D the stretches in the principal directions are defined by

$$\lambda_i = \frac{dx_i}{dX_i}; \quad (\text{no sum}) \quad . \quad (2.24)$$

Using the equations 2.21 and 2.23 the Green-Lagrange strain in 1D is related to stretch as

$$\epsilon = \frac{1}{2}(\lambda^2 - 1). \quad (2.25)$$

The extension to the 3D case is the replacement of  $L_0^2$  and  $L_f^2$  in equation 2.22 with  $dS_0^2$  and  $dS_f^2$ , respectively,

$$2\epsilon dS_0^2 = dS_f^2 - dS_0^2 \quad (2.26)$$

where  $dS_0^2$  and  $dS_f^2$  are the lengths of the vectors  $\overrightarrow{dX}$  and  $\overrightarrow{dx}$  squared, respectively, given by

$$\begin{aligned} dS_0^2 &= dX_i dX_i \\ &= dX_i \delta_{ij} dX_j \end{aligned} \quad (2.27)$$

and

$$\begin{aligned} dS_f^2 &= dx_i dx_i = dx_i \delta_{ij} dx_j \\ &= dX_i F_{ki} F_{kj} dX_j . \end{aligned} \quad (2.28)$$

If equations 2.27 and 2.28 are used in 2.26 the following relation is obtained:

$$2dX_i \epsilon_{ij} dX_j = dX_i F_{ki} F_{kj} dX_j - dX_i \delta_{ij} dX_j. \quad (2.29)$$

From equation 2.29 the definition of the Green-Lagrange strain tensor,  $\epsilon$  in terms of

the deformation gradient tensor is obtained:

$$\epsilon_{ij} = \frac{1}{2}(F_{ki}F_{kj} - \delta_{ij}) \quad (2.30)$$

or in matrix form

$$\boldsymbol{\epsilon} = \frac{1}{2}(\mathbf{F}^T \mathbf{F} - \mathbf{I}) . \quad (2.31)$$

The relationship between the Green-Lagrange strain tensor,  $\boldsymbol{\epsilon}$  and the displacement vector,  $\vec{u}$  is obtained using the equation 2.8 in equation 2.30:

$$\epsilon_{ij} = \frac{1}{2} \left[ \left( \delta_{ki} + \frac{\partial u_k}{\partial X_i} \right) \left( \delta_{kj} + \frac{\partial u_k}{\partial X_j} \right) - \delta_{ij} \right] . \quad (2.32)$$

Expanding the terms in parenthesis the following relation is achieved:

$$\epsilon_{ij} = \frac{1}{2} \left[ \delta_{ij} + \frac{\partial u_i}{\partial X_j} + \frac{\partial u_j}{\partial X_i} + \frac{\partial u_k}{\partial X_j} \frac{\partial u_k}{\partial X_i} - \delta_{ij} \right] \quad (2.33)$$

$$= \frac{1}{2} \left[ \frac{\partial u_i}{\partial X_j} + \frac{\partial u_j}{\partial X_i} + \frac{\partial u_k}{\partial X_j} \frac{\partial u_k}{\partial X_i} \right] . \quad (2.34)$$

It should be noted that the gradients in the Green-Lagrange strain tensor are defined with respect to the initial configuration. This means that all strain measures are calculated with respect to the undeformed state.

Another strain type, the Almansi-Eulerian strain tensor,  $\mathbf{e}$  is calculated with respect to the deformed state. For a 1D case the Almansi-Eulerian strain is defined as the half of the ratio of the difference between of the initial length ( $L_0$ ) squared and final length ( $L_f$ ) squared of a line to the final length squared:

$$e = \frac{L_0^2 - L_f^2}{2L_f^2} . \quad (2.35)$$

The relation for 3D is

$$2 \mathbf{e} dS_f^2 = dS_f^2 - dS_0^2. \quad (2.36)$$

After successive derivation like the one done above for the Green-Lagrangian strain tensor, the Almansi-Eulerian strain tensor is obtained in terms of the deformation gradient tensor as

$$e_{ij} = \frac{1}{2}(\delta_{ij} - F_{ki}^{-1}F_{kj}^{-1}) \quad (2.37)$$

or given in matrix form

$$\mathbf{e} = \frac{1}{2}(\mathbf{I} - \mathbf{F}^{-T}\mathbf{F}^{-1}) \quad (2.38)$$

and in terms of displacements as

$$e_{ij} = \frac{1}{2} \left[ \frac{\partial u_i}{\partial x_j} + \frac{\partial u_j}{\partial x_i} - \frac{\partial u_k}{\partial x_j} \frac{\partial u_k}{\partial x_i} \right]. \quad (2.39)$$

Note that the gradients in the Green-Lagrange strain tensor are defined with respect to the deformed configuration.

The Green-Lagrange and Almansi-Eulerian strain tensors contain quadratic terms meaning that large deformation analysis are nonlinear. If the small deformation assumption is made these quadratic terms are omitted. Therefore, for an infinitesimal displacement case the distinction between the Green-Lagrange and Almansi-Eulerian strain tensors disappears and a linear strain measure, the small deformation strain tensor,  $\boldsymbol{\varepsilon}$  is achieved,

$$\varepsilon_{ij} = \frac{1}{2} \left[ \frac{\partial u_i}{\partial X_j} + \frac{\partial u_j}{\partial X_i} \right]. \quad (2.40)$$

The right Cauchy deformation tensor,  $\mathbf{C}$  defined by

$$\mathbf{C} = \mathbf{F}^T \mathbf{F} \quad (2.41)$$

or in indicial form by

$$C_{ij} = F_{ki} F_{kj} , \quad (2.42)$$

is a frequently used quantity in the finite deformation analysis. The explicit matrix form of  $\mathbf{C}$  is

$$\mathbf{C} = \begin{bmatrix} \left(\frac{\partial x_k}{\partial X_1}\right)^2 & \frac{\partial x_k}{\partial X_1} \frac{\partial x_k}{\partial X_2} & \frac{\partial x_k}{\partial X_1} \frac{\partial x_k}{\partial X_3} \\ \frac{\partial x_k}{\partial X_2} \frac{\partial x_k}{\partial X_1} & \left(\frac{\partial x_k}{\partial X_2}\right)^2 & \frac{\partial x_k}{\partial X_2} \frac{\partial x_k}{\partial X_3} \\ \frac{\partial x_k}{\partial X_3} \frac{\partial x_k}{\partial X_1} & \frac{\partial x_k}{\partial X_3} \frac{\partial x_k}{\partial X_2} & \left(\frac{\partial x_k}{\partial X_3}\right)^2 \end{bmatrix} . \quad (2.43)$$

From equation 2.30 it follows that the Green-Lagrange strain tensor is related to the right Cauchy deformation tensor by

$$\epsilon_{ij} = \frac{1}{2}(C_{ij} - \delta_{ij}) \quad (2.44)$$

or in matrix form by

$$\boldsymbol{\epsilon} = \frac{1}{2}(\mathbf{C} - \mathbf{I}) . \quad (2.45)$$

If the right Cauchy deformation tensor is transformed such that directions 1,2 and 3 are the principal directions then all the gradients other than the ones with the same subscript  $\left(\frac{\partial x_i}{\partial X_i}\right)$  existing in the tensor equal to zero. The physical meaning of this is that the i'th-component of the position vector ( $x_i$ ) of an infinitesimal volume element in the deformed state depends only to the i'th-component of the position vector ( $X_i$ )

in the undeformed state,

$$x_i = f(X_i). \quad (2.46)$$

Thus, the right Cauchy deformation tensor in the principal direction reduces to

$$\mathbf{C} = \begin{bmatrix} \left(\frac{dx_1}{dX_1}\right)^2 & 0 & 0 \\ 0 & \left(\frac{dx_2}{dX_2}\right)^2 & 0 \\ 0 & 0 & \left(\frac{dx_3}{dX_3}\right)^2 \end{bmatrix}. \quad (2.47)$$

From equation 2.24 and 2.47 it follows that the right Cauchy deformation tensor,  $\mathbf{C}$  in the principal directions can be given as

$$\mathbf{C} = \begin{bmatrix} \lambda_1^2 & 0 & 0 \\ 0 & \lambda_2^2 & 0 \\ 0 & 0 & \lambda_3^2 \end{bmatrix}. \quad (2.48)$$

Another explanation to this is that the three real eigenvalues of the right Cauchy deformation tensor are the squares of the principal stretches, namely  $\lambda_i$ 's. Thus, using equation 2.44 the Green-Lagrange strains in the principal directions are

$$\begin{aligned} \epsilon_1 &= \frac{1}{2}(\lambda_1^2 - 1), \\ \epsilon_2 &= \frac{1}{2}(\lambda_2^2 - 1), \\ \epsilon_3 &= \frac{1}{2}(\lambda_3^2 - 1). \end{aligned} \quad (2.49)$$

Another frequently used quantity in the finite deformation mechanics is the left Cauchy deformation tensor (or Finger deformation tensor),  $\mathbf{B}$  defined by

$$\mathbf{B} = \mathbf{F}\mathbf{F}^T \quad (2.50)$$

or given by indicial notation as

$$B_{ij} = F_{ik}F_{jk} . \quad (2.51)$$

The explicit matrix form of  $\mathbf{B}$  is given by

$$\mathbf{B} = \begin{bmatrix} \left(\frac{\partial x_1}{\partial X_k}\right)^2 & \frac{\partial x_1}{\partial X_k} \frac{\partial x_2}{\partial X_k} & \frac{\partial x_1}{\partial X_k} \frac{\partial x_3}{\partial X_k} \\ \frac{\partial x_2}{\partial X_k} \frac{\partial x_1}{\partial X_k} & \left(\frac{\partial x_2}{\partial X_k}\right)^2 & \frac{\partial x_2}{\partial X_k} \frac{\partial x_3}{\partial X_k} \\ \frac{\partial x_3}{\partial X_k} \frac{\partial x_1}{\partial X_k} & \frac{\partial x_3}{\partial X_k} \frac{\partial x_2}{\partial X_k} & \left(\frac{\partial x_3}{\partial X_k}\right)^2 \end{bmatrix} . \quad (2.52)$$

The left Cauchy deformation tensor in principal directions reduces to

$$\mathbf{B} = \begin{bmatrix} \lambda_1^2 & 0 & 0 \\ 0 & \lambda_2^2 & 0 \\ 0 & 0 & \lambda_3^2 \end{bmatrix} \quad (2.53)$$

which is equal to the right Cauchy deformation tensor in principal directions.

## 2.2. Stress Measures for Finite Deformations

The well-known stress measure in engineering is the Cauchy (true) stress tensor,  $\boldsymbol{\sigma}$  which is basically defined as the force per unit deformed area. The strain measure that is appropriate to use with the Cauchy stress tensor is the small deformation strain tensor,  $\boldsymbol{\varepsilon}$ . This strain tensor is used in small deformations as its name suggests and that the deformed and undeformed areas in small deformations are approximately the same. The problem by using the Cauchy stress tensor in finite deformation cases is that the deformed area is generally not known. Therefore, a stress measure defined with respect to reference configuration is needed.

The stress tensor in the reference configuration area has to give the same force as

the Cauchy stress tensor which is defined in the deformed configuration. The traction applied on a surface is the product of the stress, the normal vector to the surface and the area of the surface. Thus, the total force  $\overrightarrow{dP}$  can be obtained via

$$\overrightarrow{dP} = \boldsymbol{\sigma} \overrightarrow{n} dA_f \quad (2.54)$$

or

$$\overrightarrow{dP} = \mathbf{T} \overrightarrow{N} dA_0 , \quad (2.55)$$

where  $\boldsymbol{\sigma}$  is the Cauchy stress tensor,  $\mathbf{T}$  is the new stress tensor with respect to the reference area,  $\overrightarrow{N}$  and  $\overrightarrow{n}$  are the unit normal vectors to the initial and final surfaces with the areas  $dA_0$  and  $dA_f$ , respectively. It follows from equations 2.54 and 2.55 that

$$\boldsymbol{\sigma} \overrightarrow{n} dA_f = \mathbf{T} \overrightarrow{N} dA_0 \quad (2.56)$$

holds. Recalling the mapping between the reference and deformed state surface areas given in equation 2.17 the left hand side of the above equation becomes

$$\boldsymbol{\sigma} \overrightarrow{n} dA_f = \boldsymbol{\sigma} J \mathbf{F}^{-T} \overrightarrow{N} dA_0 . \quad (2.57)$$

Equations 2.56 and 2.57 give a relation between the two stress tensors:

$$(\mathbf{T} - \boldsymbol{\sigma} J \mathbf{F}^{-T}) \overrightarrow{N} dA_0 = 0 . \quad (2.58)$$

This new stress tensor,  $\mathbf{T}$  defined with respect to the reference configuration is called the 1st Piola-Kirchhoff stress tensor and it follows from equation 2.58 that this tensor is given in terms of the Cauchy stress tensor as

$$\mathbf{T} = J \boldsymbol{\sigma} \mathbf{F}^{-T} . \quad (2.59)$$

or

$$T_{ij} = J \sigma_{ik} F_{jk}^{-1} \quad (2.60)$$

The Cauchy stress tensor in terms of the 1st Piola-Kirchhoff stress tensor is

$$\boldsymbol{\sigma} = J^{-1} \mathbf{T} \mathbf{F}^T \quad (2.61)$$

or in indicial notation

$$\sigma_{ij} = J^{-1} T_{ik} F_{jk} \quad (2.62)$$

There are two difficulties in using the 1st Piola-Kirchhoff stress tensor. First, it is not energetically appropriate to be used with the Green-Lagrange strain tensor which is used as the strain measure in finite deformation analysis. The product of the 1st Piola-Kirchhoff stress tensor and the Green-Lagrange strain tensor is not the same strain energy density result as the Cauchy stress tensor multiplied by the small deformation strain tensor. Secondly, 1st Piola-Kirchhoff stress tensor is not symmetric which causes difficulties by numerical analysis like finite element method. Another stress tensor, namely the 2nd Piola-Kirchhoff stress tensor,  $\mathbf{S}$  overcome these two handicaps.

The total force  $\overrightarrow{dP}$  can be mapped back into the reference configuration using the inverse of the deformation gradient tensor given by

$$\overrightarrow{dP'} = \mathbf{F}^{-1} \overrightarrow{dP} \quad (2.63)$$

where  $\overrightarrow{dP'}$  is the back mapped form of the force in the undeformed state. This force can be obtained by using the 2nd Piola-Kirchhoff stress tensor:

$$\overrightarrow{dP'} = \mathbf{S} \overrightarrow{N} dA_0 . \quad (2.64)$$

Equating the relation given in 2.63 and 2.64 and using the equation 2.54 the following is obtained:

$$\mathbf{S} \vec{N} dA_0 = \mathbf{F}^{-1} \boldsymbol{\sigma} \vec{n} dA_f . \quad (2.65)$$

After substituting the expression in the equation 2.17 for the deformed surface area the following equation is obtained:

$$(\mathbf{S} - J \mathbf{F}^{-1} \boldsymbol{\sigma} \mathbf{F}^{-T}) \vec{N} dA_0 = 0. \quad (2.66)$$

which results in the final form of the relationship between the 2nd Piola-Kirchhoff and the Cauchy stress tensors as

$$\mathbf{S} = J \mathbf{F}^{-1} \boldsymbol{\sigma} \mathbf{F}^{-T} \quad (2.67)$$

or given with indicial notation as

$$S_{ij} = J F_{ik}^{-1} \sigma_{km} F_{jm}^{-1} . \quad (2.68)$$

The inverse of this relationship gives the Cauchy stress tensor in terms of the 2nd Piola-Kirchhoff stress tensor:

$$\boldsymbol{\sigma} = J^{-1} \mathbf{F} \mathbf{S} \mathbf{F}^T \quad (2.69)$$

or

$$\sigma_{km} = J^{-1} F_{ki} S_{ij} F_{mj} . \quad (2.70)$$

From equations 2.61 and 2.69 the relation between the 1st and 2nd Piola-Kirchhoff

stress tensors is achieved as

$$\mathbf{S} = \mathbf{F}^{-1} \mathbf{T} . \quad (2.71)$$

The physical meaning of the 2nd Piola-Kirchhoff stress is hard to interpret (Figure 2.3). Usually, this tensor is used to solve finite deformation problems and then the Cauchy stress is computed from it.

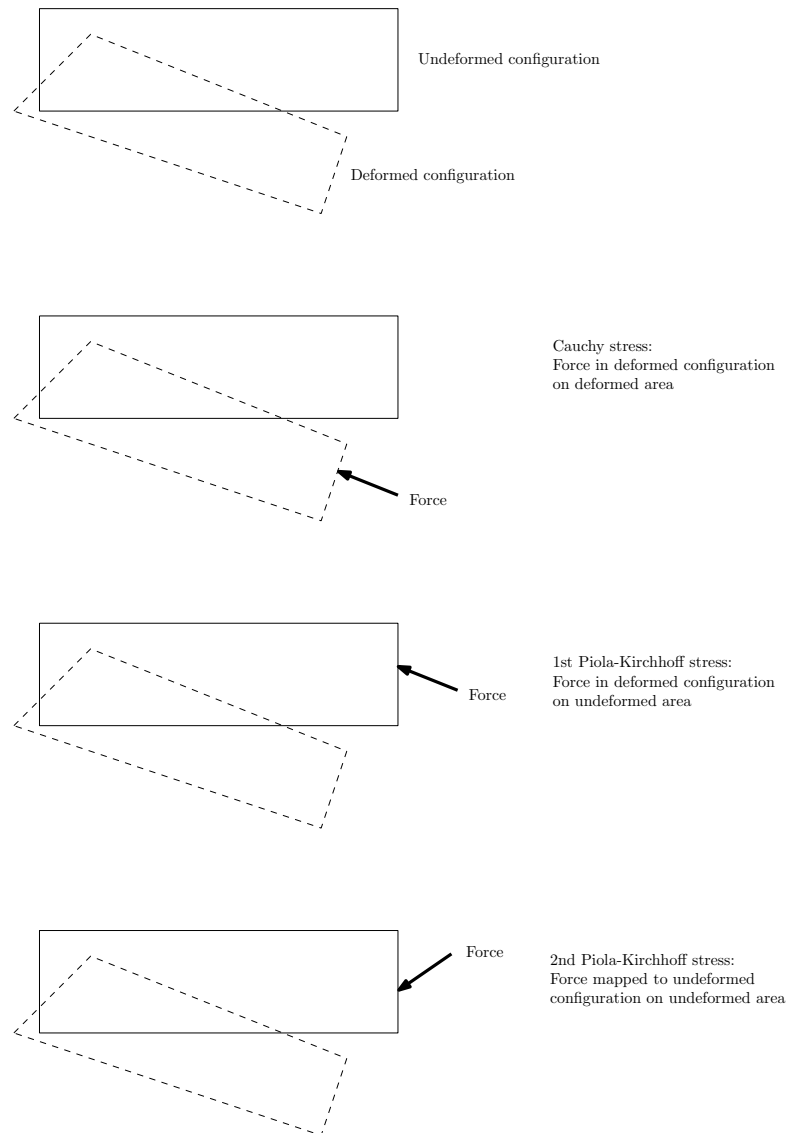


Figure 2.3. Physical interpretations and comparison of different stress definitions

### 2.3. Constitutive Relations for Nonlinear Elastic Materials under Finite Deformations: Hyperelasticity

A material is called Cauchy-elastic or just elastic if the stress field at time  $t$  depends only on the state of deformation and not on the deformation history. Hence, the stress field of an elastic material is independent of the deformation path and time.

An elastic material for which a strain energy density function exists is called hyperelastic or Green elastic material. A hyperelastic material postulates the existence of a Helmholtz free energy function,  $\Psi$  defined per unit reference volume. The Helmholtz free energy is a thermodynamic potential which measures the useful work obtainable from a closed thermodynamic system at a constant temperature and volume. For the case in which  $\Psi = \Psi(\mathbf{F})$  is solely a function of the deformation gradient tensor,  $\mathbf{F}$  or some strain tensor, the Helmholtz free energy function is referred to as the strain energy density function.

Constitutive equation of an isothermal elastic body relates the Cauchy stress tensor  $\boldsymbol{\sigma} = \boldsymbol{\sigma}(\vec{x}, t)$  at each point  $\vec{x}(\vec{X}, t)$  with the deformation gradient tensor  $\mathbf{F} = \mathbf{F}(\vec{X}, t)$ . The constitutive equation may be expressed in the general form

$$\boldsymbol{\sigma}(\vec{x}, t) = g(\mathbf{F}(\vec{X}, t), \vec{X}) \quad (2.72)$$

where  $g$  is referred as the response function associated with the Cauchy stress tensor,  $\boldsymbol{\sigma}$  or

$$\mathbf{T}(\vec{x}, t) = h(\mathbf{F}(\vec{X}, t), \vec{X}) \quad (2.73)$$

where  $h$  is referred as the response function associated with the 1st Piola-Kirchhoff stress tensor,  $\mathbf{T}$ .

Hyperelastic materials are a subclass of elastic materials whose response functions

g and h have the physical expressions of the form

$$\mathbf{T} = h(\mathbf{F}) = \frac{\partial \Psi(\mathbf{F})}{\partial \mathbf{F}} \quad (2.74)$$

and by use of relation 2.61,

$$\boldsymbol{\sigma} = g(\mathbf{F}) = J^{-1} \frac{\partial \Psi(\mathbf{F})}{\partial \mathbf{F}} \mathbf{F}^T . \quad (2.75)$$

Since the Cauchy stress tensor is symmetric ( $\boldsymbol{\sigma} = \boldsymbol{\sigma}^T$ ) the response function g also equals to the transpose of the expression given in the equation 2.75,

$$\boldsymbol{\sigma} = g(\mathbf{F}) = J^{-1} \mathbf{F} \left( \frac{\partial \Psi(\mathbf{F})}{\partial \mathbf{F}} \right)^T . \quad (2.76)$$

Consider a deformable body whose deformation is given by  $\mathbf{F}$ . After the body undergoes this deformation a rigid body motion is applied to it. The strain energy density functions before and after this rigid body motion must be equal. A proper choice for this rigid body motion might be a rotation given by the tensor  $\mathbf{R}^T$ . Hence, the strain energy density function should obey

$$\begin{aligned} \Psi(\mathbf{F}) &= \Psi(\mathbf{R}^T \mathbf{F}) \\ &= \Psi(\mathbf{R}^T \mathbf{R} \mathbf{U}) \\ &= \Psi(\mathbf{U}) . \end{aligned} \quad (2.77)$$

Equation 2.77 shows that  $\Psi$  is independent of the rotational part of  $\mathbf{F} = \mathbf{R} \mathbf{U}$  and depends only on the stretching part of  $\mathbf{F}$ , namely  $\mathbf{U}$ .

Additionally, since the right Cauchy tensor,  $\mathbf{C}$  and the Green-Lagrange strain tensor,  $\boldsymbol{\epsilon}$  are functions of the deformation gradient tensor,  $\mathbf{F}$ , the strain energy density function  $\Psi$  may also be written as the function of the right Cauchy tensor and the

Green-Lagrange strain tensor,

$$\Psi(\mathbf{F}) = \Psi(\mathbf{C}) = \Psi(\boldsymbol{\epsilon}) . \quad (2.78)$$

The time derivative of the strain energy function  $\Psi(\mathbf{F})$  can be obtained by means of the chain rule in the form of double contraction,

$$\frac{\partial \Psi(\mathbf{F})}{\partial t} = \frac{\partial \Psi(\mathbf{F})}{\partial \mathbf{F}} : \frac{\partial \mathbf{F}}{\partial t} . \quad (2.79)$$

The above relation may be expressed using the property of double contraction as

$$\frac{\partial \Psi(\mathbf{F})}{\partial t} = tr \left[ \left( \frac{\partial \Psi(\mathbf{F})}{\partial \mathbf{F}} \right)^T \frac{\partial \mathbf{F}}{\partial t} \right] . \quad (2.80)$$

Similarly, the time derivative of the strain energy function  $\Psi(\mathbf{C})$  can be achieved,

$$\begin{aligned} \frac{\partial \Psi(\mathbf{C})}{\partial t} &= \frac{\partial \Psi(\mathbf{C})}{\partial \mathbf{C}} : \frac{\partial \mathbf{C}}{\partial t} \\ &= tr \left[ \frac{\partial \Psi(\mathbf{C})}{\partial \mathbf{C}} \left( \frac{\partial \mathbf{C}}{\partial t} \right)^T \right] \\ &= tr \left[ \frac{\partial \Psi(\mathbf{C})}{\partial \mathbf{C}} \frac{\partial \mathbf{C}}{\partial t} \right] . \end{aligned} \quad (2.81)$$

Using the definition of the right Cauchy tensor  $\mathbf{C} = \mathbf{F}^T \mathbf{F}$  in 2.81 the following relation is obtained:

$$\begin{aligned} \frac{\partial \Psi(\mathbf{C})}{\partial t} &= tr \left[ \left( \frac{\partial \Psi(\mathbf{C})}{\partial \mathbf{C}} \right) \frac{\partial (\mathbf{F}^T \mathbf{F})}{\partial t} \right] \\ &= tr \left[ \left( \frac{\partial \Psi(\mathbf{C})}{\partial \mathbf{C}} \right) \left( \frac{\partial \mathbf{F}^T}{\partial t} \mathbf{F} + \mathbf{F}^T \frac{\partial \mathbf{F}}{\partial t} \right) \right] \\ &= tr \left[ \left( \frac{\partial \Psi(\mathbf{C})}{\partial \mathbf{C}} \right) \left( 2 \mathbf{F}^T \frac{\partial \mathbf{F}}{\partial t} \right) \right] . \end{aligned} \quad (2.82)$$

From equations 2.80 and 2.83 the following relation is deduced:

$$\left(\frac{\partial\Psi(\mathbf{F})}{\partial\mathbf{F}}\right)^T = 2\frac{\partial\Psi(\mathbf{C})}{\partial\mathbf{C}}\mathbf{F}^T. \quad (2.83)$$

Substituting back the equation 2.83 into 2.76 an important reduced form of the constitutive equation for hyperelastic materials is obtained,

$$\boldsymbol{\sigma} = 2J^{-1}\mathbf{F}\frac{\partial\Psi(\mathbf{C})}{\partial\mathbf{C}}\mathbf{F}^T. \quad (2.84)$$

Alternative expressions may be obtained for the 1st and 2nd Piola-Kirchhoff stress tensors by using equations 2.59 and 2.67,

$$\mathbf{T} = 2\mathbf{F}\frac{\partial\Psi(\mathbf{C})}{\partial\mathbf{C}} \quad (2.85)$$

$$\mathbf{S} = 2\frac{\partial\Psi(\mathbf{C})}{\partial\mathbf{C}}. \quad (2.86)$$

Using the chain rule and the expression 2.45 in the equation 2.86 the 2nd Piola-Kirchhoff stress tensor is obtained as the derivative of the strain energy density function with respect to the Green-Lagrange strain tensor,

$$\mathbf{S} = 2\frac{\partial\Psi}{\partial\boldsymbol{\epsilon}}\frac{\partial\boldsymbol{\epsilon}}{\partial\mathbf{C}} = \frac{\partial\Psi(\boldsymbol{\epsilon})}{\partial\boldsymbol{\epsilon}}. \quad (2.87)$$

Since the scalar valued strain energy density function is invariant under rotation (equation 2.77) it may also be expressed in terms of the principal invariants of its

argument. For instance, the function may be given in the form of

$$\Psi = \Psi(\mathbf{C}) = \Psi [I_1(\mathbf{C}), I_2(\mathbf{C}), I_3(\mathbf{C})] \quad (2.88)$$

where  $I_i$ 's are the invariants of  $\mathbf{C}$  with the definitions of

$$I_1(\mathbf{C}) = \text{tr} \mathbf{C} = \lambda_1^2 + \lambda_2^2 + \lambda_3^2 \quad (2.89)$$

$$\begin{aligned} I_2(\mathbf{C}) &= \frac{1}{2} [(\text{tr} \mathbf{C})^2 - \text{tr}(\mathbf{C}^2)] \\ &= \text{tr} \mathbf{C}^{-1} \det \mathbf{C} \\ &= \lambda_1^2 \lambda_2^2 + \lambda_1^2 \lambda_3^2 + \lambda_2^2 \lambda_3^2 \end{aligned} \quad (2.90)$$

$$I_3(\mathbf{C}) = \det \mathbf{C} = \lambda_1^2 \lambda_2^2 \lambda_3^2 . \quad (2.91)$$

Third invariant of  $\mathbf{C}$  is the determinant of the tensor. If a tensor is a product of two other tensors then its determinant equals to the product of the determinants of these two tensors. Application of this rule for  $\mathbf{C}$  results in

$$\det \mathbf{C} = \det \mathbf{F} \det \mathbf{F}^T = J^2 , \quad (2.92)$$

where  $J$  is the determinant of the deformation gradient tensor,  $\mathbf{F}$ . Equating the relations 2.91 and 2.92 and taking the square root gives

$$J = \lambda_1 \lambda_2 \lambda_3 . \quad (2.93)$$

From equations 2.48 and 2.53 it can be observed that the invariants of the left Cauchy deformation tensor are the same with those of the right Cauchy deformation tensor such that

$$\begin{aligned} I_1(\mathbf{B}) &= I_1(\mathbf{C}) \\ I_2(\mathbf{B}) &= I_2(\mathbf{C}) \\ I_3(\mathbf{B}) &= I_3(\mathbf{C}) \end{aligned} \tag{2.94}$$

hold.

Constitutive equations for hyperelastic materials in terms of invariants are obtained with the equation 2.86 by means of the chain rule differentiation,

$$\mathbf{S} = 2 \frac{\partial \Psi(\mathbf{C})}{\partial \mathbf{C}} = 2 \left( \frac{\partial \Psi}{\partial I_1} \frac{\partial I_1}{\partial \mathbf{C}} + \frac{\partial \Psi}{\partial I_2} \frac{\partial I_2}{\partial \mathbf{C}} + \frac{\partial \Psi}{\partial I_3} \frac{\partial I_3}{\partial \mathbf{C}} \right). \tag{2.95}$$

The derivatives of the invariants with respect to  $\mathbf{C}$  are given by

$$\begin{aligned} \frac{\partial I_1}{\partial \mathbf{C}} &= \mathbf{I} \\ \frac{\partial I_2}{\partial \mathbf{C}} &= I_1 \mathbf{I} - \mathbf{C} \\ \frac{\partial I_3}{\partial \mathbf{C}} &= I_3 \mathbf{C}^{-1} \quad [28]. \end{aligned} \tag{2.96}$$

Using the relations in 2.96 in the equation 2.95 an expression for the 2nd Piola-Kirchhoff stress tensor in terms of the three invariants is obtained,

$$\mathbf{S} = 2 \frac{\partial \Psi(\mathbf{C})}{\partial \mathbf{C}} = 2 \left[ \left( \frac{\partial \Psi}{\partial I_1} + I_1 \frac{\partial \Psi}{\partial I_2} \right) \mathbf{I} - \frac{\partial \Psi}{\partial I_2} \mathbf{C} + I_3 \frac{\partial \Psi}{\partial I_3} \mathbf{C}^{-1} \right]. \tag{2.97}$$

The relation for the Cauchy stress tensor can be deduced from the equation 2.97

using the relation 2.69 and the definition of the right Cauchy tensor  $\mathbf{C} = \mathbf{F}^T \mathbf{F}$ ,

$$\boldsymbol{\sigma} = 2J^{-1} \left[ I_3 \frac{\partial \Psi}{\partial I_3} \mathbf{I} + \left( \frac{\partial \Psi}{\partial I_1} + I_1 \frac{\partial \Psi}{\partial I_2} \right) \mathbf{B} - \frac{\partial \Psi}{\partial I_2} \mathbf{B}^2 \right]. \quad (2.98)$$

Cayley-Hamilton equation states that every (second order) tensor  $\mathbf{A}$  satisfies its own characteristic equation,

$$\mathbf{A}^3 - I_1 \mathbf{A}^2 + I_2 \mathbf{A} - I_3 \mathbf{I} = 0 \quad (2.99)$$

where  $I_i$ 's are the invariants of the tensor  $\mathbf{A}$ . If the left Cauchy deformation tensor,  $\mathbf{B}$  is used in the Cayley-Hamilton equation it becomes

$$\mathbf{B}^3 - I_1 \mathbf{B}^2 + I_2 \mathbf{B} - I_3 \mathbf{I} = 0. \quad (2.100)$$

When the equation is multiplied with  $\mathbf{B}^{-1}$  an expression for  $\mathbf{B}^2$  is achieved,

$$\mathbf{B}^2 = I_1 \mathbf{B} - I_2 \mathbf{I} + I_3 \mathbf{B}^{-1}. \quad (2.101)$$

An alternative form to the relation 2.98 is obtained by using 2.101 in it,

$$\boldsymbol{\sigma} = 2J^{-1} \left[ \left( I_2 \frac{\partial \Psi}{\partial I_2} + I_3 \frac{\partial \Psi}{\partial I_3} \right) \mathbf{I} + \frac{\partial \Psi}{\partial I_1} \mathbf{B} - I_3 \frac{\partial \Psi}{\partial I_2} \mathbf{B}^{-1} \right]. \quad (2.102)$$

The strain energy density function may also be regarded as a function of the principal stretches  $\lambda_i$  ( $i = 1, 2, 3$ ). Then, the principal Cauchy stresses are given by

$$\sigma_i = J^{-1} \lambda_i \frac{\partial \Psi}{\partial \lambda_i}; \quad i = 1, 2, 3 \quad [28]. \quad (2.103)$$

Additionally, the principal 1st and 2nd Piola-Kirchhoff stresses may be expressed

as

$$T_i = \frac{\partial \Psi}{\partial \lambda_i}; \quad i = 1, 2, 3 \quad (2.104)$$

and

$$S_i = \frac{1}{\lambda_i} \frac{\partial \Psi}{\partial \lambda_i}; \quad i = 1, 2, 3 \quad , \quad (2.105)$$

respectively, which are related to the principal Cauchy stresses as

$$T_i = J \lambda_i^{-1} \sigma_i; \quad i = 1, 2, 3 \quad (2.106)$$

and

$$S_i = J \lambda_i^{-2} \sigma_i; \quad i = 1, 2, 3 \quad . \quad (2.107)$$

Some materials like numerous polymers may undergo finite deformations without an observable volume changes. These material may be regarded as incompressible which is a common assumption in continuum and computational mechanics. The incompressibility constraint is characterized by  $J = 1$  (see equation 2.12). Materials with internal constraints such as the incompressibility are referred to as constrained materials.

The strain energy function for an incompressible material may be postulated as

$$\Psi = \Psi(\mathbf{F}) - p(J - 1) \quad , \quad (2.108)$$

where  $\Psi$  is defined for  $J = \det \mathbf{F} = 1$ . The scalar,  $p$  in the above equation serves as an indeterminate Lagrange multiplier and can be identified as a hydrostatic pressure. This scalar represents a workless reaction to the kinematic constraint and may only be determined from the equilibrium equations and the boundary conditions.

A constitutive equation for the 1st Piola-Kirchhoff stress tensor,  $\mathbf{T}$  is arrived by differentiating equation 2.108 with respect to the deformation gradient tensor,  $\mathbf{F}$  as given in equation 2.74 and using the identity  $(\partial J/\partial \mathbf{F} = J\mathbf{F}^{-T})$ ,

$$\mathbf{T} = -p\mathbf{F}^{-T} + \frac{\partial\Psi(\mathbf{F})}{\partial\mathbf{F}} . \quad (2.109)$$

Multiplying equation 2.109 by  $\mathbf{F}^{-1}$  from the left-hand side, the 2nd Piola-Kirchhoff stress tensor,  $\mathbf{S}$  as given in 2.71 takes the form

$$\mathbf{S} = -p\mathbf{F}^{-1}\mathbf{F}^{-T} + \mathbf{F}^{-1}\frac{\partial\Psi(\mathbf{F})}{\partial\mathbf{F}} \quad (2.110)$$

and after using equation 2.83 the relation becomes

$$\mathbf{S} = -p\mathbf{C}^{-1} + 2\frac{\partial\Psi(\mathbf{C})}{\partial\mathbf{C}} . \quad (2.111)$$

If equation 2.109 is multiplied by  $\mathbf{F}^T$  from the right-hand side the symmetric Cauchy stress tensor,  $\boldsymbol{\sigma}$  is obtained:

$$\boldsymbol{\sigma} = -p\mathbf{I} + \frac{\partial\Psi(\mathbf{F})}{\partial\mathbf{F}}\mathbf{F}^T = -p\mathbf{I} + \mathbf{F}\left(\frac{\partial\Psi(\mathbf{F})}{\partial\mathbf{F}}\right)^T . \quad (2.112)$$

If the strain energy density function,  $\Psi$  is expressed as a function of the principal stretches then the relations of the stress tensors become

$$\sigma_i = -p + \lambda_i \frac{\partial\Psi}{\partial\lambda_i} ; \quad i = 1, 2, 3 ; \quad (\text{no sum}) , \quad (2.113)$$

$$T_i = -p\lambda_i^{-1} + \frac{\partial\Psi}{\partial\lambda_i} ; \quad i = 1, 2, 3 ; \quad (\text{no sum}) , \quad (2.114)$$

$$S_i = -p\lambda_i^{-2} + \lambda_i^{-1} \frac{\partial\Psi}{\partial\lambda_i} ; \quad i = 1, 2, 3 ; \quad (\text{no sum}) . \quad (2.115)$$

### 3. ELASTIC MATERIAL MODELS FOR RBC MEMBRANE

#### 3.1. 2D, Incompressible, Isotropic, Hyperelastic Material Model of Evans

Evans modeled the membrane as a 2D, incompressible, isotropic material [16]. As indicated in equation 2.88 the strain energy density function can be written in terms of the invariants of right Cauchy deformation tensor,  $\mathbf{C}$ . The invariants are given for the 3D right Cauchy deformation tensor in equations 2.89, 2.90 and 2.91. For the 2D tensor the invariants are

$$I_1^*(\mathbf{C}) = \text{tr}\mathbf{C} = \lambda_1^2 + \lambda_2^2 \quad (3.1)$$

$$I_2^*(\mathbf{C}) = \det\mathbf{C} = \lambda_1^2\lambda_2^2. \quad (3.2)$$

The incompressibility condition in the plane indicates that the area remains constant. Considering an infinitesimal square area element in 2D with the edges in the initial configuration,  $dX_1$  and  $dX_2$  becoming a rectangle with the edges  $dx_1$  and  $dx_2$ , the ratio of the final area to the initial area,  $dA_f/dA_0$  can be given as

$$\begin{aligned} \frac{dA_f}{dA_0} &= \frac{dx_1 dx_2}{dX_1 dX_2} \\ &= \lambda_1 \lambda_2 \quad . \end{aligned} \quad (3.3)$$

Here the subscripts 1 and 2 stand for the principal directions. The principal directions 1 and 2 lie in the plane and the principal direction 3, which will be used in the following sections, is directed perpendicular to this plane. Thus, if the initial and final areas are equal (incompressibility constraint) then  $\lambda_1 \lambda_2 = 1$  holds.

Same result can be obtained substituting the appropriate unit normal vector and deformation gradient tensor into the relation given in 2.17:

$$dA_f \begin{Bmatrix} 0 \\ 0 \\ 1 \end{Bmatrix} = dA_0 (\lambda_1 \lambda_2) \begin{pmatrix} 1/\lambda_1 & 0 & 0 \\ 0 & 1/\lambda_2 & 0 \\ 0 & 0 & 1 \end{pmatrix} \begin{Bmatrix} 0 \\ 0 \\ 1 \end{Bmatrix}. \quad (3.4)$$

Note that the unit vectors in the normal direction to the area element are the same and in the third principal direction and the stretch in the third principal direction equals to one. The third row gives the necessary relation between the initial and final areas:

$$dA_f = dA_0 \lambda_1 \lambda_2 \quad (3.5)$$

which is the same with the expression 3.3.

Evans assumed that RBC membrane is an incompressible material such that the second invariant,  $I_2^*$  is equal to one. Then the strain energy density function,  $\Psi_E$  is a function of the first invariant  $I_1^*$  only,

$$\Psi_E = \Psi_E(I_1^*). \quad (3.6)$$

Expanding the strain energy density function in a power series in  $I_1^*$  gives

$$\Psi_E = \sum_{n=1}^{\infty} E_n (I_1^* - 2)^n \quad (3.7)$$

where  $E_n$ 's are the material constants.

Evans [16] claimed that the first term of the power series expansion suffices to represent the strain energy density function of RBC membrane:

$$\Psi_E = E_1 (\lambda_1^2 + \lambda_2^2 - 2). \quad (3.8)$$

In his work Evans also mentioned briefly about the strain energy density function proposed by Skalak et al. for RBC membrane [18]. One of the significant differences between the two strain energy density functions is that Skalak et al. assumed a quadratic function. Evans discussed that linear form of strain energy density function can be successively used for RBC membrane even for very large extension ratios.

The Cauchy stress-stretch relation of an incompressible, isotropic, hyperelastic material in 3D is given in equation 2.113. Remember that  $p$  in this equation is the Lagrange multiplier, which can be identified as the hydrostatic pressure. This term is added to the equation in order to include the effect of the incompressibility constraint. Although there is no deformation due to the hydrostatic pressure acting on the faces of an incompressible unit cubic material element there still exist normal stresses on the faces created by the hydrostatic pressure. Since any value of the hydrostatic pressure cause the same deformation state (namely no deformation) the normal stress values due to this type of loading cannot be obtained from the deformation state.

For a 2D analysis , equation 2.113 becomes,

$$\Sigma_i = -p + \lambda_i \frac{\partial \Psi}{\partial \lambda_i} \quad ; \quad i = 1, 2 \quad ; \quad (\text{no sum}) \quad ; \quad (3.9)$$

where  $\Sigma_i$  is the Cauchy stress resultant per unit length in the  $i$ th-principal direction.

Thus, the constitutive law can be derived from 3.8 using 3.9,

$$\Sigma_i = -p + 2E_1 \lambda_i^2 \quad ; \quad i = 1, 2 \quad ; \quad (\text{no sum}) \quad . \quad (3.10)$$

Using equation 2.49 the Cauchy stress resultant-Green-Lagrange strain relation in the principal directions are given as

$$\Sigma_i = -p_m + 4E_1 \epsilon_i \quad i = 1, 2 \quad , \quad (3.11)$$

with

$$p_m = p + 2E_1. \quad (3.12)$$

In equation 3.11 the only material constant is the variable  $E_1$  which is related to the shear modulus of the material. The in-plane shear modulus,  $\mu$  of this material model can be obtained using the relation

$$\mu = \frac{1}{2} \frac{\partial \Sigma_s}{\partial \gamma_s} \quad (3.13)$$

where  $\Sigma_s$  and  $\gamma_s$  are the in-plane shear stress resultant and strain, respectively given as

$$\Sigma_s = \frac{1}{2}(\Sigma_1 - \Sigma_2) \quad (3.14)$$

$$\gamma_s = \frac{1}{2}(\epsilon_1 - \epsilon_2) = \frac{1}{2}(\lambda_1^2 - \lambda_2^2). \quad (3.15)$$

Using 3.11, 3.13, 3.14 and 3.15 the relation between  $\mu$  and the coefficient  $E_1$  can be obtained,

$$\mu = 2E_1. \quad (3.16)$$

Evans defined the in-plane shear modulus as  $\mu^E = 4E_1$  in his work indicating  $\mu^E = 2\mu$ .

The final form of the constitutive relation can be given as

$$\Sigma_i = -p_m + \mu^E(\lambda_i^2 - 1); \quad i = 1, 2; \quad (\text{no sum}) . \quad (3.17)$$

There is no constant related to the bulk modulus since the material is assumed to be incompressible meaning the bulk modulus is infinite. The term  $p$  is included in 3.10 to add the effect of this *infinity*-bulk modulus.

Evans uses this material model to analyze the cell swelling [16], fluid shear flow and micropipette aspiration experiments [17] where analytical models are employed.

### 3.2. 2D, Compressible, Isotropic, Hyperelastic Material Model of Skalak et al.

Skalak et al. [18] proposed an isotropic, compressible, hyperelastic 2D material model for RBC membrane benefiting from a strain energy density function,  $\Psi_S$ , given as

$$\Psi_S = \frac{B}{4} \left( \frac{I_1^2}{2} + I_1 - I_2 \right) + \frac{C}{8} I_2^2 \quad (3.18)$$

where

$$I_1 = \lambda_1^2 + \lambda_2^2 - 2 \quad (3.19)$$

$$I_2 = \lambda_1^2 \lambda_2^2 - 1 \quad (3.20)$$

and  $B$  and  $C$  are the material constants.

The Cauchy stress-stretch relation of compressible, isotropic, hyperelastic mate-

rials in 3D was given in equation 2.103. The 2D analogous of the formulation is

$$\Sigma_i = J_A^{-1} \lambda_i \frac{\partial \Psi}{\partial \lambda_i} \quad i = 1, 2 \quad (3.21)$$

where  $J_A = \lambda_1 \lambda_2$ .

Hence, the 2D Cauchy stress resultant-stretch relations can be given as

$$\Sigma_1 = \frac{\lambda_1}{\lambda_2} \left[ \frac{B}{2} (\lambda_1^2 - 1) + \frac{C}{2} \lambda_2^2 I_2 \right] \quad (3.22)$$

$$\Sigma_2 = \frac{\lambda_2}{\lambda_1} \left[ \frac{B}{2} (\lambda_2^2 - 1) + \frac{C}{2} \lambda_1^2 I_2 \right] \quad (3.23)$$

Skalak et al. obtained the values of the two constants,  $B$  and  $C$  from the in-plane shear and bulk modulus values available in the literature. By assigning a larger value to the constant  $C$  compared to  $B$  a nearly incompressible material was obtained.

### 3.3. 2D, Compressible, Isotropic, Hyperelastic Material Model of Evans et al.

As stated before, from the experiments conducted with RBC it is observed that the deformation behavior of RBC membrane under constant surface area differs from the dilatational one. Forces which must be applied in order to achieve a deformation causing a surface area increase are comparatively much greater than the ones to cause a deformation with constant surface area. Therefore, an elastic constitutive equation separating the effects of changes in area from extensional deformation at constant area is needed [29]. This type of material model is a 2D analog of rubber. Rubber greatly resists volume changes as indicated by its large volumetric compressibility (bulk) modulus, but is capable of very large extensions at nearly constant volume due to its comparatively low shear modulus. Similarly, RBC membrane greatly resists surface

area changes whereas very large extensions at nearly constant surface area is possible.

In the light of the above discussion the Cauchy stress resultant,  $\Sigma$  is the sum of two stress resultant components: 1) a dilatational stress resultant,  $\Sigma^\alpha$  and 2) stress resultant due to the extensional deformation at constant surface area,  $\Sigma^\beta$ :

$$\Sigma = \Sigma^\alpha + \Sigma^\beta \quad . \quad (3.24)$$

Considered in terms of the stress resultant components  $\Sigma^\alpha$  and  $\Sigma^\beta$ , the second term in equation 3.10 is the stress resultant due to the extensional deformation at constant surface area. This expression is used for the stress resultants in the principal directions due to the extensional deformation at constant surface area in the present material model such that

$$\Sigma_i^\beta = \mu \lambda_i^2 ; \quad i = 1, 2 ; \quad (\text{no sum}) \quad (3.25)$$

holds.

Evans and Skalak proposed that  $\Sigma_\alpha$  can be approximated with a Taylor series expansion in the fractional change in area,  $\alpha$  by

$$\Sigma^\alpha = \Sigma_0^\alpha + K\alpha + O(\alpha^2) + \dots \quad , \quad (3.26)$$

where  $\Sigma_0^\alpha$  is the dilatational stress resultant in the initial state,  $K$  is the in-plane bulk modulus and the function  $O(x)$  stands for the higher order terms in the sum [29].

$\alpha$  is the fractional change in area,  $(dA_f - dA_0)/dA_0$  where  $dA_f$  and  $dA_0$  are the final and initial areas, respectively. Using equation 3.3 the fractional change in area

can be given as

$$\begin{aligned}\alpha &= \frac{dA_f - dA_0}{dA_0} \\ &= \lambda_1 \lambda_2 - 1 \quad .\end{aligned}\tag{3.27}$$

Assuming that the initial equilibrium state of the membrane is stress free ( $\Sigma_0^\alpha = 0$ ) and that the fractional area change  $\alpha$  is small such that the higher order terms in equation 3.26 can be neglected, the constitutive relations of the present material model in the principal directions are

$$\Sigma_1 = K\alpha + \mu\lambda_1^2\tag{3.28}$$

and

$$\Sigma_2 = K\alpha + \mu\lambda_2^2 \quad .\tag{3.29}$$

The assumption that the fractional area change  $\alpha$  is small should be checked after the analysis to prove the validity of the constitutive relations 3.28 and 3.29.

This constitutive relation is similar to the one given in equation 3.10. The difference between the two models is that the present model does not assume the material as incompressible but nearly incompressible. The Lagrange multiplier,  $p$  in equation 3.10 is replaced by a term including the in-plane bulk modulus,  $K$  to add the effect of area expansion into the constitutive relation. The choice of a significantly larger value for in-plane bulk modulus,  $K$  compared to the in-plane shear modulus,  $\mu$  provides that the area of the membrane remains almost constant if no large isotropic stress resultants exist. So, a nearly incompressible material model is obtained.

Using 3.27 in 3.28 and 3.29, the constitutive relations in the principal directions

become

$$\Sigma_1 = K(\lambda_1\lambda_2 - 1) + \mu\lambda_1^2 \quad (3.30)$$

and

$$\Sigma_2 = K(\lambda_1\lambda_2 - 1) + \mu\lambda_2^2 \quad . \quad (3.31)$$

The above constitutive relations are used by Evans et al. to investigate the value of the in-plane bulk modulus,  $K$  of RBC membrane by constructing an analytical model for micropipette aspiration experiment of preswollen RBC's [30].

### 3.4. 3D, Incompressible, Isotropic, Hyperelastic Material Model of Neo-Hookean Strain Energy Density Function

Recently, Dao et al. [5] used the optical tweezer method to deform RBC and employed the isotropic, incompressible neo-Hookean material model in 3D for cell membrane,

$$\Psi_{NH} = G(\lambda_1^2 + \lambda_2^2 + \lambda_3^2 - 3) \quad (3.32)$$

where  $G$  is the elastic material constant.

The incompressibility constraint in 3D means that the material volume remains constant throughout the deformation process and the Jacobian,  $J$  of the deformation gradient tensor equals to unity (see equation 2.12).

Although Dao et al. used this material model in the FE analysis of optical tweezer deformation it does not represent the material characteristics of RBC membrane properly. As mentioned before RBC membrane conserves its surface area. If an in-plane deformation to a sheet of neo-Hookean material with the same thickness of RBC mem-

brane is applied then the surface area increases where the thickness decreases such that its volume is conserved. Hence, large in-plane deformations cause large increases in surface area if 3D, incompressible, isotropic, hyperelastic material models are used.

### 3.5. Comparison of 2D and 3D Isotropic Hyperelastic Material Models

As stated in the previous sections, 2D and 3D isotropic hyperelastic material models are used to represent the material behavior of RBC membrane. Previous studies have shown that the membrane is highly resistant to an isotropic (biaxial) surface stretch but would readily stretch in one direction [4, 13, 14]. This means that the membrane would resist to surface area increase which is the case by isotropic stretching. On the other hand, it would deform easier by uniaxial stretching where the force needed for this type of loading would be much less than the one needed by isotropic stretching and the surface area is almost constant.

To make a comparison between the 2D and 3D, isotropic, hyperelastic material models 2D, nearly incompressible, isotropic, hyperelastic material model given in section 3.3 and 3D, incompressible, isotropic, hyperelastic material model of neo-Hookean strain energy density function (see section 3.4) are chosen as representative examples. The material constants of the 2D material model are  $K = 500 \text{ mN/m}$  and  $\mu = 0.0035 \text{ mN/m}$  which are in the range of values given in literature. The single material constant,  $G$  of neo-Hookean type material is chosen as 5 kPa which is also comparable with the estimated values of previous studies [5, 25].

The deformation behavior of the 2D hyperelastic material model by isotropic and uniaxial stretching are given in figures 3.1 and 3.2, whereas the ones of the neo-Hookean material are given in 3.3 and 3.4. Note that the first vertical axes in figures 3.1 and 3.2 stand for the first principal stress resultant,  $\Sigma_1$  where the ones in figures 3.3 and 3.4 stand for the first principal stress,  $\sigma_1$ . In these figures not the stress and the stress resultant values but the orders of them are the important point. For the 3D hyperelastic material, the stresses in isotropic and uniaxial tension are in the same order which is not the case for the RBC membrane but are six orders of magnitude different

for the 2D hyperelastic material. Moreover, another striking difference can be realized in fractional area changes. The isotropic tension causes surface area change for both material models which is expected. But this is not the case for uniaxial tension where area remains almost constant for 2D hyperelastic material. The 3D, incompressible, isotropic, hyperelastic material model results in an area increase by uniaxial stretching since the thickness of the material decreases and the volume is preserved. Thus, it can be concluded that the 3D, incompressible, isotropic, hyperelastic materials are not a good choice to represent the RBC membrane, especially in large deformations.

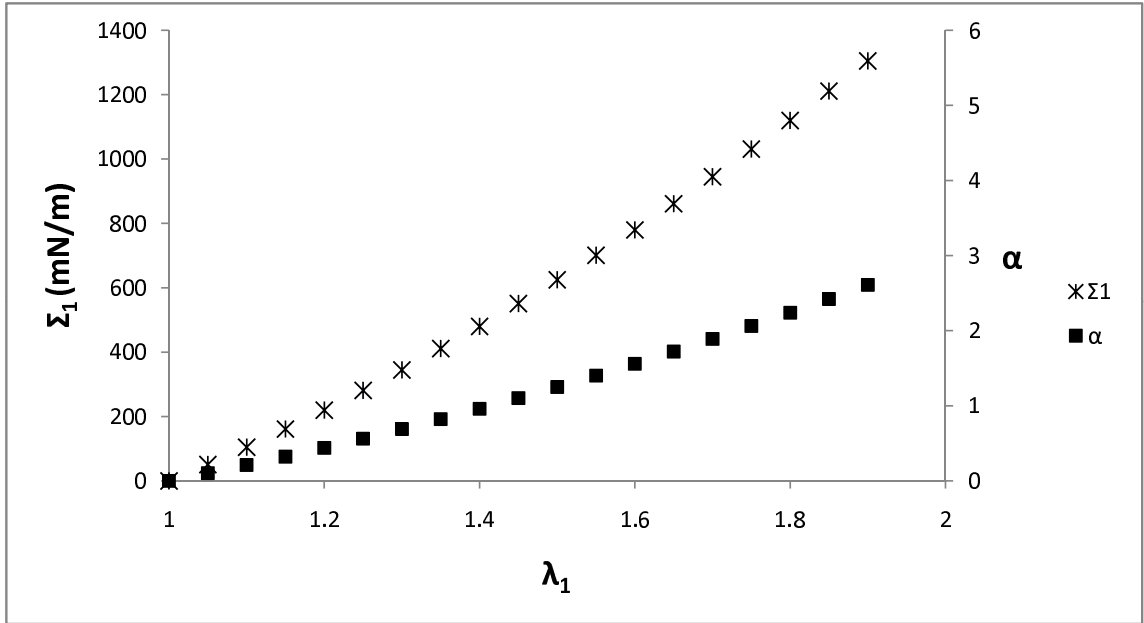


Figure 3.1. Stress resultant in the first principal direction,  $\Sigma_1$  and fractional area change,  $\alpha$  by isotropic (biaxial) tension ( $\Sigma_1 = \Sigma_2$ ) for 2D, nearly incompressible, isotropic, hyperelastic material described in section 3.3

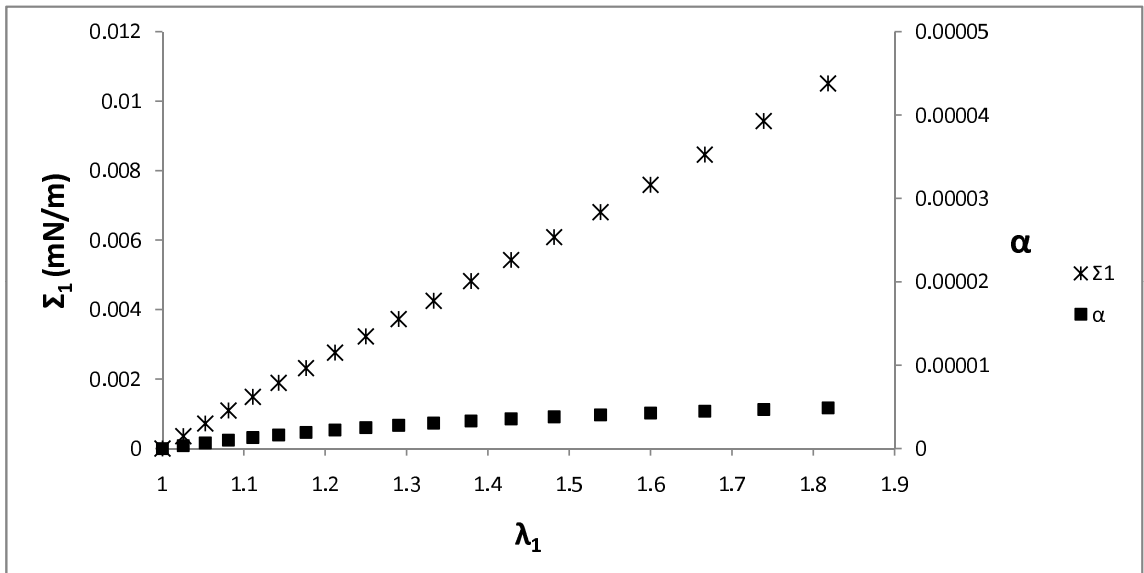


Figure 3.2. Stress resultant in the first principal direction,  $\Sigma_1$  and fractional area change,  $\alpha$  by uniaxial tension ( $\Sigma_2 = 0$ ) for 2D, nearly incompressible, isotropic, hyperelastic material described in section 3.3

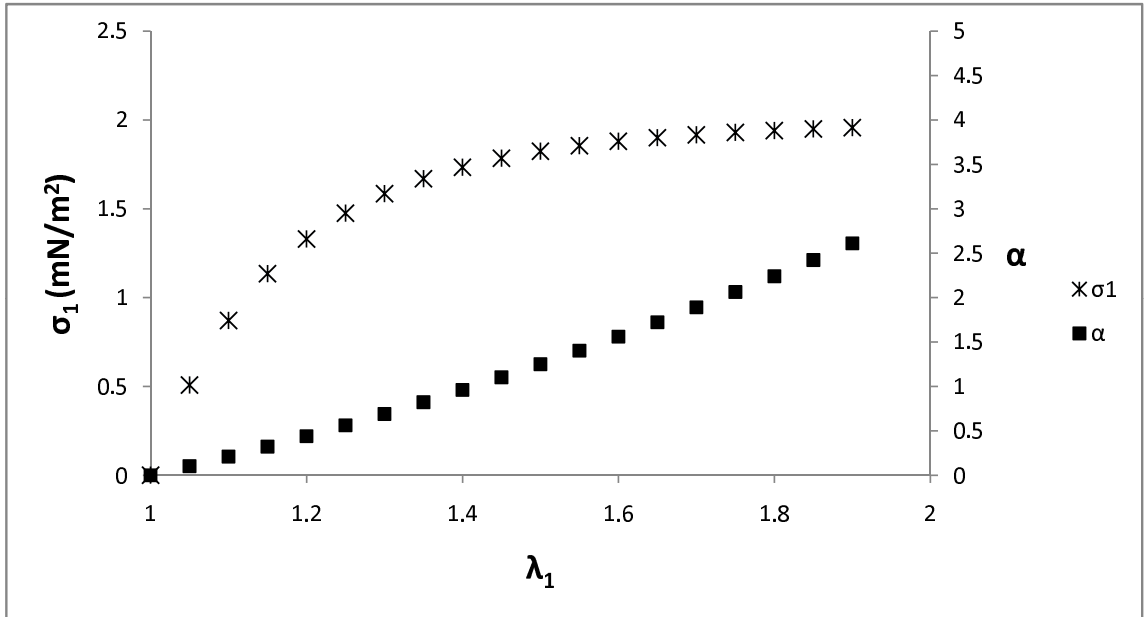


Figure 3.3. Stress in the first principal direction,  $\sigma_1$  and fractional area change,  $\alpha$  by isotropic (biaxial) tension ( $\sigma_1 = \sigma_2$ ) for 3D, incompressible, isotropic, neo-Hookean hyperelastic material described in section 3.4

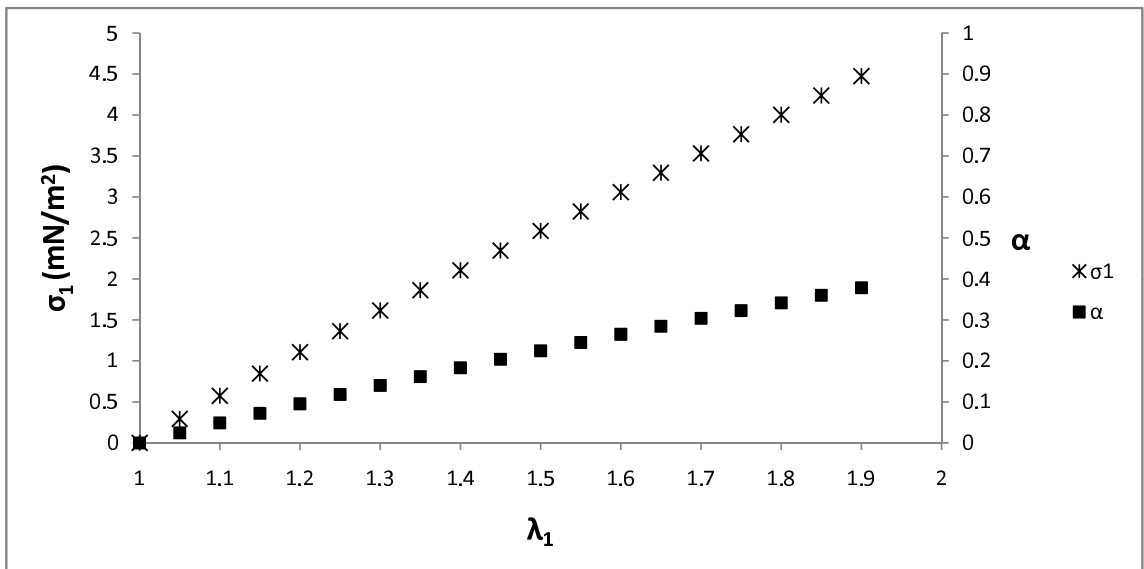


Figure 3.4. Stress in the first principal direction,  $\sigma_1$  and fractional area change,  $\alpha$  by uniaxial tension ( $\sigma_2 = 0$ ) for 3D, incompressible, isotropic, neo-Hookean hyperelastic material described in section 3.4

## 4. MODELS FOR THE DEFORMATION OF FLACCID RBC BY MICROPIPETTE ASPIRATION

### 4.1. Analytical Models

#### 4.1.1. Infinite Plane Membrane Model of Evans

Evans studied micropipette aspiration of flaccid RBC where the suction of an infinite plane into a cylindrical micropipette was used as the model [17] (see graph 1.7). This model is valid for small pipettes and for thin discocytes aspirated in the central region which is assumed to be relatively flat compared to the peripheral portion of the cell. Additionally, the model is just suitable for the experiments where the portion of the cell outside the pipette remains flat throughout the experiment and the sucked portion leans tightly to the pipette's wall. So, the model is valid for cells with nonspherical outside portion and if no buckling occurs inside the pipette. Another assumption is that there exists no frictional force between the pipette wall and the aspirated cell membrane.

Evans benefited from the membrane theory to analyze the experiment. Membrane theory is one of the two distinct theories used in the analysis of shell-like structures. In this theory the structure is considered as incapable of conveying moments whose effects are included in the other theory, namely the bending or general theory [31]. Additionally, out-of-plane stresses are negligible in the case of shells and membranes and are not included in the equilibrium equations. Therefore, the analysis reduces to a plane stress case.

The geometry of pipette, shapes RBC undergo in the experiment and the loading are axisymmetric. Therefore, Evans used the mechanical equilibrium equations of the membrane theory for axisymmetric membrane surfaces which relates the in-plane stress

resultants,  $\Sigma_{ij}$ , to the external forces exerted on the membrane [29],

$$\frac{\partial \Sigma_{\phi\phi}}{\partial \phi} + \frac{\partial(\Sigma_{\phi m} r)}{\partial s} + \Sigma_{\phi m} \frac{\partial r}{\partial s} + \sigma_{\phi} r = 0 \quad (4.1)$$

$$\frac{\partial(\Sigma_{mm} r)}{\partial s} + \frac{\partial \Sigma_{\phi m}}{\partial \phi} - \Sigma_{\phi\phi} \frac{\partial r}{\partial s} + \sigma_m r = 0 \quad (4.2)$$

$$\frac{\Sigma_{mm}}{R_m} + \frac{\Sigma_{\phi\phi}}{R_{\phi}} = \Delta P \quad (4.3)$$

where  $\Delta P$  is the pressure difference across the membrane (inside minus outside pressure) and  $\sigma_{\phi}$  and  $\sigma_m$  are the shear stresses applied on surface of membrane. The subscripts  $m$  and  $\phi$  denote the meridional and the azimuthal ones, respectively and due to the axisymmetric nature of the problem, are the principal directions.  $r$  is the radial coordinate (see figure 1.7) whereas  $\phi$  is the azimuthal coordinate.  $s$  is the curvilinear coordinate along the meridian.  $R_m$  and  $R_{\phi}$  are the radii of the membrane surface in the meridional and azimuthal directions.

For axisymmetric loading of the membrane, the shear stress,  $\sigma_{\phi}$  and shear force resultant,  $\Sigma_{\phi m}$  are zero. So, the equilibrium equations reduce to

$$\frac{d(\Sigma_{mm} r)}{ds} - \Sigma_{\phi\phi} \frac{dr}{ds} + \sigma_m r = 0 \quad (4.4)$$

$$\frac{\Sigma_{mm}}{R_m} + \frac{\Sigma_{\phi\phi}}{R_{\phi}} = \Delta P. \quad (4.5)$$

If  $\sigma_m$  equals to zero then the solutions to the equations 4.4 and 4.5 are

$$\Sigma_{mm} = \frac{\Delta P R_{\phi}}{2} \quad (4.6)$$

and

$$\Sigma_{\phi\phi} = \frac{(2/R_\phi - 1/R_m)}{2} R_\phi^2 \Delta P. \quad (4.7)$$

There are three cell portions to be analyzed: the cap, the cylindrical portion, and the outside portion which is assumed to be flat. For the cap, equations 4.6 and 4.7 give the stress resultants. For the cylindrical portion, the stress resultant  $\Sigma_{mm}$  remains constant since no friction between the pipette wall and the membrane is assumed. Finally, the equilibrium equation for the plane outside can be obtained from equations 4.4 and 4.5 noting that  $dr = ds$ ,  $1/R_m = 1/R_\phi = 0$ , and  $\Delta P = 0$ ,

$$\Sigma_{mm} - \Sigma_{\phi\phi} + r \frac{d\Sigma_{mm}}{dr} = 0. \quad (4.8)$$

The constitutive relation for the red cell membrane proposed by Evans [16] and given in 3.11 is modified using the relation  $\mu^E = 4E_1$ ,

$$\Sigma_{mm} = -p_m + \mu^E \epsilon_{mm} \quad (4.9)$$

$$\Sigma_{\phi\phi} = -p_m + \mu^E \epsilon_{\phi\phi} \quad (4.10)$$

where the Green-Lagrange strains  $\epsilon_{mm}$  and  $\epsilon_{\phi\phi}$  are obtained from 2.49 as

$$\epsilon_{mm} = \frac{1}{2}(\lambda_{mm}^2 - 1) \quad (4.11)$$

$$\epsilon_{\phi\phi} = \frac{1}{2}(\lambda_{\phi\phi}^2 - 1). \quad (4.12)$$

The material model used by Evans [16] is assumed to be incompressible in 2D meaning that there is no change in the membrane surface area due to the deformation. So, the product of the stretch ratios in the principal directions equals to one,

$$\lambda_{mm}\lambda_{\phi\phi} = 1 \quad (4.13)$$

and the stretch ratio in the radial direction can be written in terms of the azimuthal one,

$$\lambda_{mm} = \frac{1}{\lambda_{\phi\phi}}. \quad (4.14)$$

Then, equation 4.12 becomes

$$\epsilon_{\phi\phi} = \frac{1}{2}(\lambda_{mm}^{-2} - 1). \quad (4.15)$$

The stretch ratio  $\lambda_{\phi\phi}$  is given by the ratio of the deformed circle circumference to the undeformed circle circumference at the same material location,

$$\lambda_{\phi\phi} = \frac{2\pi r}{2\pi r_0} = \frac{r}{r_0}, \quad (4.16)$$

$r_0$  being the radius in the undeformed state.

Thus,  $\lambda_{mm}$  can be given as

$$\lambda_{mm} = \frac{1}{\lambda_{\phi\phi}} = \frac{r_0}{r}. \quad (4.17)$$

In terms of equations 4.9 to 4.12 and 4.15 to 4.17, equation 4.8 becomes,

$$\frac{1}{2} \left[ \left( \frac{r_0}{r} \right)^2 - \left( \frac{r}{r_0} \right)^2 \right] + \frac{r_0}{r} \frac{dr_0}{dr} - \left( \frac{r_0}{r} \right)^2 - \frac{r}{\mu^E} \frac{dp_m}{dr} = 0. \quad (4.18)$$

Deformed and undeformed elemental areas located on the plane region outside the pipette should be equal.

$$r_0 dr_0 d\phi = r dr d\phi \quad (4.19)$$

Eliminating the  $d\phi$  terms, equation 4.19 becomes

$$\frac{dr_0}{dr} = \frac{r}{r_0}. \quad (4.20)$$

Equation 4.20 can be used in equation 4.18 to obtain

$$2 - \left( \frac{r_0}{r} \right)^2 - \left( \frac{r}{r_0} \right)^2 = \frac{2r}{\mu^E} \frac{dp_m}{dr}. \quad (4.21)$$

Since the material is considered as incompressible, deformed and undeformed total membrane areas are equal and the radius  $r$  in the deformed state is related to the undeformed radius  $r_0$  by

$$\pi r_0^2 = A_{CAP} + A_{CYL} + \pi(r^2 - R_P^2) \quad (4.22)$$

where  $A_{CAP}$  and  $A_{CYL}$  are the surface areas of the cap and the cylinder portion, respectively and  $R_P$  is the pipette radius.

Now define

$$A' = \frac{A_{CAP} + A_{CYL} - \pi R_P^2}{\pi}. \quad (4.23)$$

So, equation 4.22 becomes

$$r_0^2 = A' + r^2. \quad (4.24)$$

Using 4.24, 4.21 becomes

$$2 - \frac{A' + r^2}{r^2} - \frac{r^2}{A' + r^2} = \frac{2r}{\mu^E} \frac{dp_m}{dr}. \quad (4.25)$$

Equation 4.25 can be integrated to obtain

$$\left[ \ln r + \frac{A'}{2r^2} - \frac{1}{2} \ln(A' + r^2) \right]_{\infty}^{R_P} = 2 \frac{p_m(R_P) - p_m(\infty)}{\mu^E}. \quad (4.26)$$

It is assumed that the outside portion remains relaxed. Hence, the value of  $p_m(\infty)$  is taken as zero.

$$\frac{A'}{2R_P^2} - \frac{1}{2} \ln \left( \frac{A' + R_P^2}{R_P^2} \right) = 2 \frac{p_m(R_P)}{\mu^E}. \quad (4.27)$$

Equation 4.9 can be used to obtain the stress resultant in the radial direction at the pipette tip,

$$\Sigma_{mm}(R_P) = -p_m(R_P) + \mu^E \epsilon_{mm}(R_P). \quad (4.28)$$

The radial Lagrangian strain is obtained from 4.11 by using 4.17 and 4.24,

$$\epsilon_{mm}(R_P) = \frac{A'}{2R_P^2}. \quad (4.29)$$

The final form of  $\Sigma_{mm}(R_P)$  is obtained from 4.28 with the help of 4.27 and 4.29,

$$\Sigma_{mm}(R_P) = \frac{\mu^E}{4} \left[ \frac{A'}{R_P^2} + \ln \left( 1 + \frac{A'}{R_P^2} \right) \right]. \quad (4.30)$$

As indicated before,  $\Sigma_{mm}$  is constant in the cylindrical portion of the membrane. Equations 4.6 and 4.30 should be equal for the radial stress resultant at the cap-cylinder junction,

$$2 \frac{\Delta P R_P}{\mu^E} = \frac{A'}{R_P^2} + \ln \left( 1 + \frac{A'}{R_P^2} \right). \quad (4.31)$$

Equation 4.31 relates the aspirated area to the pressure difference required to suck the membrane into the pipette. Evans assumed a spheroidal cap which is a half-ellipse in cross section and obtained  $\Delta P R_P / \mu^E$  as a function of  $D/R_P$ .

#### 4.1.2. Infinite Plane Membrane Model of Chien et al. (Spherical Cap Model)

Chien et al. [24] also analyzed the micropipette aspiration of red blood cell. Their analytical approach was very similar to the Evans' one [16]. The work of Chien et al. diverge from the Evans' analysis at three important points. First, the in-plane shear modulus,  $\mu^C$ , they used is equal to one-half of  $\mu^E$ . So, the constitutive relations used in this paper are

$$\Sigma_{mm} = -p_m + \frac{\mu^C}{2} \epsilon_{mm} \quad (4.32)$$

$$\Sigma_{\phi\phi} = -p_m + \frac{\mu^C}{2}\epsilon_{\phi\phi}. \quad (4.33)$$

Secondly, they used equation 4.8 to obtain an expression for  $\Sigma_{mm}$  where Evans used this equation to get an expression for the term,  $p_m$  in his constitutive relations (see equation 4.26). Then they equated the stress resultant  $\Sigma_{mm}$  at the cap-cylinder junction (equation 4.6) to this expression,

$$\frac{R_P \Delta P}{2} = \int_{R_P}^{\infty} (\Sigma_{mm} - \Sigma_{\phi\phi}) \frac{dr}{r}. \quad (4.34)$$

The integral on the left hand side of 4.34 can be evaluated using equations 4.11, 4.15, 4.17, 4.24, 4.32 and 4.33.

$$\int_{R_P}^{\infty} (\Sigma_{mm} - \Sigma_{\phi\phi}) \frac{dr}{r} = \int_{R_P}^{\infty} \mu^C \left( \frac{r_0^2}{r^3} - \frac{r}{r_0^2} \right) dr \quad (4.35)$$

$$\int_{R_P}^{\infty} \mu^C \left( \frac{r_0^2}{r^3} - \frac{r}{r_0^2} \right) dr = \mu^C \int_{R_P}^{\infty} \left( \frac{A' + r^2}{r^3} - \frac{r}{A' + r^2} \right) dr \quad (4.36)$$

$$\mu^C \int_{R_P}^{\infty} \left( \frac{A'}{r^3} + \frac{1}{r} - \frac{r}{A' + r^2} \right) dr = \frac{\mu^C}{2} \left[ -\frac{A'}{r^2} + 2 \ln r - \ln(A' + r^2) \right]_{R_P}^{\infty} \quad (4.37)$$

$$\frac{\mu^C}{2} \left[ -\frac{A'}{r^2} + 2 \ln r - \ln(A' + r^2) \right]_{R_P}^{\infty} = \frac{\mu^C}{2} \left[ \frac{A'}{R_P^2} + \ln \left( \frac{A' + R_P^2}{R_P^2} \right) \right] \quad (4.38)$$

Thus, equation 4.34 becomes,

$$\frac{R_P \Delta P}{\mu^C} = \frac{A'}{R_P^2} + \ln \left( 1 + \frac{A'}{R_P^2} \right). \quad (4.39)$$

Expressions 4.31 and 4.39 are the same noting that the shear modulus  $\mu^C$  is equal to one-half of the shear modulus  $\mu^E$ .

The last difference of the analysis of Chien et al. is that they assumed the cap geometry as hemispherical. With this assumption equation 4.23 becomes

$$A' = \frac{2\pi R_P^2 + 2\pi R_P(D - R_P) - \pi R_P^2}{\pi} \quad (4.40)$$

$$A' = 2R_P D - R_P^2. \quad (4.41)$$

Using equation 4.41, the relation between  $\Delta P R_P / \mu^C$  and  $D / R_P$  can be obtained from 4.39 easily,

$$\frac{R_P \Delta P}{\mu^C} = \frac{2D}{R_P} - 1 + \ln \left( \frac{2D}{R_P} \right). \quad (4.42)$$

## 4.2. FE Analysis

Higuchi and Kanno analyzed an RBC and an spherocyte subjected to micropipette aspiration experiment by FEM [25]. They modeled the membrane complex as an effective continuum material with the 3D, incompressible, hyperelastic material model of Arruda-Boyce form of strain energy potential. The RBC geometry used in the work is the one proposed by Evans and Fung [15] who estimated the biconcave shape of RBC (see figure 4.1) by the equation given as

$$y = \pm 0.5 R_0 \left[ 1 - \frac{x^2 + z^2}{R_0^2} \right]^{0.5} \left[ C_0 + C_1 \frac{x^2 + z^2}{R_0^2} + C_2 \left( \frac{x^2 + z^2}{R_0^2} \right)^2 \right] \quad (4.43)$$

with  $R_0 = 3.91 \mu m$ ,  $C_0 = 0.207161$ ,  $C_1 = 2.002558$  and  $C_2 = -1.122762$  where  $R_0$  is the RBC radius. Higuchi and Kanno did small (nano-order) deformation analysis

of the experiment and obtained stress distribution and displacements occurring in the membrane.

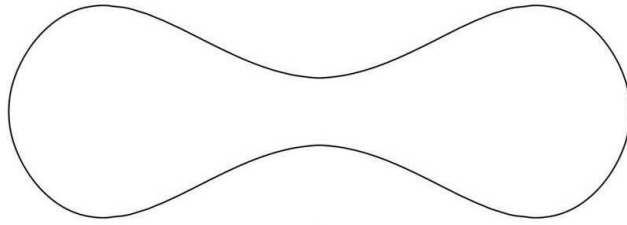


Figure 4.1. Cross section of RBC biconcave shape estimated by Evans and Fung [15]

## 5. PRESENT FE ANALYSIS

The micropipette aspiration experiment of flaccid RBC is analyzed using finite element package ABAQUS. Three different geometric models representing the undeformed flaccid RBC are used for this purpose. The first one is the "Infinite Plane Membrane Model" (figure 5.1) where the undeformed RBC geometry is modeled as an infinite plane as done by the analytical analyses in literature. This model provides a direct comparison of the computational results with the analytical ones. Second geometric model for the flaccid RBC is the so called "Disk Model" where the cross section of this geometric model is shown in figure 5.4. The last model is the "Modified Biconcave Model" (figure 5.8) which is a modified version of the biconcave RBC shape (figure 4.1) proposed by Evans and Fung [15].

Since the geometry of the flaccid RBC and the pipette and the loading condition by micropipette aspiration experiment is axisymmetric an axisymmetric FE analysis is performed. Therefore, all three geometrical models mentioned are axisymmetric models.

In all three computational models the inner radius of the pipette is taken as  $0.45 \mu m$  in order to be able to compare the results with the experimental ones given in [32]. A fillet of radius of  $0.05 \mu m$  is added to the pipette tip for convergence issues.

An axisymmetry boundary condition is applied to the node or nodes located on the symmetry line. The pipette is modeled as a rigid body and encastered. A negative pressure (suction pressure) is applied on the portion of the membrane located inside the pipette which caused the partial aspiration of the membrane into the pipette. The tangential behavior of the interaction between the micropipette and membrane is assumed to be frictionless in all models.

Convergence check is done for all computational models and suitable element sizes are chosen. The 2-node, linear, axisymmetric shell elements, SAX1 are used for the cell membrane.

The material model described in the section 3.3 is implemented to ABAQUS with the aid of the user subroutine *UGENS* where linear or nonlinear constitutive relations of a shell section can be programmed. The nonlinear geometry option is used for the inclusion of the nonlinear effects of large displacements. As it can be seen in the equations 3.30 and 3.31, the material constants are the in-plane shear modulus,  $\mu$  and the in-plane bulk modulus,  $K$ . The bending stiffness of the membrane is neglected and only in-plane elasticity is taken into consideration as it was done in the analytical models in literature.

### 5.1. Infinite Plane Membrane Model

In the infinite plane membrane model, flaccid RBC which is to be aspirated into micropipette is taken as an infinite plane membrane (see figure 5.1). The membrane plane is modeled large enough (with a radius of  $5 \mu m$ ) to represent an infinite one. The axisymmetric FE model used for this geometry is given in figure 5.3.

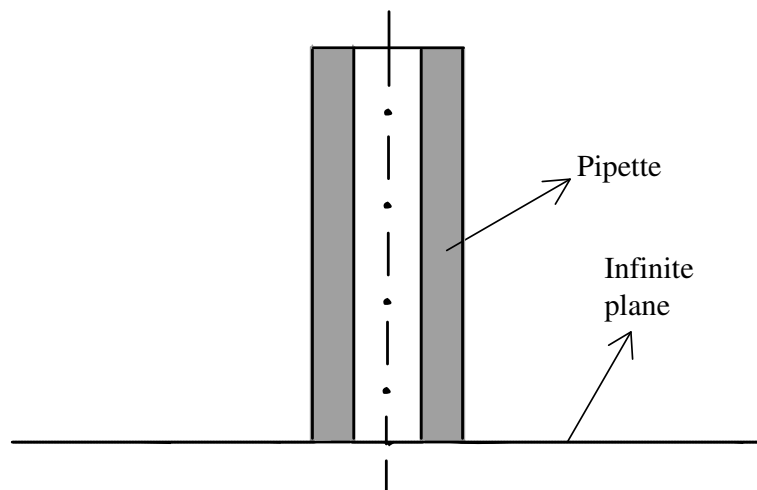


Figure 5.1. Cross section of the infinite plane membrane model at the initial state

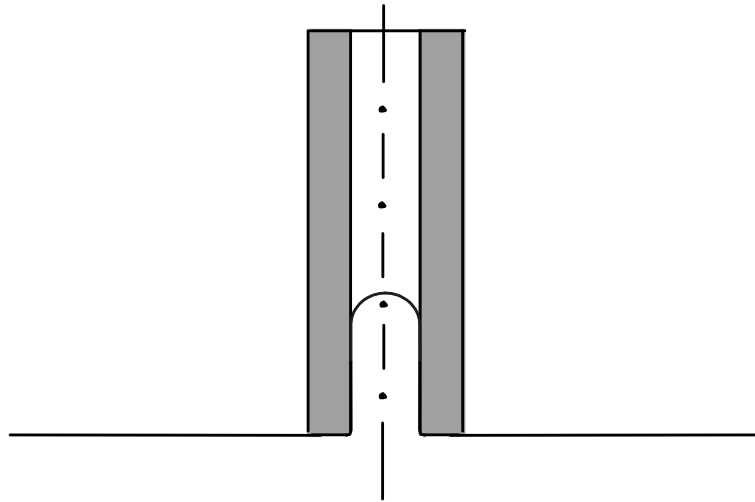


Figure 5.2. Cross section of the infinite plane membrane model at the deformed state

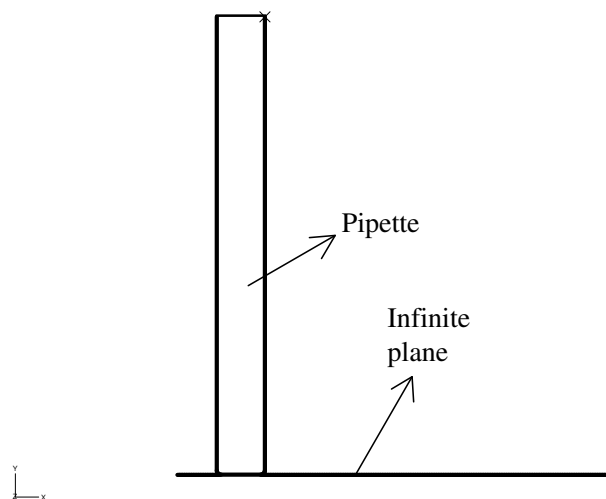


Figure 5.3. Axisymmetric FE model for infinite plane geometry

## 5.2. Disk Model

The so-called disk model is an evaluated version of the infinite plane model enclosing a volume inside (figure 5.4). In the model the top and bottom faces are still flat. The distance between these faces are  $1 \mu m$  and the radii of faces are  $3.5 \mu m$ . The axisymmetric FE model used for the disk geometry is given in figure 5.6.

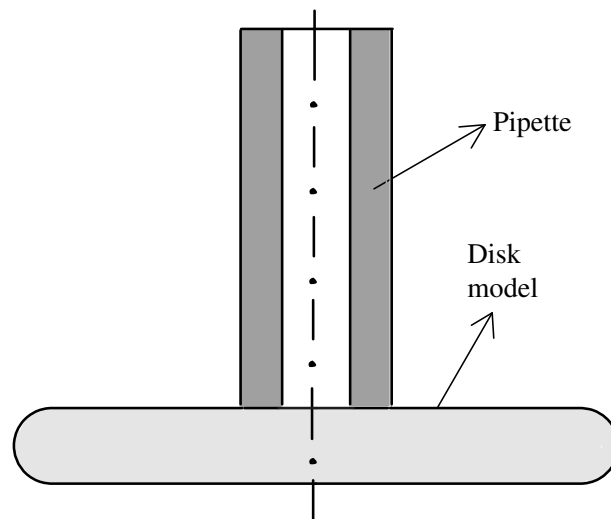


Figure 5.4. Cross section of the disk model at the initial state

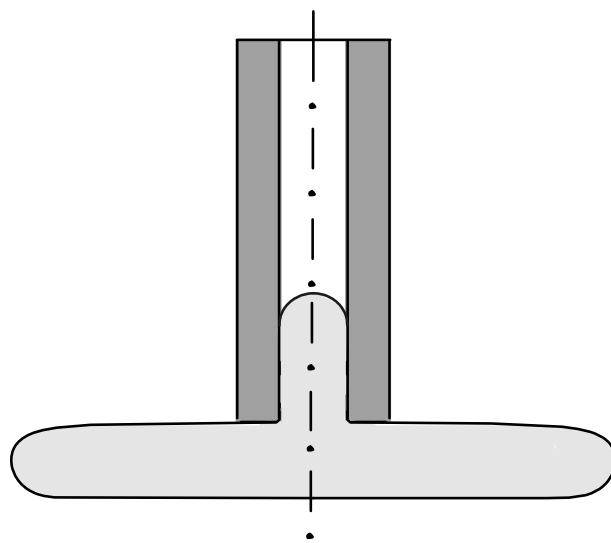


Figure 5.5. Cross section of the disk model at the deformed state

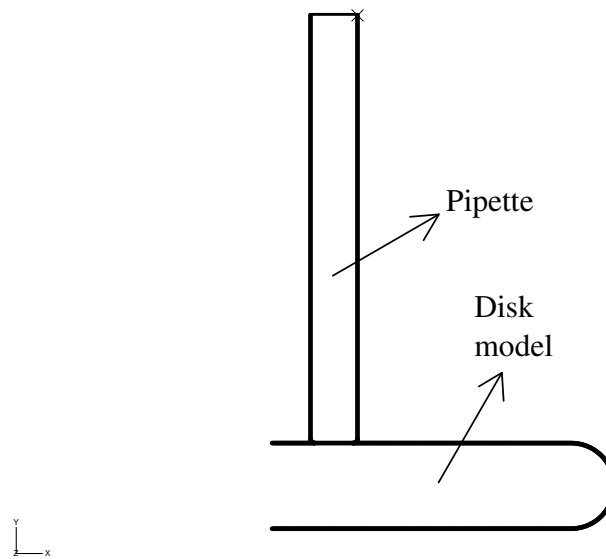


Figure 5.6. Axisymmetric FE model for the disk geometry

### 5.3. Modified Biconcave Model

The modified biconcave model is the most realistic geometry for flaccid biconcave RBC shape. The starting geometry for this model is the estimated shape for biconcave RBC proposed by Evans and Fung [15]. The modified part is the portion inside the pipette. This portion is modeled flat which is curved in the biconcave RBC geometry of Evans and Fung (see figure 5.7). This modification enables the direct comparison of the results obtained from the simulations with this model and the ones with the infinite plane and disk models. Additionally, this geometrical modification helps to convergence of simulations. The axisymmetric FE model used for this geometry is given in figure 5.10.

This geometric model is first simulated without cytosol and then with cytosol. To model the cytosol inside the RBC axisymmetric hydrostatic fluid elements with two nodes, namely FAX2 elements are used.

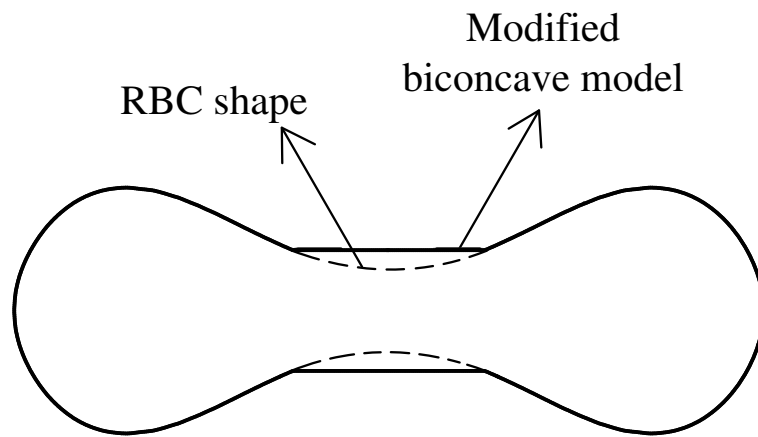


Figure 5.7. Modified biconcave model and the RBC geometry proposed by Evans and Fung

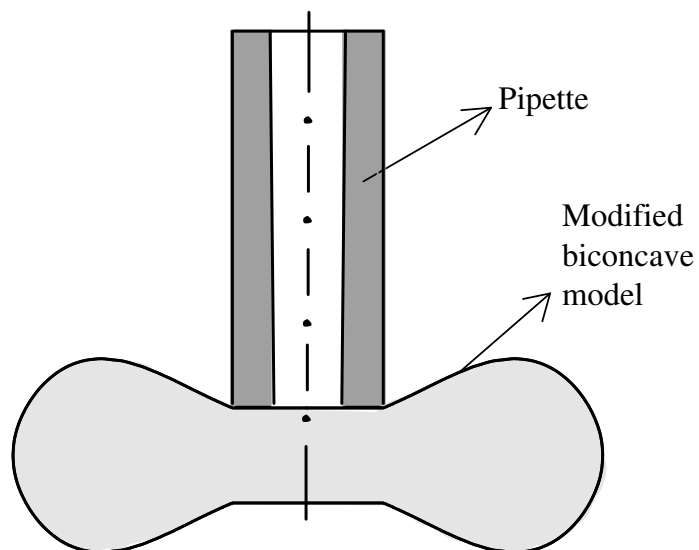


Figure 5.8. Cross section of the modified biconcave model at the initial state

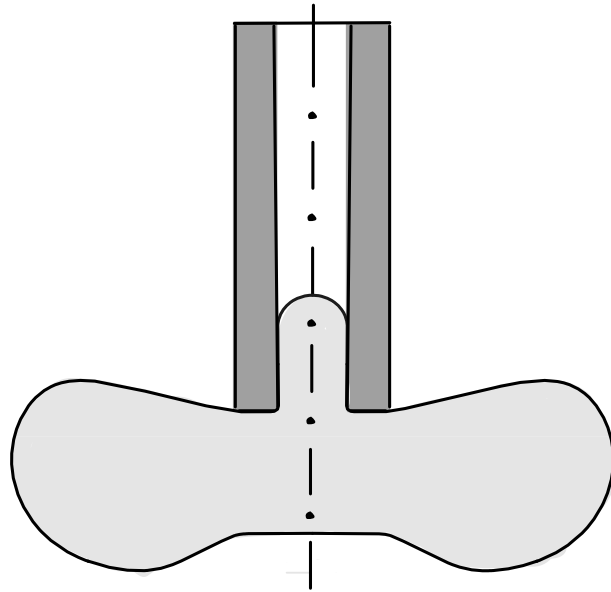


Figure 5.9. Cross section of the modified biconcave model at the deformed state

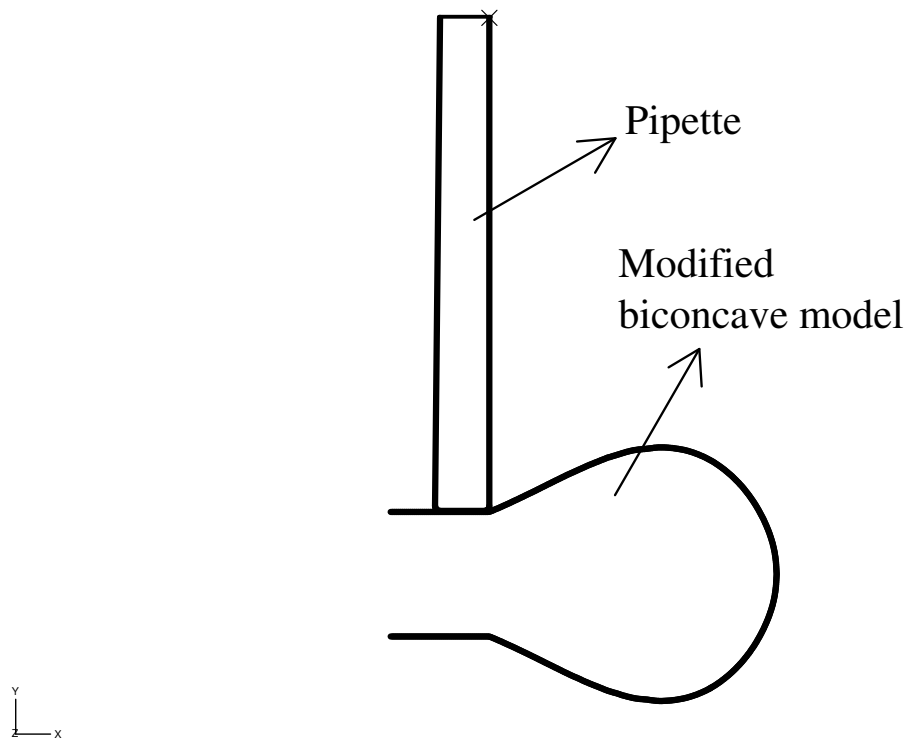


Figure 5.10. Axisymmetric FE model for the modified biconcave geometry

## 6. RESULTS

Typical values in literature for in-plane shear modulus,  $\mu$  are in the range of  $3\text{-}5 \cdot 10^{-3} \text{ mN/m}$  whereas for in-plane bulk modulus,  $K$  much higher values like  $500 \text{ mN/m}$  are estimated [4, 8, 9]. This  $K$  value is  $10^5$  times larger than the value for  $\mu$ . This means that RBC membrane is a nearly incompressible material which can deform easily keeping its surface area constant.

To be able to compare the FE results with the results in literature  $\Delta P \cdot R_p$  vs.  $D/R_p$  graphs are obtained. Graphs for different  $K$  and  $\mu$  values are computed in the FE simulations. There are various articles from where experimental data and analytical results for MA of flaccid RBC experiment can be obtained [32, 17, 24]. All of them resulted in similar  $\Delta P \cdot R_p$  vs.  $D/R_p$  graphs. The article of Evans and La Celle is the one chosen for the comparison since it contains the info of inner pipette radius [32].

The effects of the two elastic material constants,  $K$  and  $\mu$  are investigated where one of the constants varies and the other one is constant. Additionally, the fractional area change,  $\alpha$ , the stretches and stress resultants in the first and second principal directions,  $\lambda_1$ ,  $\lambda_2$ ,  $\Sigma_1$  and  $\Sigma_2$ , respectively, after the deformation are also computed for all geometric models where the principal direction 1 is the meridional direction and the principal direction 2 is the circumferential direction.

### 6.1. Infinite Plane Membrane Model

The  $\Delta P \cdot R_p$  vs.  $D/R_p$  graph obtained from the FE simulations of infinite plane membrane model for the elastic material constants  $K = 500 \text{ mN/m}$  and  $\mu = 3 \cdot 10^{-3} \text{ mN/m}$  is given in figure 6.1 with the experimental results obtained by Evans and La Celle [32]. These values for  $K$  and  $\mu$  give the curve which fits the experimental data best. The analytical result obtained by Evans and La Celle is also given in the same figure. The computational and analytical graphs show very similar results.

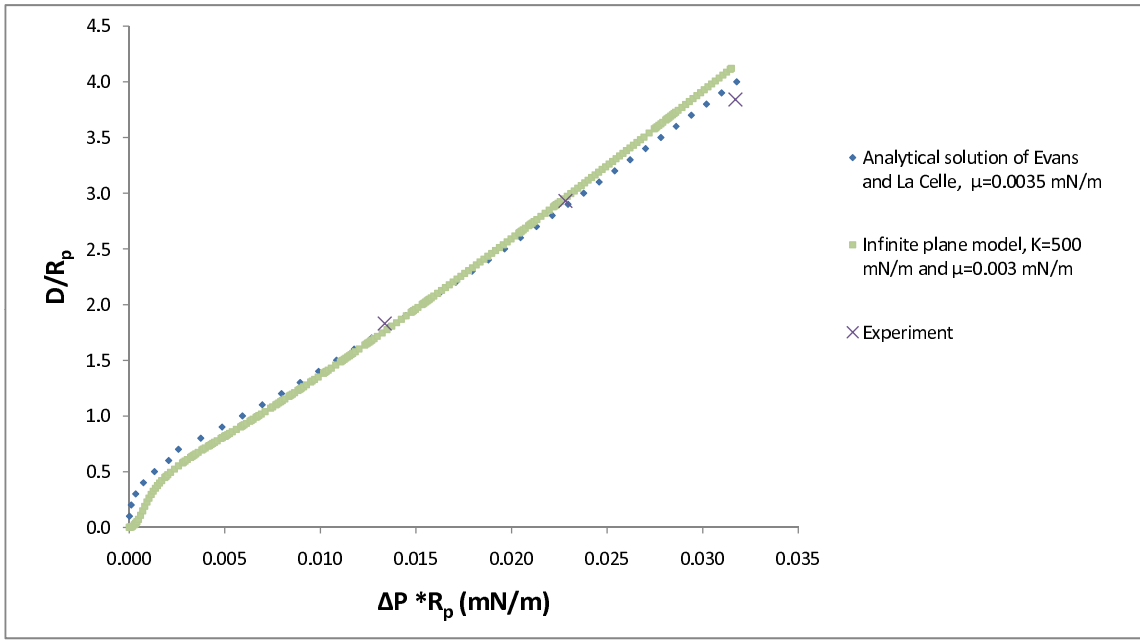


Figure 6.1. Comparison of the experimental and analytical results given by Evans and La Celle [32] and FE simulation for infinite plane membrane model with  $K = 500 \text{ mN/m}$  and  $\mu = 3 \cdot 10^{-3} \text{ mN/m}$

Results of infinite plane membrane models with different element numbers (125, 250 and 500 elements) for  $K = 500 \text{ mN/m}$  and  $\mu = 3 \cdot 10^{-3} \text{ mN/m}$  are given in figure 6.2. Since the three curves show very similar results the mesh with 250 elements is chosen for the infinite plane model.

The effects of the two elastic material constants,  $K$  and  $\mu$  are also investigated where one of the constants varied and the other one is kept constant. Figure 6.3 shows the graphs for different  $K$  values. In these simulations the value of  $\mu$  is  $3 \cdot 10^{-3} \text{ mN/m}$ . It can be easily seen that the variation in  $K$  values results in slightly different curves.

In figure 6.4 different  $\Delta P \cdot R_p$  vs.  $D/R_p$  curves for different  $\mu$  values are compared where  $K$  value is fixed to  $500 \text{ mN/m}$ . Variation in  $\mu$  value greatly affects the distance of the aspirated tongue in the pipette.

As indicated before the validity of the constitutive relation used in the present work (equations 3.30 and 3.31) has to be proved by checking whether the fractional surface area change,  $\alpha$  remained small.  $\alpha$  is plotted as a function of curvilinear distance,  $s$ ,

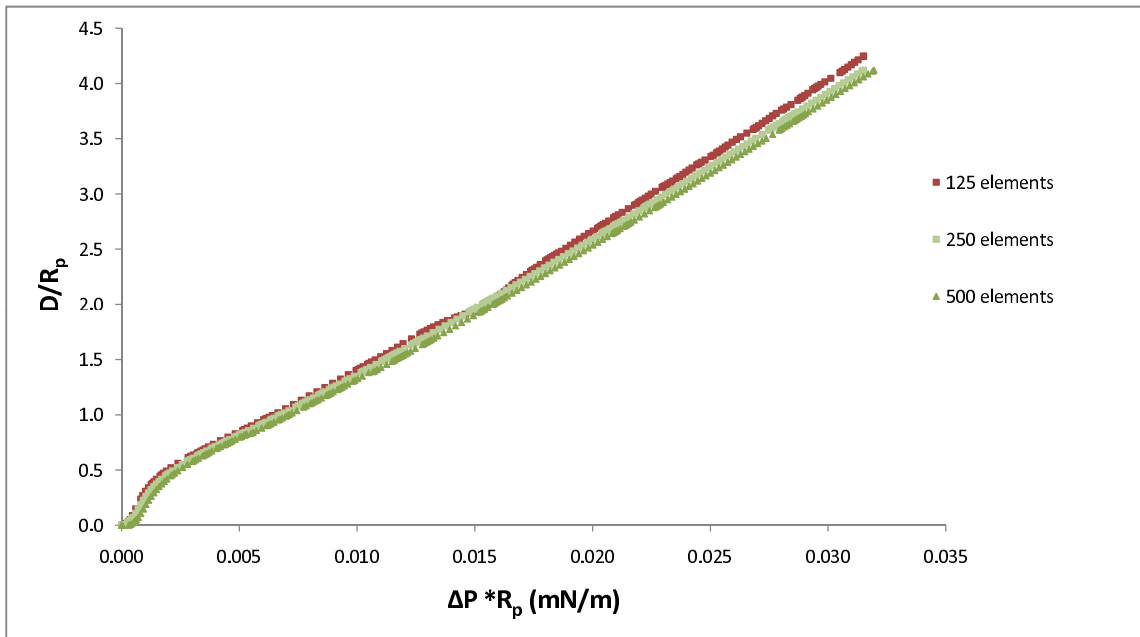


Figure 6.2. Results of infinite plane membrane models with different element numbers for  $K = 500 \text{ mN/m}$  and  $\mu = 3 \cdot 10^{-3} \text{ mN/m}$

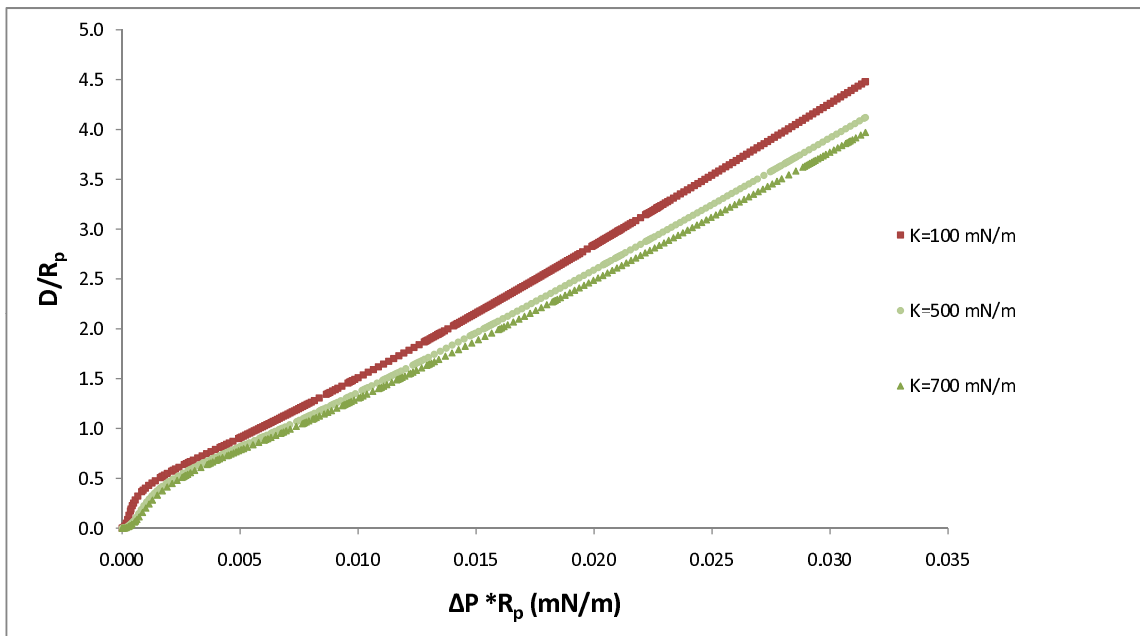


Figure 6.3. Comparison of FE simulation results for infinite plane membrane model with fixed value of  $\mu = 3 \cdot 10^{-3} \text{ mN/m}$  and different  $K$  values: a)  $K = 100 \text{ mN/m}$ , b)  $K = 500 \text{ mN/m}$ , c)  $K = 700 \text{ mN/m}$

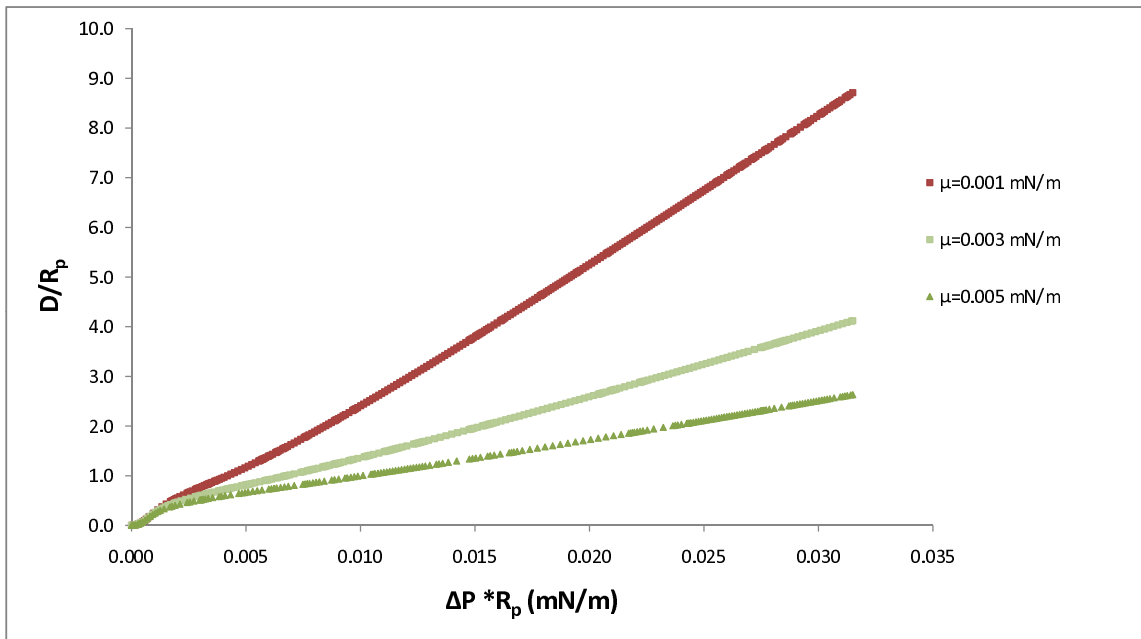


Figure 6.4. Comparison of FE simulations results for infinite plane membrane model with fixed value of  $K = 500 \text{ mN/m}$  and different  $\mu$  values: a)  $\mu = 1 \cdot 10^{-3} \text{ mN/m}$ , b)  $\mu = 3 \cdot 10^{-3} \text{ mN/m}$ , c)  $\mu = 5 \cdot 10^{-3} \text{ mN/m}$

along the meridian from the pole of the aspirated tongue to the outer membrane surface in figure 6.5 at the pressure value of 0.07 kPa for the values of  $K$  and  $\mu$  as  $500 \text{ mN/m}$  and  $3 \cdot 10^{-3} \text{ mN/m}$ , respectively. The graph indicates that the fractional surface area values are very small meaning that the membrane remained almost incompressible.

Same graphs are computed for different  $K$  values by keeping the  $\mu$  value constant at  $3 \cdot 10^{-3} \text{ mN/m}$  to see the effect of in-plane bulk modulus on surface area increase. When the graphs 6.5, 6.6, 6.7 and 6.8 are investigated it becomes obvious that the fractional surface area values in micropipette aspiration of flaccid RBC are very small even for the value of  $K = 1 \text{ mN/m}$ .

The stretches in the first and second principal directions, namely  $\lambda_1$  and  $\lambda_2$  are also computed. Figures 6.9 and 6.10 give the principal stretches as a function of curvilinear distance,  $s$ , at the suction pressure of 0.07 kPa for  $K = 500 \text{ mN/m}$  and  $\mu = 3 \cdot 10^{-3} \text{ mN/m}$ . Evans and Skalak have obtained a similar graph for the first principal stretch in their analytical analysis [29].

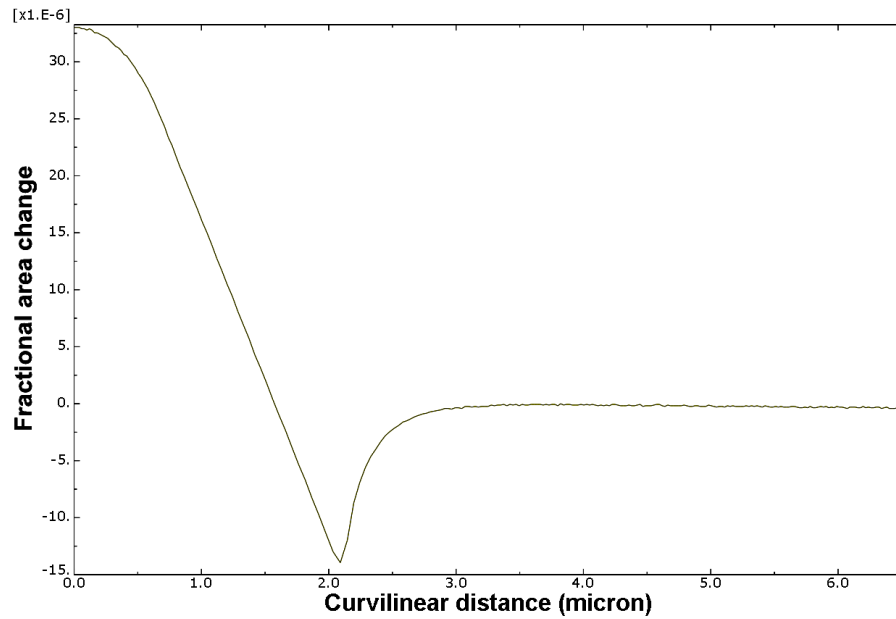


Figure 6.5. Fractional area change,  $\alpha$  in the infinite plane membrane model as a function of curvilinear distance,  $s$ , along the meridian from the pole of the aspirated tongue to the outer membrane surface for  $K = 500 \text{ mN/m}$  and  $\mu = 3 \cdot 10^{-3} \text{ mN/m}$  at  $\Delta P = 0.07 \text{ kPa}$

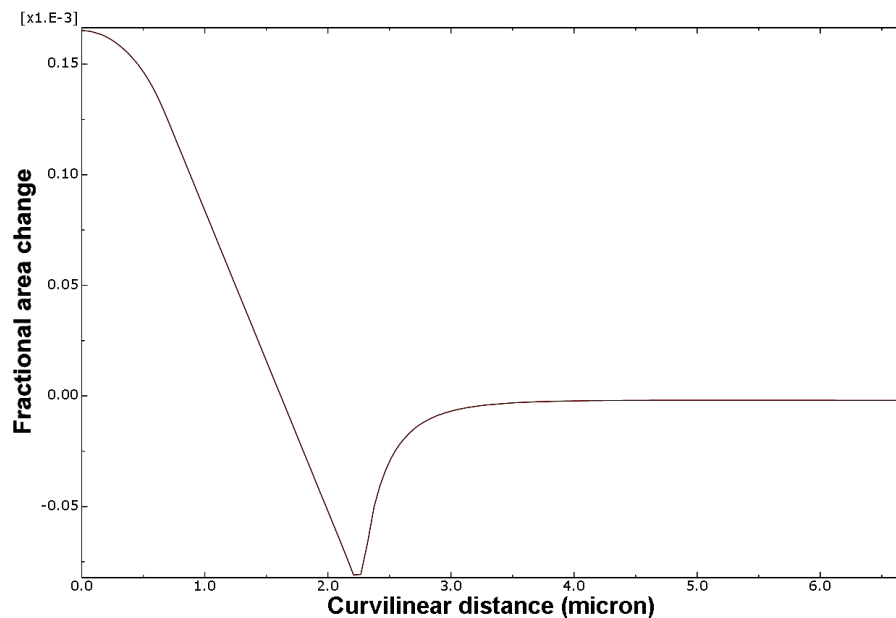


Figure 6.6. Fractional area change,  $\alpha$  as a function of curvilinear distance,  $s$ , along the meridian from the pole of the aspirated tongue to the outer membrane surface in the infinite plane membrane model for  $K = 100 \text{ mN/m}$  and  $\mu = 3 \cdot 10^{-3} \text{ mN/m}$  at  $\Delta P = 0.07 \text{ kPa}$

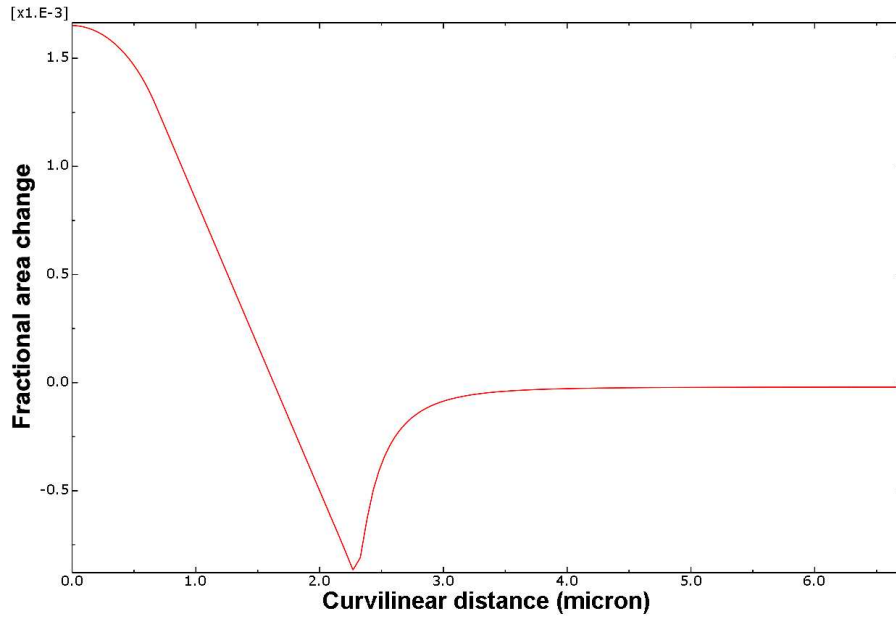


Figure 6.7. Fractional area change,  $\alpha$  as a function of curvilinear distance,  $s$ , along the meridian from the pole of the aspirated tongue to the outer membrane surface in the infinite plane membrane model for  $K = 10 \text{ mN/m}$  and  $\mu = 3 \cdot 10^{-3} \text{ mN/m}$  at  $\Delta P = 0.07 \text{ kPa}$

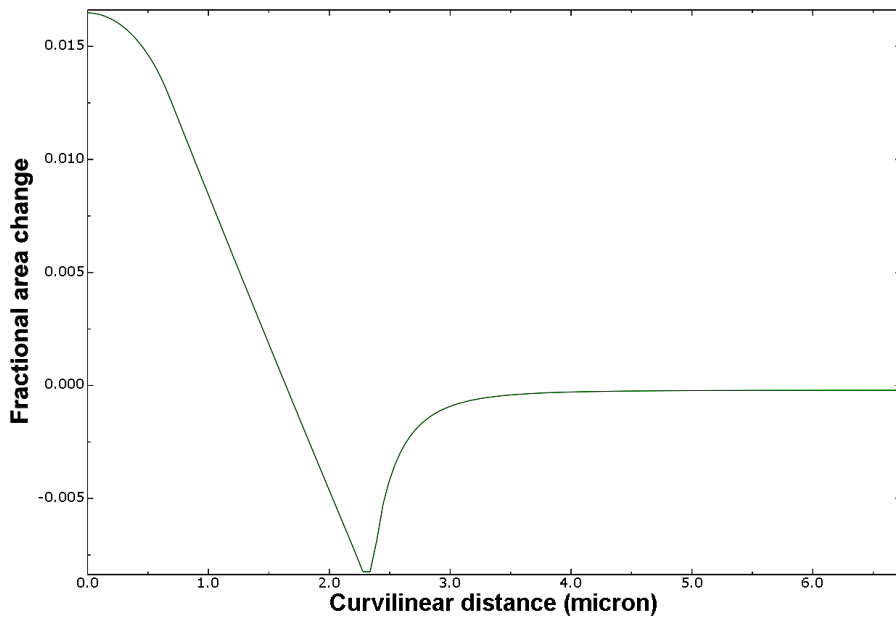


Figure 6.8. Fractional area change,  $\alpha$  as a function of curvilinear distance,  $s$ , along the meridian from the pole of the aspirated tongue to the outer membrane surface in the infinite plane membrane model for  $K = 1 \text{ mN/m}$  and  $\mu = 3 \cdot 10^{-3} \text{ mN/m}$  at  $\Delta P = 0.07 \text{ kPa}$

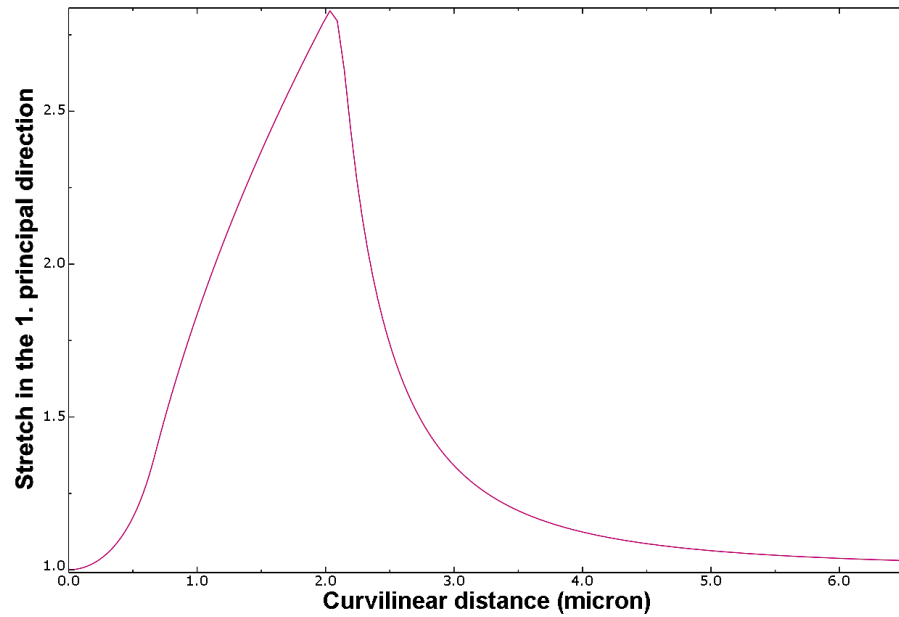


Figure 6.9. First principal stretch,  $\lambda_1$  as a function of curvilinear distance,  $s$ , along the meridian from the pole of the aspirated tongue to the outer membrane surface in the infinite plane membrane model for  $K = 500 \text{ mN/m}$  and  $\mu = 3 \cdot 10^{-3} \text{ mN/m}$  at

$$\Delta P = 0.07 \text{ kPa}$$

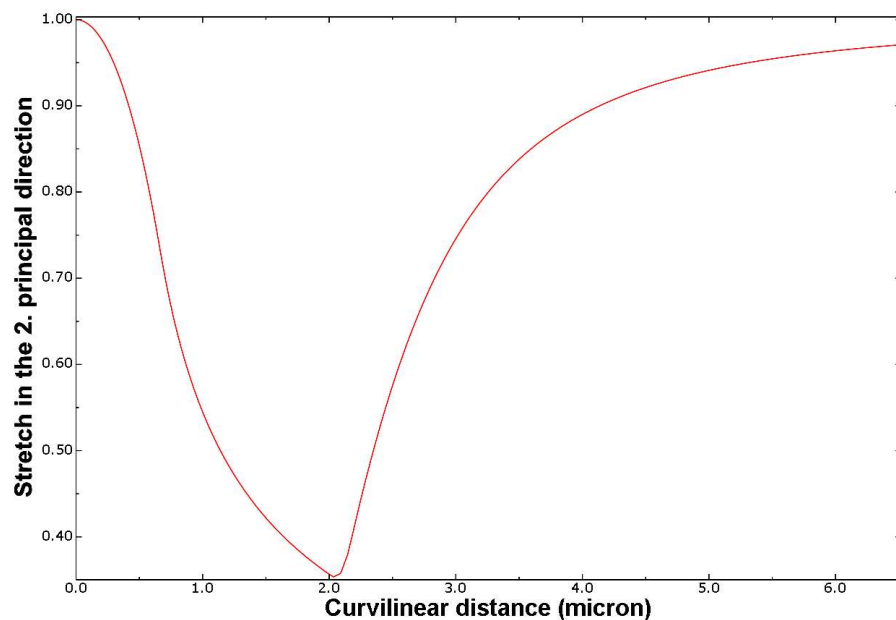


Figure 6.10. Second principal stretch,  $\lambda_2$  as a function of curvilinear distance,  $s$ , along the meridian from the pole of the aspirated tongue to the outer membrane surface in the infinite plane membrane model for  $K = 500 \text{ mN/m}$  and  $\mu = 3 \cdot 10^{-3} \text{ mN/m}$  at

$$\Delta P = 0.07 \text{ kPa}$$

The stress resultants in the first and second principal directions,  $\Sigma_1$  and  $\Sigma_2$ , respectively, may be another interesting subject. The graphs of these at the suction pressure of 0.07 kPa for  $K = 500 \text{ mN/m}$  and  $\mu = 3 \cdot 10^{-3} \text{ mN/m}$  are plotted in figures 6.11 and 6.12.

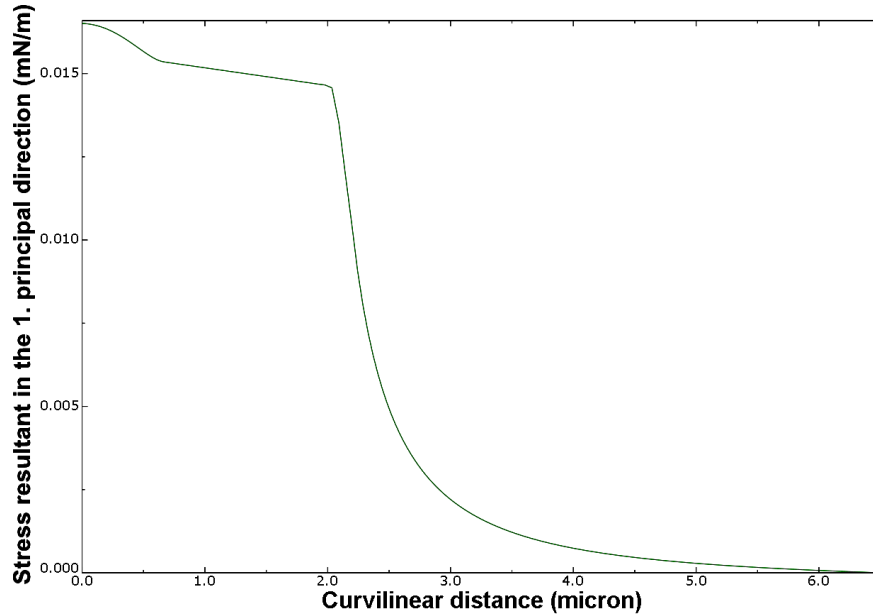


Figure 6.11. First principal stress resultant,  $\Sigma_1$  in the meridional direction as a function of curvilinear distance,  $s$ , along the meridian from the pole of the aspirated tongue to the outer membrane surface in the infinite plane membrane model for

$$K = 500 \text{ mN/m} \text{ and } \mu = 3 \cdot 10^{-3} \text{ mN/m} \text{ at } \Delta P = 0.07 \text{ kPa}$$

## 6.2. Disk Model

The  $\Delta P \cdot R_p$  vs.  $D/R_p$  graph obtained from the FE simulations of disk model for the elastic material constants  $K = 500 \text{ mN/m}$  and  $\mu = 3 \cdot 10^{-3} \text{ mN/m}$  is given in figure 6.13 with the experimental results obtained by Evans and La Celle [32]. The computational result fits the experimental data well. The analytical result obtained by Evans and La Celle is also given in the same figure.

Results of disk model with different element numbers (250, 500 and 750 elements) for  $K = 500 \text{ mN/m}$  and  $\mu = 3 \cdot 10^{-3} \text{ mN/m}$  are given in figure 6.14. The mesh with 500 elements is chosen for the simulation of the disk model.

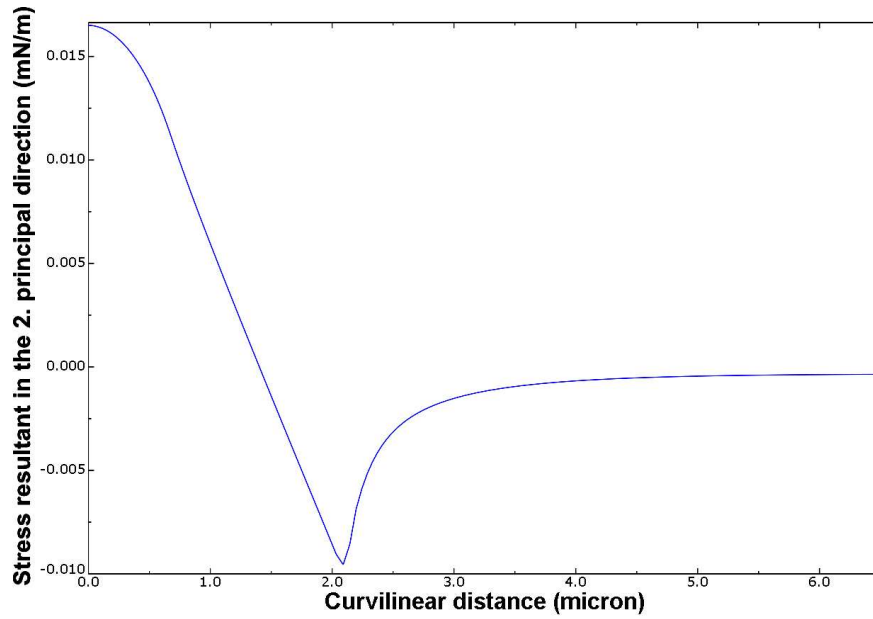


Figure 6.12. Second principal stress resultant,  $\Sigma_2$  in the circumferential direction as a function of curvilinear distance,  $s$ , along the meridian from the pole of the aspirated tongue to the outer membrane surface in the infinite plane membrane model for  $K = 500 \text{ mN/m}$  and  $\mu = 3 \cdot 10^{-3} \text{ mN/m}$  at  $\Delta P = 0.07 \text{ kPa}$

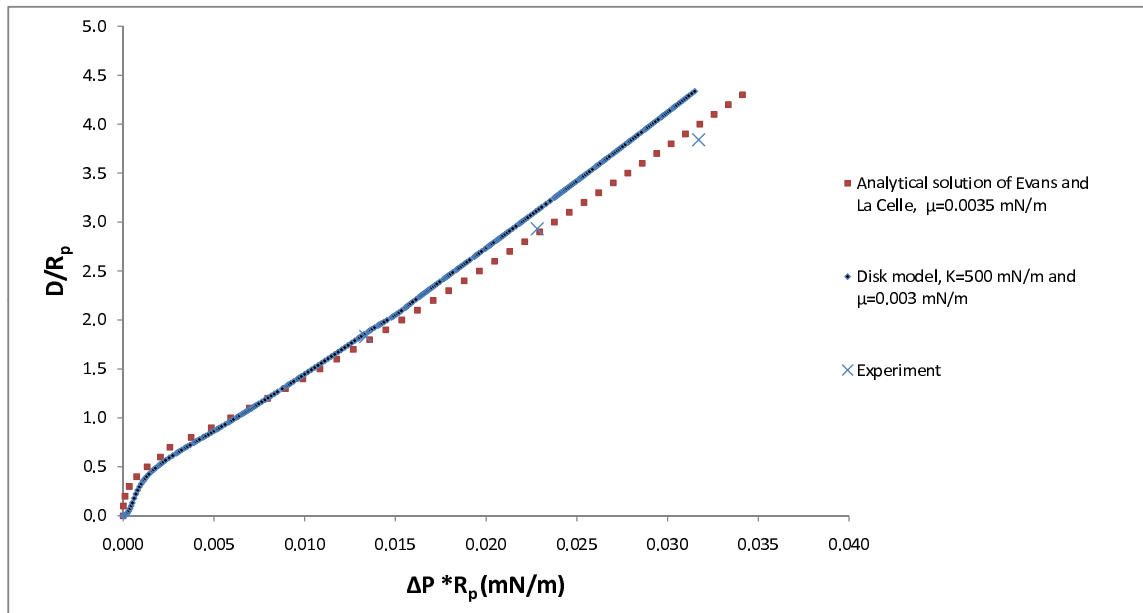


Figure 6.13. Comparison of the experimental and analytical results given by Evans and La Celle [32] and FE simulation with  $K = 500 \text{ mN/m}$  and  $\mu = 3 \cdot 10^{-3} \text{ mN/m}$  for disk model

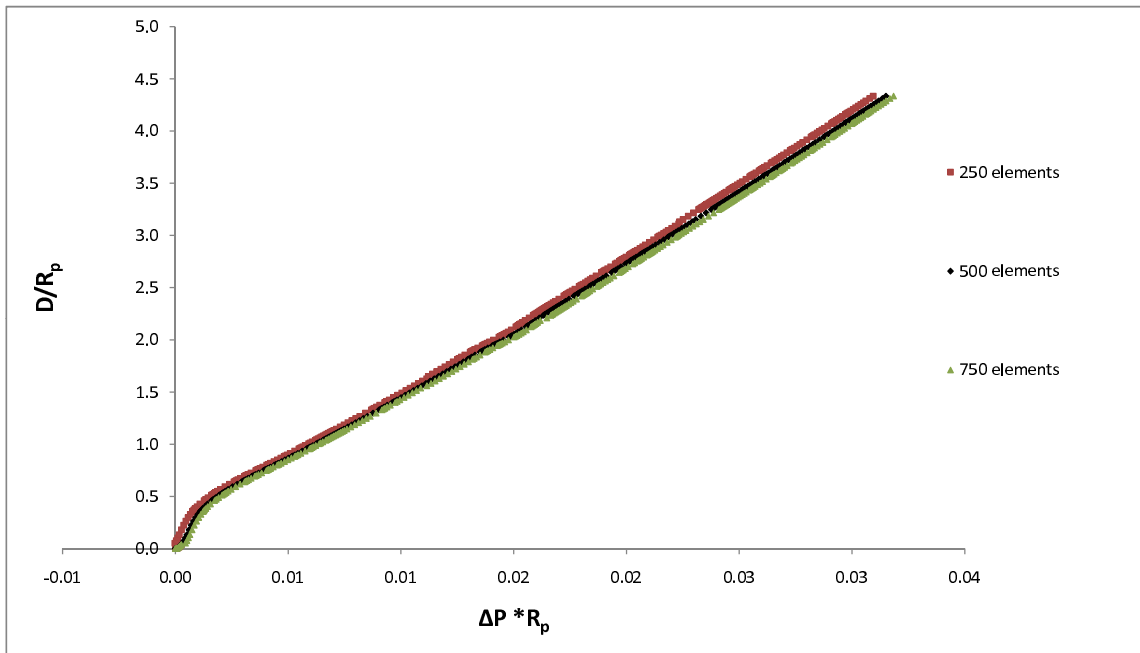


Figure 6.14. Results of disk models with different element numbers for  $K = 500 \text{ mN/m}$  and  $\mu = 3 \cdot 10^{-3} \text{ mN/m}$

Figure 6.15 shows the graphs for different  $K$  values. In these simulations the value of  $\mu$  is  $3 \cdot 10^{-3} \text{ mN/m}$ . In figure 6.16 different  $\Delta P \cdot R_p$  vs.  $D/R_p$  curves for different  $\mu$  values are compared where  $K$  value is fixed to  $500 \text{ mN/m}$ . Similar to the infinite plane model, the observation is that the variation in  $\mu$  affects the distance of the aspirated portion whereas the effect the variation in  $K$  is slight.

Figure 6.17 compares the simulation results of the infinite plane membrane and disk models for different  $\mu$  values where  $K$  value is fixed to  $500 \text{ mN/m}$ . The results of the two models for the same  $\mu$  value are almost same.

Figures 6.18 and 6.19 give the principal stretches as a function of curvilinear distance,  $s$ , at the suction pressure of  $0.07 \text{ kPa}$  for  $K = 500 \text{ mN/m}$  and  $\mu = 3 \cdot 10^{-3} \text{ mN/m}$  for the disk model. Also, fractional area change  $\alpha$ , and stress resultants in the first and second principal directions,  $\Sigma_1$  and  $\Sigma_2$ , respectively, are computed at the suction pressure of  $0.07 \text{ kPa}$  for  $K = 500 \text{ mN/m}$  and  $\mu = 3 \cdot 10^{-3} \text{ mN/m}$  (figures 6.20, 6.21 and 6.22).

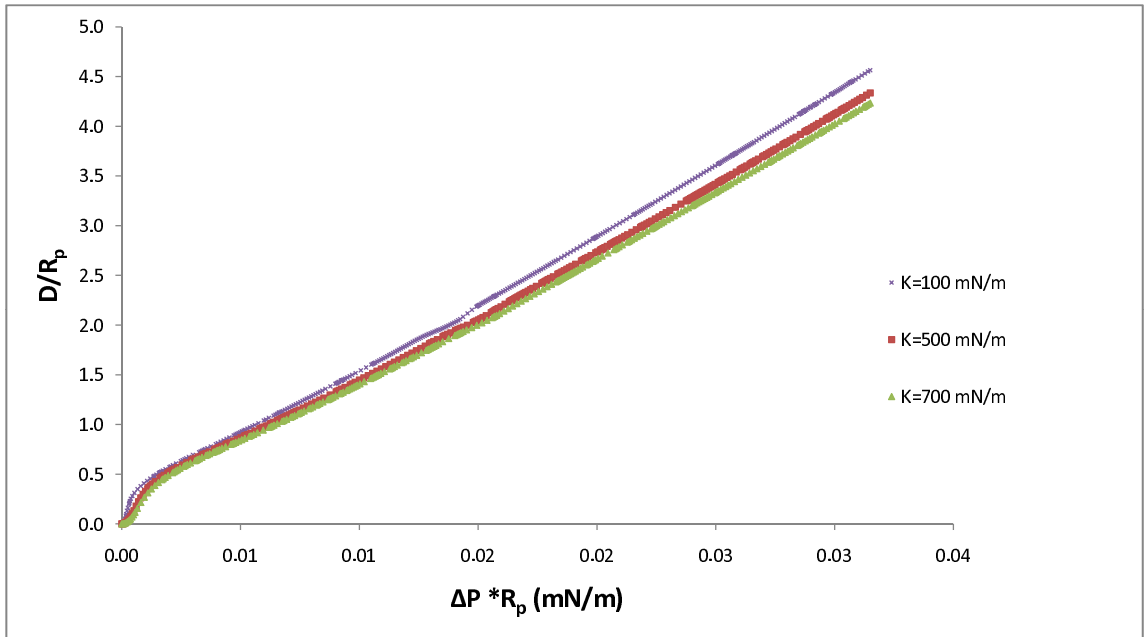


Figure 6.15. Comparison of FE simulation results of disk model with fixed value of  $\mu = 3 \cdot 10^{-3} \text{ mN/m}$  and different  $K$  values: a)  $K = 100 \text{ mN/m}$ , b)  $K = 500 \text{ mN/m}$ , c)  $K = 700 \text{ mN/m}$

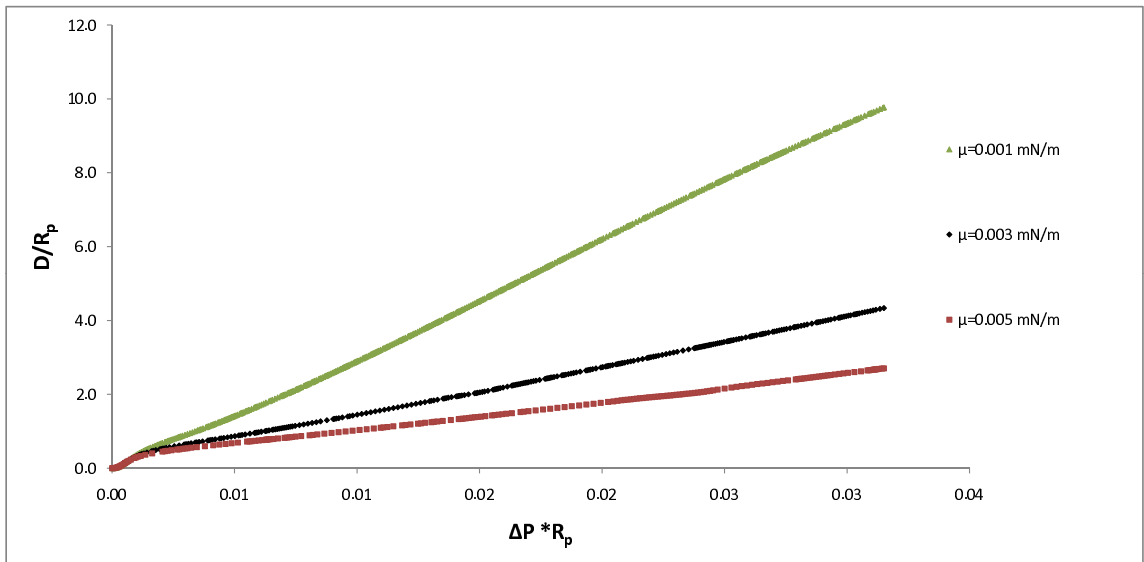


Figure 6.16. Comparison of FE simulations results of disk model with fixed value of  $K = 500 \text{ mN/m}$  and different  $\mu$  values: a)  $\mu = 1 \cdot 10^{-3} \text{ mN/m}$ , b)  $\mu = 3 \cdot 10^{-3} \text{ mN/m}$ , c)  $\mu = 5 \cdot 10^{-3} \text{ mN/m}$

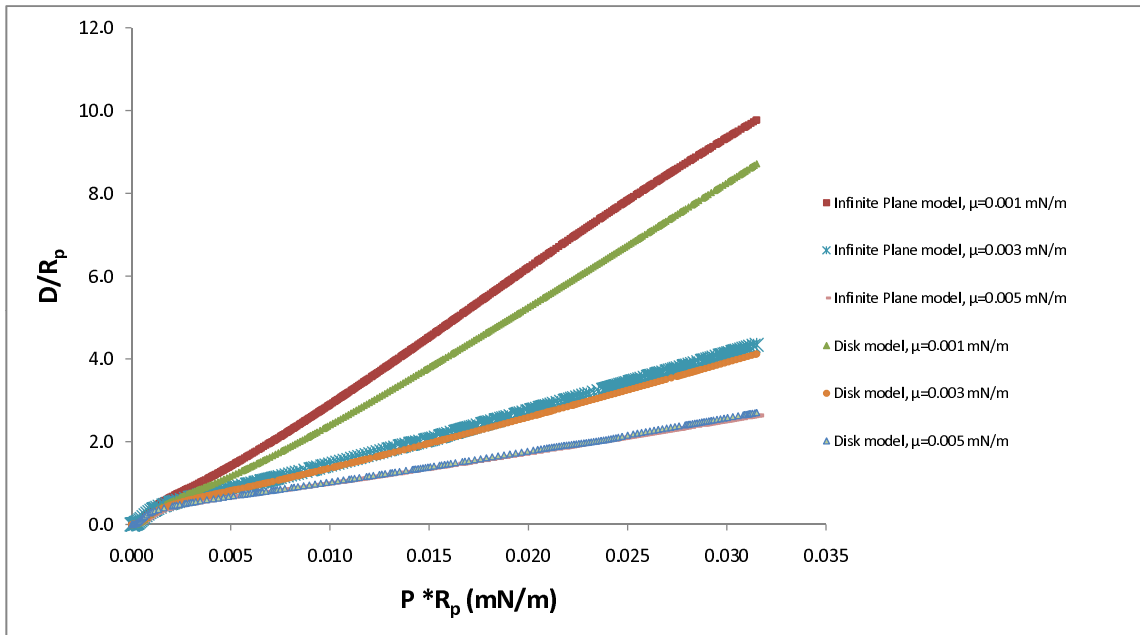


Figure 6.17. Comparison of FE simulations results of infinite plane membrane and disk models with fixed value of  $K = 500$  mN/m and different  $\mu$  values: a)  $\mu = 1 \cdot 10^{-3}$  mN/m, b)  $\mu = 3 \cdot 10^{-3}$  mN/m, c)  $\mu = 5 \cdot 10^{-3}$  mN/m

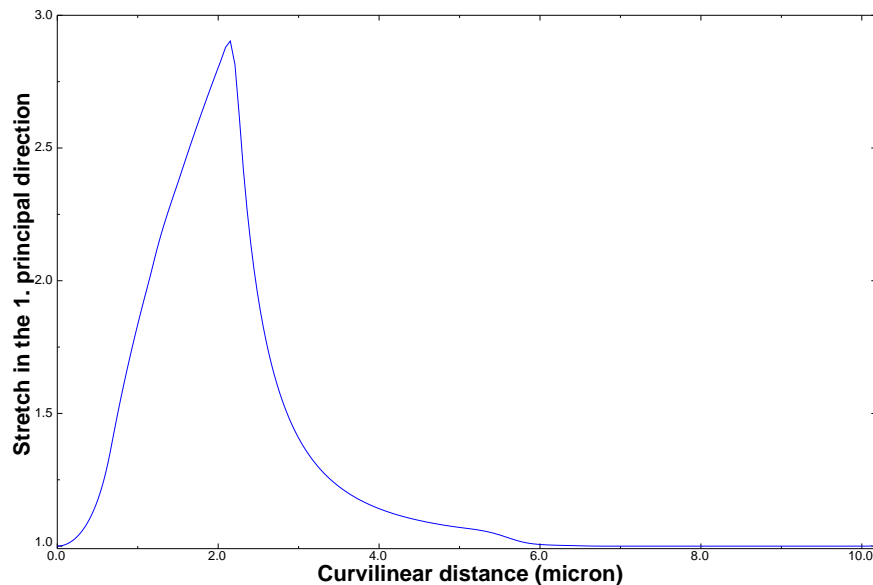


Figure 6.18. First principal stretch,  $\lambda_1$  as a function of curvilinear distance,  $s$ , along the meridian from the pole of the aspirated tongue to the outer membrane surface in the disk model for  $K = 500$  mN/m and  $\mu = 3 \cdot 10^{-3}$  mN/m at  $\Delta P = 0.07$  kPa

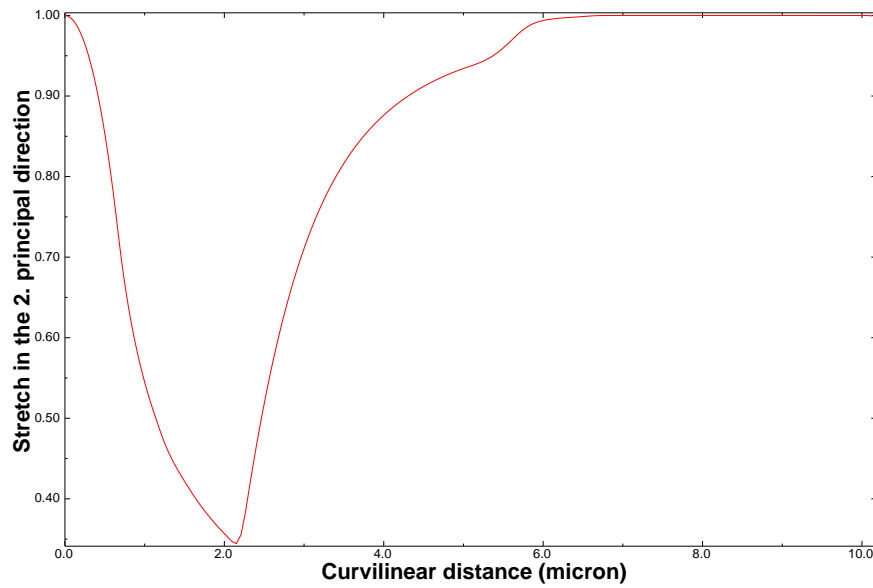


Figure 6.19. Second principal stretch,  $\lambda_2$  as a function of curvilinear distance,  $s$ , along the meridian from the pole of the aspirated tongue to the outer membrane surface in the disk model for  $K = 500 \text{ mN/m}$  and  $\mu = 3 \cdot 10^{-3} \text{ mN/m}$  at  $\Delta P = 0.07 \text{ kPa}$

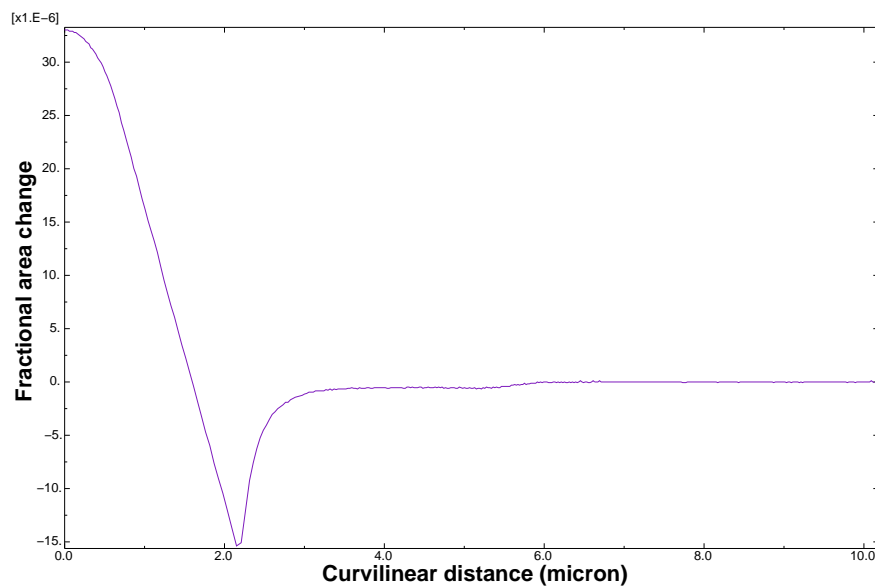


Figure 6.20. Fractional area change,  $\alpha$  in the disk model as a function of curvilinear distance,  $s$ , along the meridian from the pole of the aspirated tongue to the outer membrane surface for  $K = 500 \text{ mN/m}$  and  $\mu = 3 \cdot 10^{-3} \text{ mN/m}$  at  $\Delta P = 0.07 \text{ kPa}$

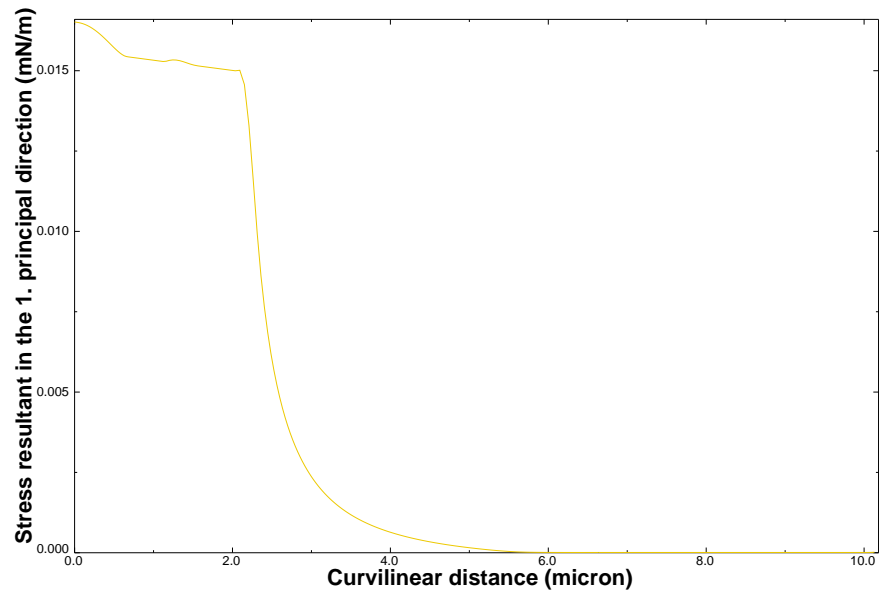


Figure 6.21. First principal stress resultant,  $\Sigma_1$  in the meridional direction as a function of curvilinear distance,  $s$ , along the meridian from the pole of the aspirated tongue to the outer membrane surface in the disk model for  $K = 500 \text{ mN/m}$  and

$$\mu = 3 \cdot 10^{-3} \text{ mN/m at } \Delta P = 0.07 \text{ kPa}$$

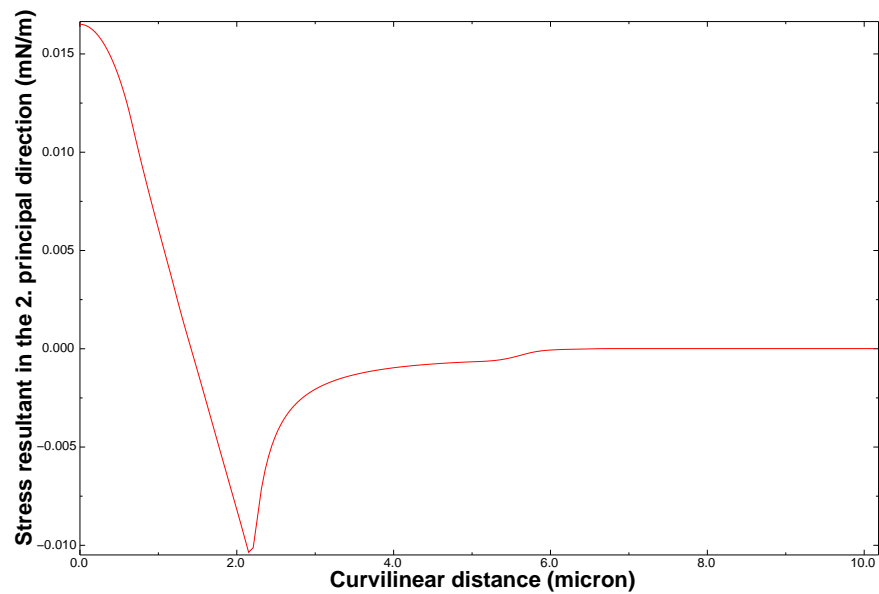


Figure 6.22. Second principal stress resultant,  $\Sigma_2$  in the circumferential direction as a function of curvilinear distance,  $s$ , along the meridian from the pole of the aspirated tongue to the outer membrane surface in the disk model for  $K = 500 \text{ mN/m}$  and

$$\mu = 3 \cdot 10^{-3} \text{ mN/m at } \Delta P = 0.07 \text{ kPa}$$

### 6.3. Modified Biconcave Model

Results of the simulations with the modified biconcave model without cytosol  $\Delta P \cdot R_p$  vs.  $D/R_p$  are very similar to the ones of the other two computational models. Variation in the value of  $\mu$  caused different  $\Delta P \cdot R_p$  vs.  $D/R_p$  curves (figure 6.23) whereas variation in the value of  $K$  resulted in similar curves (figure 6.24).

Figure 6.25 shows that the  $\Delta P \cdot R_p$  vs.  $D/R_p$  curve which fits the experimental data is the one with the  $\mu$  value close to 0.004 mN/m. The convergence check for modified biconcave model is done with three different meshes (250, 500 and 750 elements) for  $K = 500 \text{ mN/m}$  and  $\mu = 3 \cdot 10^{-3} \text{ mN/m}$  are given in 6.26. The mesh with 500 elements is used for the modified biconcave model.

Comparing the results of the modified biconcave model without cytosol and the one of the infinite plane membrane model indicates that the initial curved outside portion of the cell membrane causes some differences in the results (figure 6.27), especially for lower  $\mu$  values.

If the cytosol inside the RBC is also modeled the  $\Delta P \cdot R_p$  vs.  $D/R_p$  curves do not change (figure 6.28). However, this volume preserving fluid affects the deformed shape of the RBC membrane portion outside the pipette (figure 6.29).

Figures 6.30, 6.31, 6.33 and 6.34 give the principal stretches and stress resultants as a function of curvilinear distance,  $s$ , at the suction pressure of 0.07 kPa for  $K = 500 \text{ mN/m}$  and  $\mu = 3 \cdot 10^{-3} \text{ mN/m}$  for the modified biconcave model without cytosol. The fractional area change,  $\alpha$ , is given in figure 6.32. Same plots for the modified biconcave model with cytosol are given in figures 6.35 through 6.39.

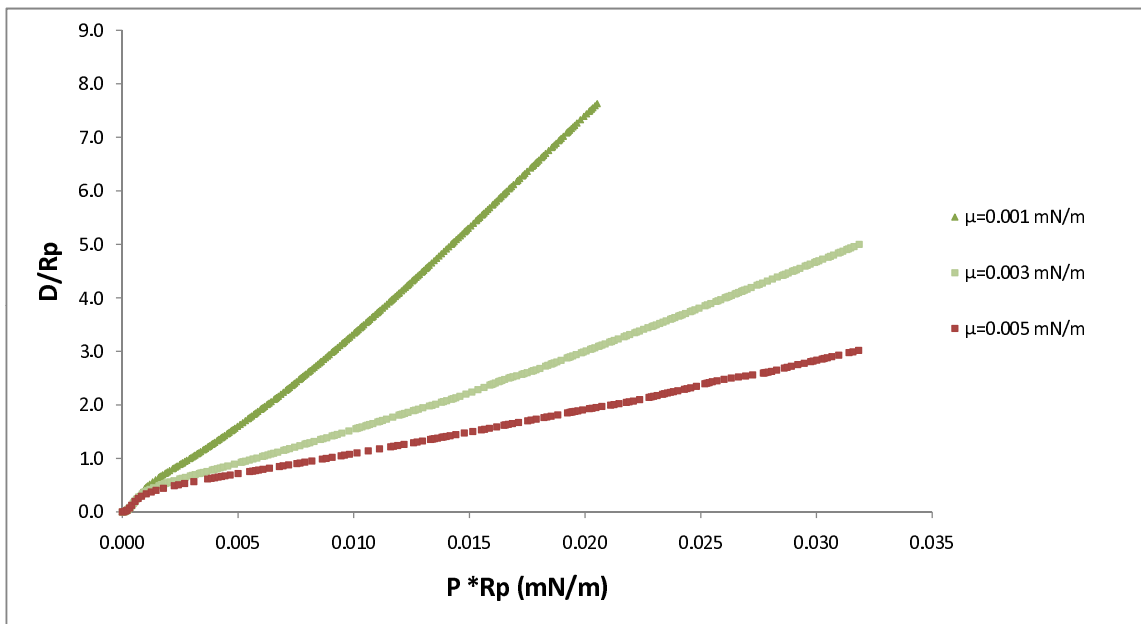


Figure 6.23. Comparison of FE simulations results of modified biconcave shape model without cytosol for fixed value of  $K = 500 \text{ mN/m}$  and different  $\mu$  values: a)  $\mu = 1 \cdot 10^{-3} \text{ mN/m}$ , b)  $\mu = 3 \cdot 10^{-3} \text{ mN/m}$ , c)  $\mu = 5 \cdot 10^{-3} \text{ mN/m}$

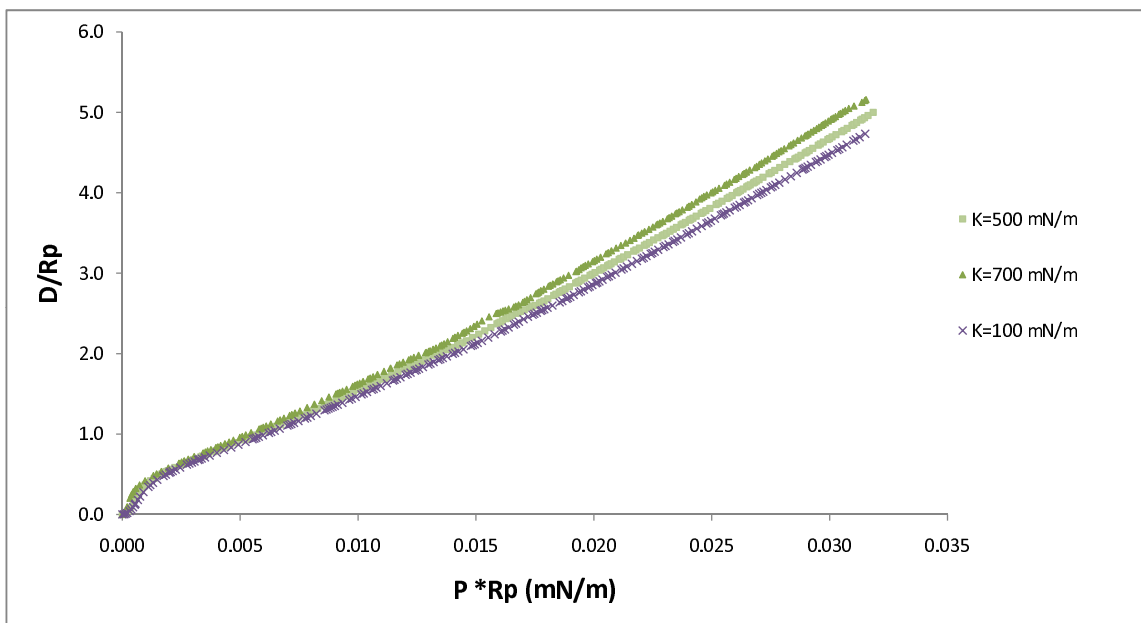


Figure 6.24. Comparison of FE simulations results of modified biconcave shape model without cytosol for fixed value of  $\mu = 3 \cdot 10^{-3} \text{ mN/m}$  and different  $K$  values: a)  $K = 100 \text{ mN/m}$ , b)  $K = 500 \text{ mN/m}$ , c)  $K = 700 \text{ mN/m}$

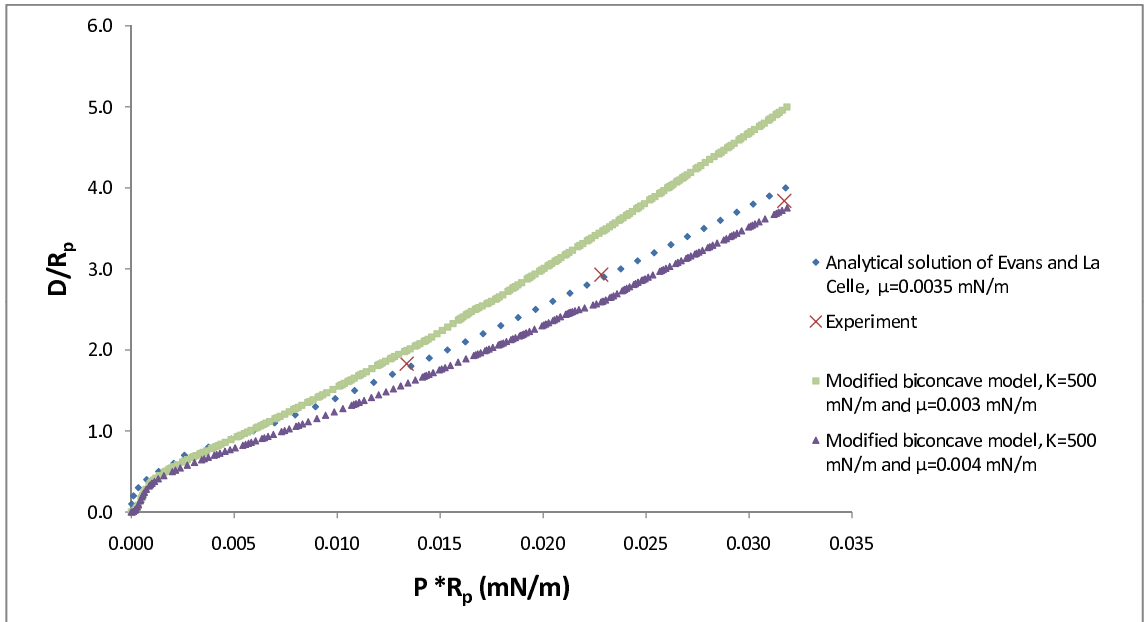


Figure 6.25. Comparison of the experimental and analytical results given by Evans and La Celle [32] and FE simulation with  $K = 500$  mN/m and  $\mu = 3 \cdot 10^{-3}$  mN/m and  $\mu = 4 \cdot 10^{-3}$  mN/m for modified biconcave model without cytosol

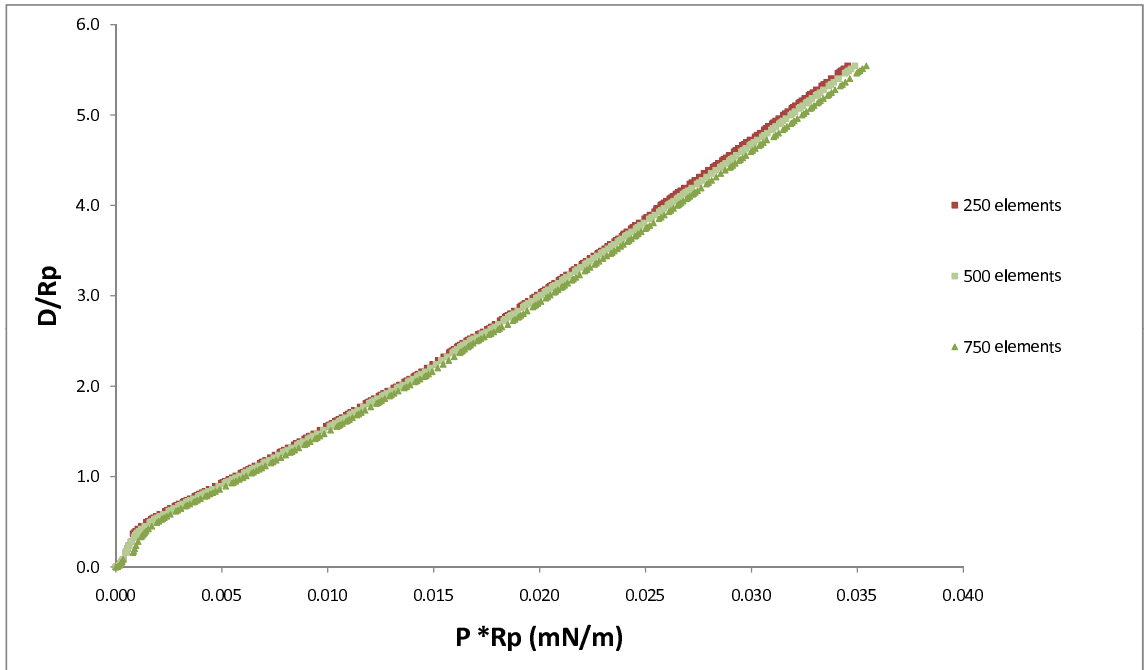


Figure 6.26. Results of modified biconcave models with different element numbers for  $K = 500$  mN/m and  $\mu = 3 \cdot 10^{-3}$  mN/m

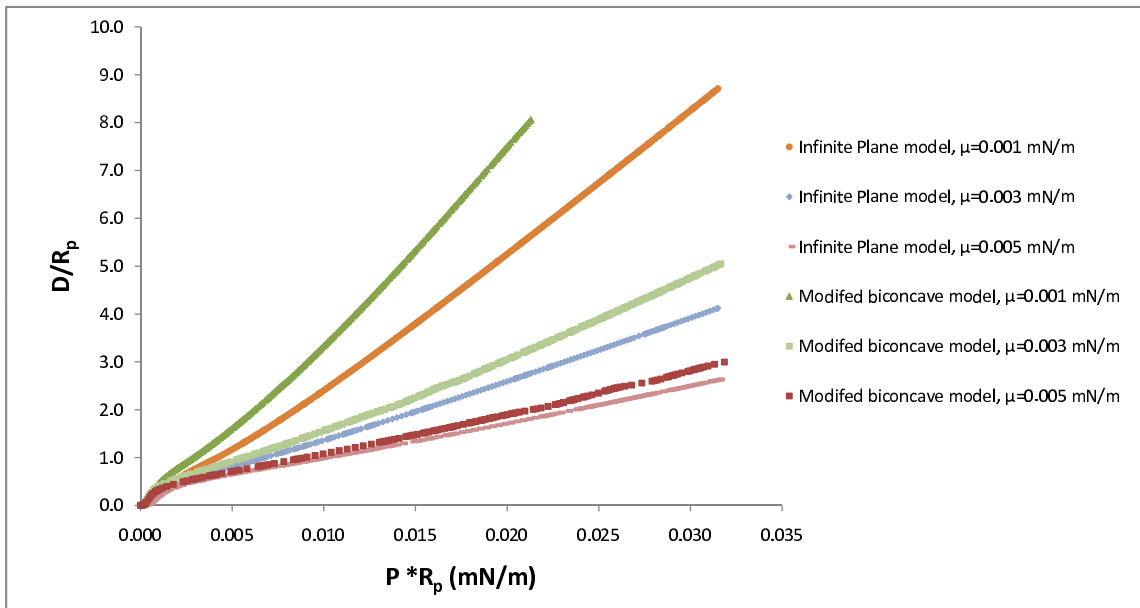


Figure 6.27. Comparison of FE simulations results of infinite plane membrane and modified biconcave model without cytosol with fixed value of  $K = 500 \text{ mN/m}$  and different  $\mu$  values: a)  $\mu = 1 \cdot 10^{-3} \text{ mN/m}$ , b)  $\mu = 3 \cdot 10^{-3} \text{ mN/m}$ , c)  $\mu = 5 \cdot 10^{-3} \text{ mN/m}$

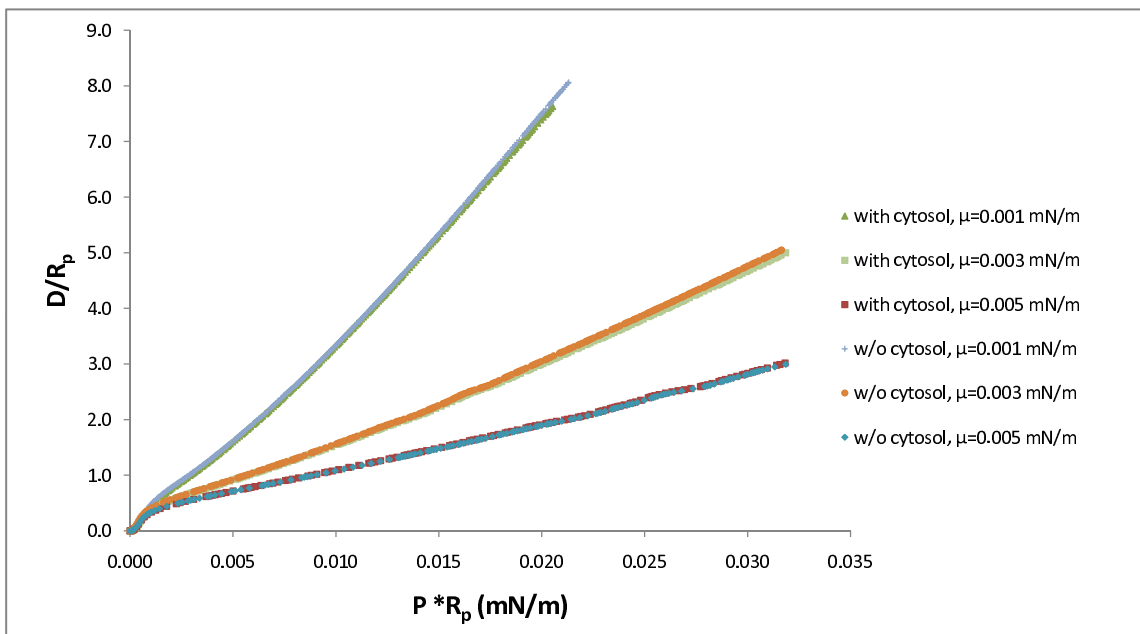


Figure 6.28. Comparison of FE simulations results of modified biconcave shape model with and without cytosol with fixed value of  $K = 500 \text{ mN/m}$  and different  $\mu$  values: a)  $\mu = 1 \cdot 10^{-3} \text{ mN/m}$ , b)  $\mu = 3 \cdot 10^{-3} \text{ mN/m}$ , c)  $\mu = 5 \cdot 10^{-3} \text{ mN/m}$

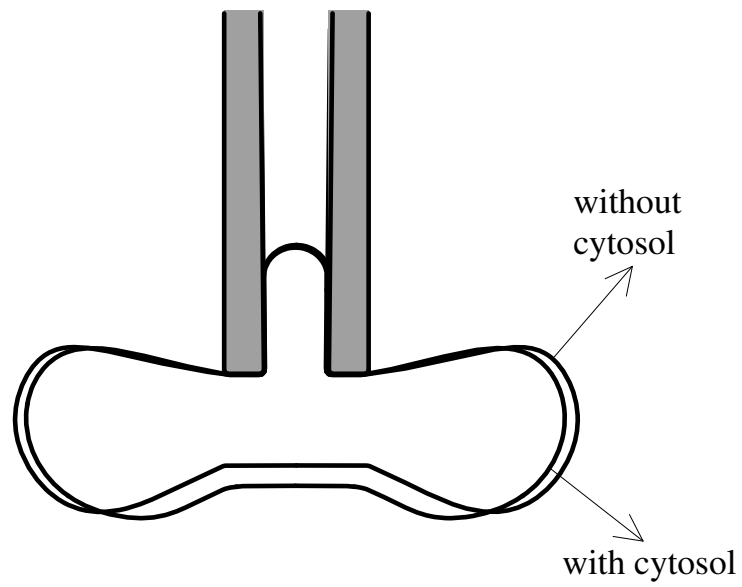


Figure 6.29. Deformed shapes of modified biconcave model with and without cytosol

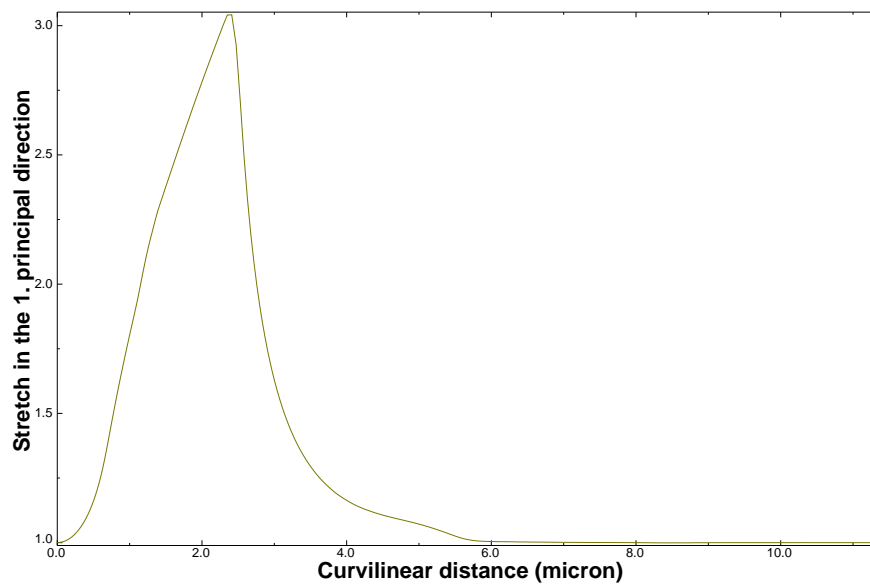


Figure 6.30. First principal stretch,  $\lambda_1$  as a function of curvilinear distance,  $s$ , along the meridian from the pole of the aspirated tongue to the outer membrane surface in

the modified biconcave model without cytosol for  $K = 500 \text{ mN/m}$  and

$$\mu = 3 \cdot 10^{-3} \text{ mN/m at } \Delta P = 0.07 \text{ kPa}$$

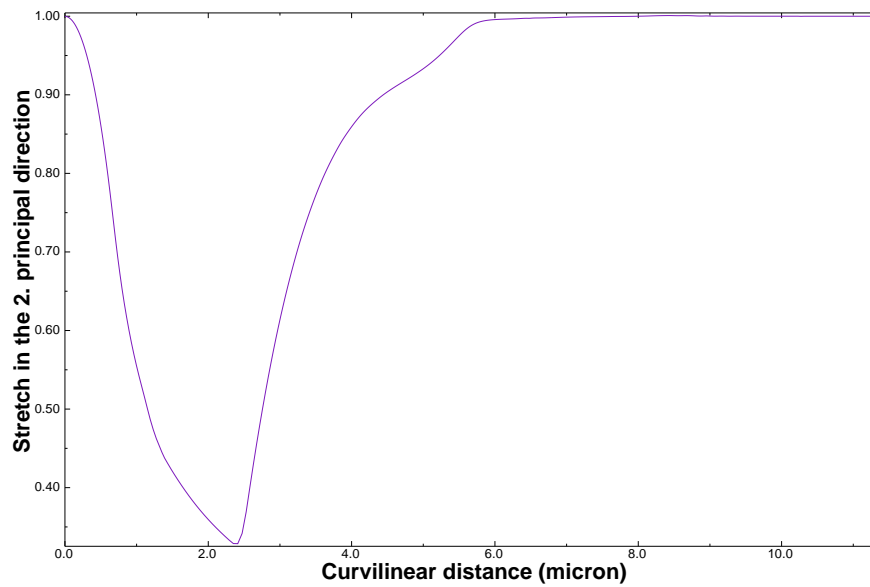


Figure 6.31. Second principal stretch,  $\lambda_2$  as a function of curvilinear distance,  $s$ , along the meridian from the pole of the aspirated tongue to the outer membrane surface in the modified biconcave model without cytosol for  $K = 500 \text{ mN/m}$  and

$$\mu = 3 \cdot 10^{-3} \text{ mN/m at } \Delta P = 0.07 \text{ kPa}$$

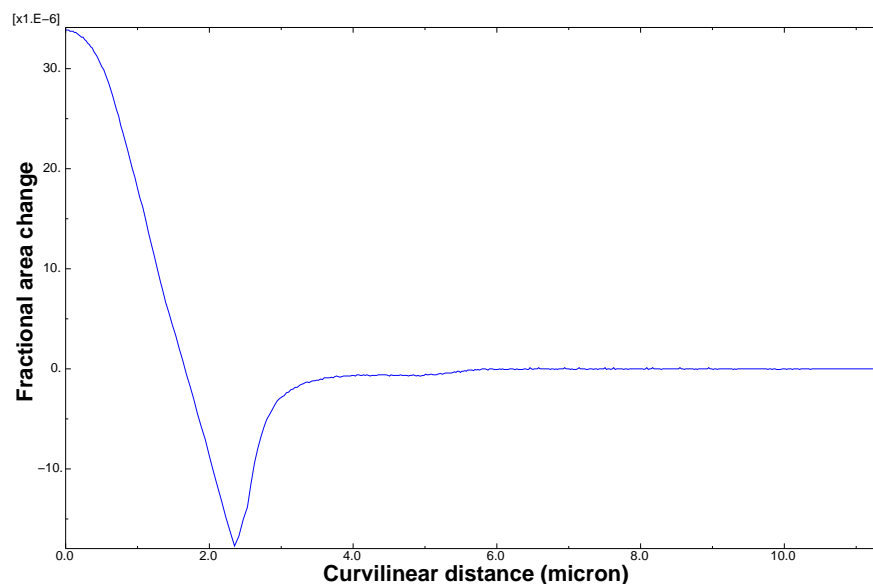


Figure 6.32. Fractional area change,  $\alpha$  in the modified biconcave model without cytosol model as a function of curvilinear distance,  $s$ , along the meridian from the pole of the aspirated tongue to the outer membrane surface for  $K = 500 \text{ mN/m}$  and

$$\mu = 3 \cdot 10^{-3} \text{ mN/m}$$

$$\text{at } \Delta P = 0.07 \text{ kPa}$$

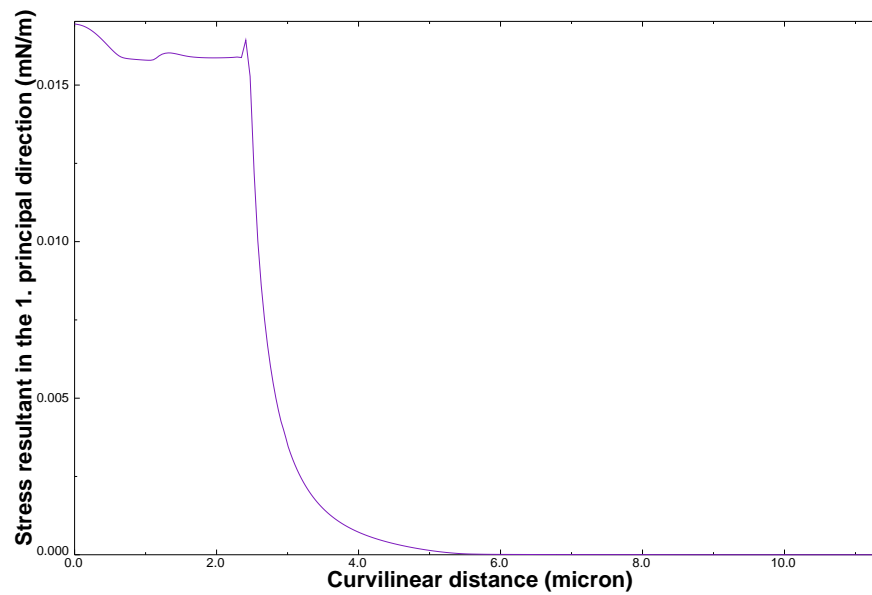


Figure 6.33. First principal stress resultant,  $\Sigma_1$  in the meridional direction as a function of curvilinear distance,  $s$ , along the meridian from the pole of the aspirated tongue to the outer membrane surface in the modified biconcave model without cytosol for  $K = 500 \text{ mN/m}$  and  $\mu = 3 \cdot 10^{-3} \text{ mN/m}$  at  $\Delta P = 0.07 \text{ kPa}$

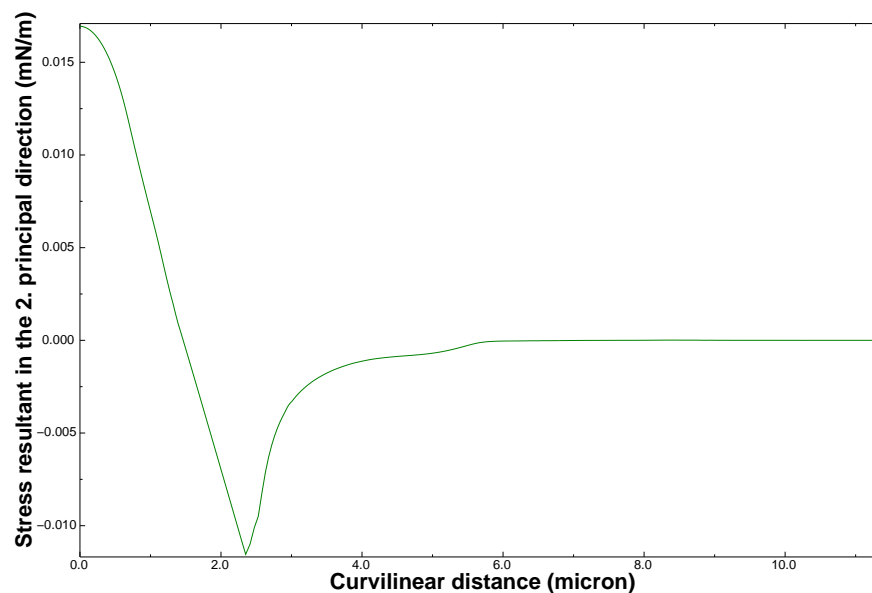


Figure 6.34. Second principal stress resultant,  $\Sigma_2$  in the circumferential direction as a function of curvilinear distance,  $s$ , along the meridian from the pole of the aspirated tongue to the outer membrane surface in the modified biconcave model without cytosol for  $K = 500 \text{ mN/m}$  and  $\mu = 3 \cdot 10^{-3} \text{ mN/m}$  at  $\Delta P = 0.07 \text{ kPa}$

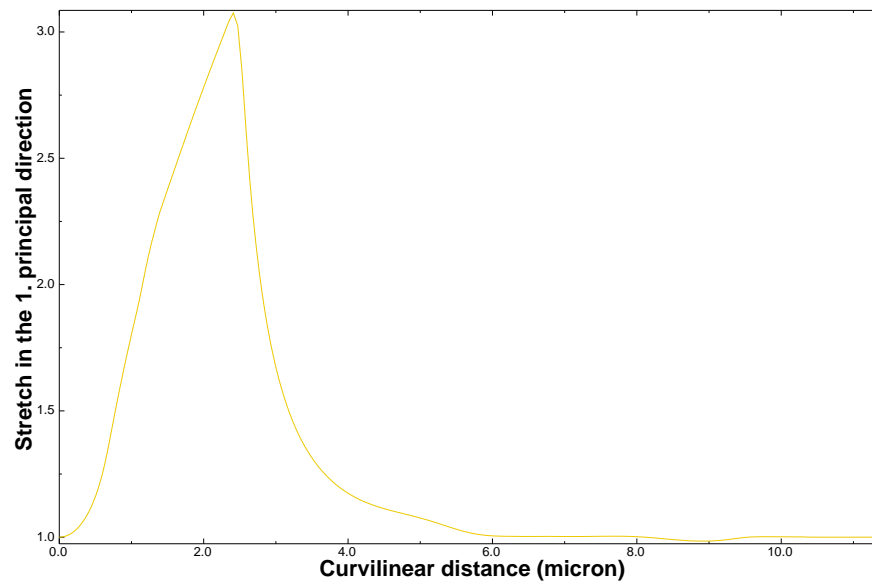


Figure 6.35. First principal stretch,  $\lambda_1$  as a function of curvilinear distance,  $s$ , along the meridian from the pole of the aspirated tongue to the outer membrane surface in the modified biconcave model with cytosol for  $K = 500 \text{ mN/m}$  and

$$\mu = 3 \cdot 10^{-3} \text{ mN/m at } \Delta P = 0.07 \text{ kPa}$$

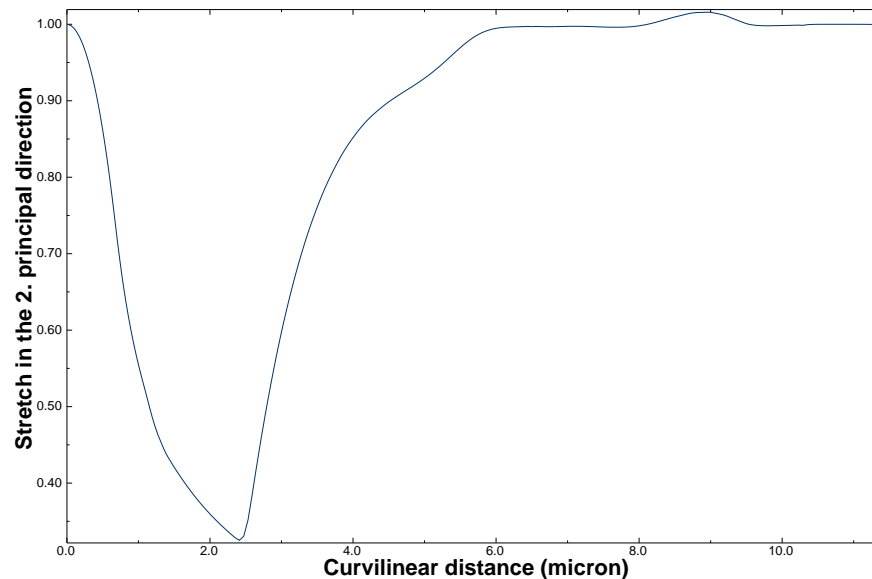


Figure 6.36. Second principal stretch,  $\lambda_2$  as a function of curvilinear distance,  $s$ , along the meridian from the pole of the aspirated tongue to the outer membrane surface in the modified biconcave model with cytosol for  $K = 500 \text{ mN/m}$  and

$$\mu = 3 \cdot 10^{-3} \text{ mN/m at } \Delta P = 0.07 \text{ kPa}$$

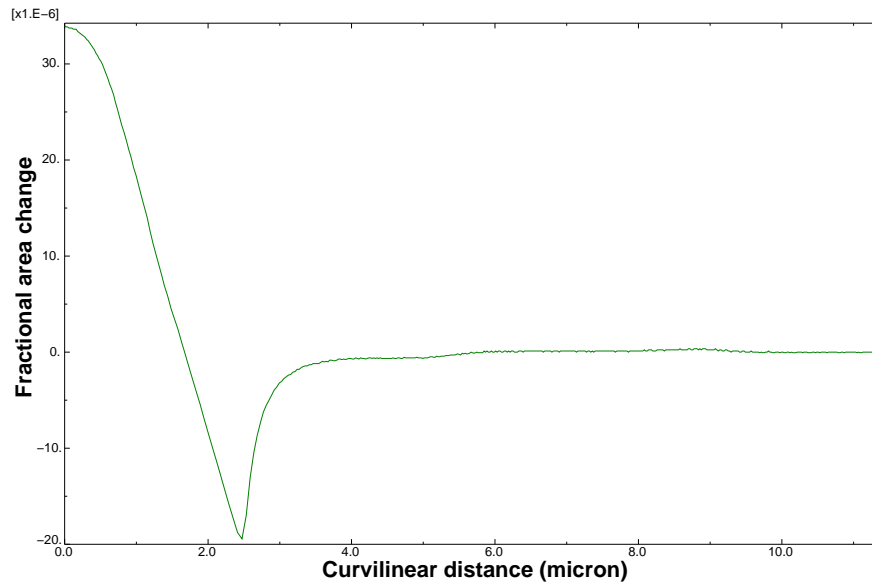


Figure 6.37. Fractional area change,  $\alpha$  in the modified biconcave model with cytosol model as a function of curvilinear distance,  $s$ , along the meridian from the pole of the aspirated tongue to the outer membrane surface for  $K = 500 \text{ mN/m}$  and

$$\mu = 3 \cdot 10^{-3} \text{ mN/m}$$

$$\text{at } \Delta P = 0.07 \text{ kPa}$$

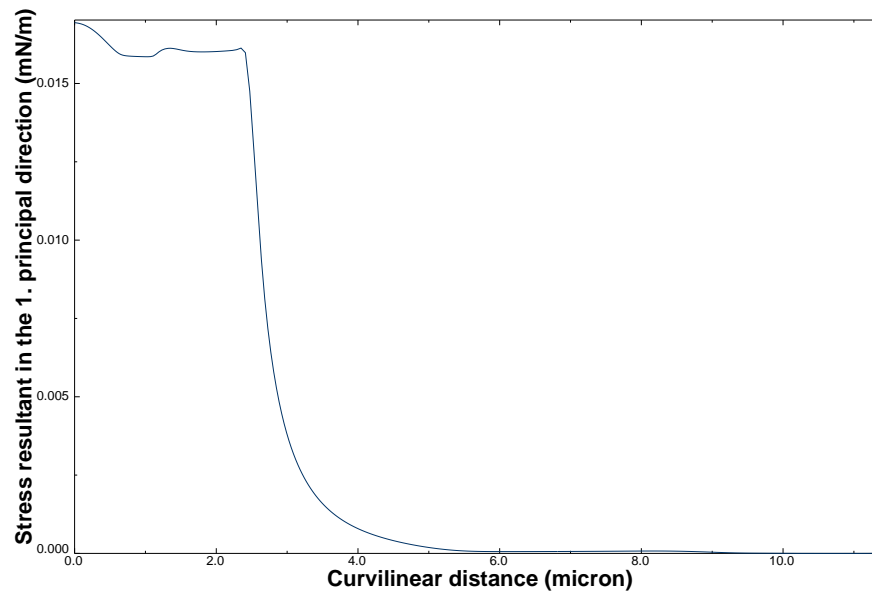


Figure 6.38. First principal stress resultant,  $\Sigma_1$  in the meridional direction as a function of curvilinear distance,  $s$ , along the meridian from the pole of the aspirated tongue to the outer membrane surface in the modified biconcave model with cytosol for  $K = 500 \text{ mN/m}$  and  $\mu = 3 \cdot 10^{-3} \text{ mN/m}$  at  $\Delta P = 0.07 \text{ kPa}$

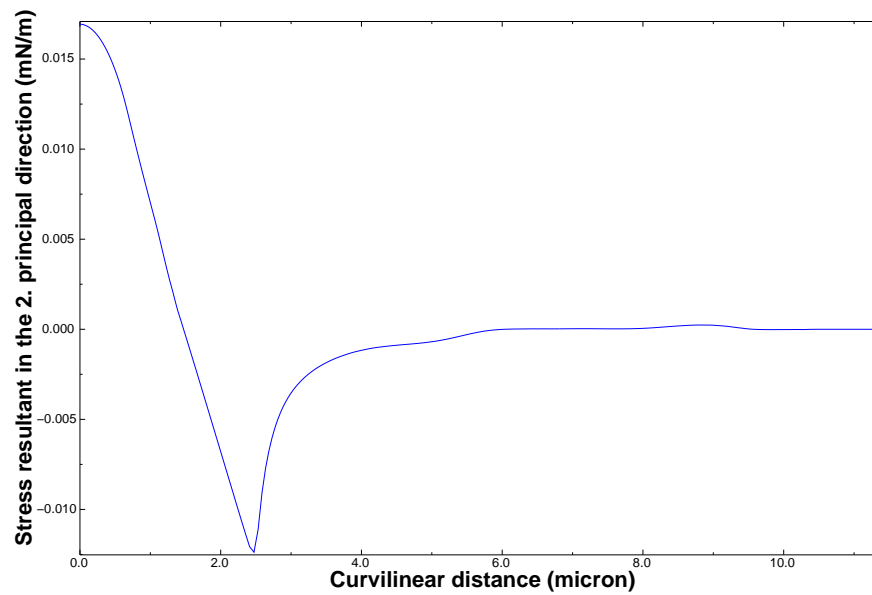


Figure 6.39. Second principal stress resultant,  $\Sigma_2$  in the circumferential direction as a function of curvilinear distance,  $s$ , along the meridian from the pole of the aspirated tongue to the outer membrane surface in the modified biconcave model with cytosol for  $K = 500 \text{ mN/m}$  and  $\mu = 3 \cdot 10^{-3} \text{ mN/m}$  at  $\Delta P = 0.07 \text{ kPa}$

## 7. CONCLUSION

Simulations with different in-plane bulk modulus values (100, 500 and 700 mN/m) and fixed in-plane shear modulus value ( $3 \mu\text{N/m}$ ) result in similar  $\Delta P \cdot R_p$  vs.  $D/R_p$  curves for all three geometrical models. Therefore, 500 mN/m is chosen as the in-plane bulk modulus value in the computations where the appropriate value of  $\mu$  for RBC membrane is investigated. Additionally, size of the RBC membrane surface area by micropipette aspiration deformation remains almost constant for this  $K$  value in all computational models where much lower values like 1 mN/m results in significant area changes. Thus, the chosen in-plane bulk modulus value caused the surface area size to remain almost constant after the deformation and hence, a nearly incompressible, 2D material is obtained.

On the other hand, in-plane shear modulus,  $\mu$ , greatly affects the  $\Delta P \cdot R_p$  vs.  $D/R_p$  results for all computational models. By investigating the in-plane shear modulus value that produce the  $\Delta P \cdot R_p$  vs.  $D/R_p$  curves, which fit the experimental data best, the appropriate value for this material constant is estimated. Even though the appropriate  $\mu$  value differs slightly for different computed geometries, the value is in the range of 3-4  $\mu\text{N/m}$ . This corroborates the in-plane shear modulus values in literature.

Curved shape of the RBC affects the results. This can be realized comparing  $\Delta P \cdot R_p$  vs.  $D/R_p$  results of the infinite plane model and those of the disk model. Furthermore, results of the modified biconcave model manifest this fact more pronounced. Thus, the initial curved outside portion affects the deformation of flaccid RBC in micropipette aspiration which has to be taken into account.

Cytosol is never modeled in the previous analytical analyses. Hence, its contribution to whole cell deformation in the micropipette aspiration experiment has not been investigated in these works. In the present study cytosol is modeled as a volume preserving hydraulic fluid and it is shown that cytosol has no effect on the deformed RBC portion inside the pipette. It just changes the shape of the outer RBC portion.

Hence, modeling the cytosol does not influence the membrane in-plane shear modulus value estimation.

Furthermore, stretch and stress resultant values in the principal directions are also computed at the maximum applied suction pressure in the experiment. Investigation of the first and second principal stretches,  $\lambda_1$  and  $\lambda_2$ , which are in the meridional and circumferential directions, respectively, as a function of curvilinear distance,  $s$  along the meridian from the pole of the aspirated tongue to the outer membrane surface shows that the material element located at the top of the leading edge inside the pipette is not stretched.  $\lambda_1$  increases as the pipette tip is approached. Maximum value of  $\lambda_1$  is obtained at the pipette tip and far away from the tip on the outer membrane portion almost no stretch in the first principal direction is observable. On the other hand,  $\lambda_2$  decreases approaching the pipette tip and the minimum value is reached at the pipette tip. Again, far away from the tip on the outer membrane portion almost no stretch in the second principal direction is observable. First principal stress resultant,  $\Sigma_1$  decreases along the meridian from the pole of the aspirated tongue to the outer membrane. A plateau is observable for the membrane portion which is in contact with the pipette. Second principal stress resultant,  $\Sigma_2$  first decreases as the pipette tip is approached from the aspirated tongue pole, has a minimum value at the tip and reaches the zero-value on the outer membrane portion far away from the tip.

This work is the first FE analysis for large deformation study of human red blood cell membrane in micropipette aspiration experiment where a 2D material model is implemented to the FE package. In future, other whole cell experiments conducted with RBC like osmotic swelling and optical tweezer stretching can be modeled this way in order to investigate the deformation and material characteristics of RBC and its membrane at continuum level. Results of such continuum models can be used as the start point for microstructure analyses of RBC membrane.

## REFERENCES

1. Lim, C. T., *Single Cell Mechanics Study of the Human Disease Malaria*, Journal of Biomechanical Science and Engineering, Vol. 1, No. 1, pp. 82-92, 2006.
2. Boal, D., *Mechanics of the Cell*, Cambridge University Press, Cambridge, 2002.
3. <http://www.academic.marist.edu/~jzmz/methods/rcmorph.html>
4. Hochmuth, R. M., *Measuring the Mechanical Properties of Individual Human Blood Cells*, Journal of Biomechanical Engineering, Vol. 115, pp. 515-519, 1993.
5. Dao, M., C.T. Lim and S. Suresh, *Mechanics of the Human Red Blood Cell Deformed by Optical Tweezers*, Journal of the Mechanics and Physics of Solids, Vol. 51, pp. 2259-2280, 2003.
6. Lim, C. T., M. Dao, S. Suresh, C. H. Sow and K. T. Chew *Large Deformation of Living Cells Using Optical Traps*, Acta Materialia, Vol. 52, pp. 1837-1845, 2004.
7. Lim, C. T., E. H. Zhou and S. T. Quek *Mechanical Models for Living Cells - A Review*, Journal of Biomechanics, Vol. 39, pp. 195-216, 2006.
8. Hochmuth, R. M., *Properties of Red Blood Cells*, Handbook of Bioengineering, Chapter 12, 1987.
9. Waugh, R. E. and R. M. Hochmuth, *Mechanics and Deformability of Hematocytes*, The Biomedical Engineering Handbook, Chapter 32, CRC Press, 2000.
10. Hochmuth, R. M., *Micropipette Aspiration of Living Cells*, Journal of Biomechanics, Vol. 33, pp. 15-22, 2000.
11. Lim, C. T., E. H. Zhou, A. Li, S. R. K. Vedula and H. X. FU *Experimental Techniques for Single Cell and Single Molecule Biomechanics*, Materials Science and

- Engineering, Vol. C 26, pp. 1278-1288, 2006.
12. Rand, R. P. and A. C. Burton, *Mechanical Properties of Red Cell Membrane: I. Membrane Stiffness and Intracellular Pressure*, Biophysical Journal, Vol. 4, pp. 115-135, 1964.
  13. Rand, R. P., *Mechanical Properties of Red Cell Membrane: II. Viscoelastic Breakdown of the Membrane*, Biophysical Journal, Vol. 4, pp. 303-316, 1964.
  14. Hochmuth, R. M. and N. Mohandas, *Uniaxial Loading of the Red-Cell Membrane*, Journal of Biomechanics, Vol. 5, pp. 501-509, 1972.
  15. Evans, E. and Y. C. Fung, *Improved Measurements of the Erythrocyte Geometry*, Microvascular Research, Vol. 4, pp. 335-347, 1972.
  16. Evans, E. A., *A New Material Concept for the Red Cell Membrane*, Biophysical Journal, Vol. 13, pp. 926-940, 1973.
  17. Evans, E. A., *New Membrane Concept Applied to the Analysis of Fluid Shear- and Micropipette-Deformed Red Blood Cells*, Biophysical Journal, Vol. 13, pp. 941-954, 1973.
  18. Skalak, R., A. Tozeren, R. P. Zarda and S. Chien, *Strain Energy Function of Red Blood Cell Membranes*, Biophysical Journal, Vol. 13, pp. 245-264, 1973.
  19. Evans, E. A., *Bending Resistance and Chemically Induced Moments in Membrane Bilayers*, Biophysical Journal, Vol. 14, pp. 923-931, 1974.
  20. Evans, E. A., *Bending Elastic Modulus of Red Blood Cell Membrane Derived from Buckling Instability in Micropipet Aspiration Tests*, Biophysical Journal, Vol. 43, pp. 27-30, 1983.
  21. Zarda, P. R., S. Chien and R. Skalak, *Elastic Deformations of Red Blood Cells*, Journal of Biomechanics, Vol. 10, pp. 211-221, 1977.

22. Pai B. K. and H. D. Weymann, *Equilibrium Shapes of Red Blood Cells in Osmotic Swelling*, Journal of Biomechanics, Vol. 13, pp. 105-112, 1980.
23. Mills, J. P., L. Qie, M. Dao, C.T. Lim and S. Suresh, *Nonlinear Elastic and Viscoelastic Deformation of the Human Red Blood Cell with Optical Tweezers*, Molecular and Cellular Biomechanics, Vol. 1, No. 3, pp. 169-180, 2004.
24. Chien, S., K. P. Sung, R. Skalak, S. Usami and A. Tozeren, *Theoretical and Experimental Studies on Viscoelastic Properties of Erythrocyte Membrane*, Biophysical Journal, Vol. 24, pp. 463-487, 1978.
25. Higuchi, R. and Y. Kanno *Finite Element Method Analysis of the Deformation of Human Red Blood Cells*, JSME International Journal, Series A, Vol. 49, No. 3, pp. 331-336, 2006.
26. Liu, I., *Continuum Mechanics*, Springer, New York, 2002.
27. Doghri, I., *Mechanics of Deformable Solids: Linear, Nonlinear, Analytical and Computational Aspects*, Springer, New York, 2000.
28. Holzapfel, G. A., *Nonlinear Solid Mechanics*, WILEY, 2001.
29. Evans, E. A. and R. Skalak, *Mechanics and Thermodynamics of Biomembranes*, CRC Press, Florida, 1980.
30. Evans, E. A., R. Waugh and L. Melnik, *Elastic Area Compressibility Modulus of Red Cell Membrane*, Biophysical Journal, Vol. 16, pp. 585-595, 1976.
31. Ugural, A. C., *Stresses in Plates and Shells*, McGraw-Hill, Singapore, 1999.
32. Evans, E. A. and P. L. La Celle, *Intrinsic Material Properties of the Erythrocyte Membrane Indicated by Mechanical Analysis of Deformation*, Blood, Vol. 45, pp. 29-43, 1975.

## REFERENCES NOT CITED

1. *ABAQUS Theory Manual, Version 6.7*, ABAQUS Inc., 2007.
2. Fung, Y. C. B and P.Tong, *Theory of The Sphering of Red Blood Cells*, Biophysical Journal, Vol. 8, pp. 175-18, 1968.
3. Pug-de-Morales-Marinkovich, M., K. T. Turner, J. P. Butler, J. J. Fredberg and S. Suresh, *Viscoelasticity of the Human Red Blood Cell*, American Journal of Physiology - Cell Physiology, Vol. 293, pp. C597-C605, 2007.
4. Evans, E. A. and R. M. Hochmuth, *Membrane Viscoplastic Flow*, Biophysical Journal, Vol. 16, pp. 13-26, 1976.
5. Evans, E. A. and R. M. Hochmuth, *Membrane Viscoelasticity*, Biophysical Journal, Vol. 16, pp. 1-11, 1976.